

AD-A095 254

PENNSYLVANIA STATE UNIV UNIVERSITY PARK APPLIED RESE--ETC F/8 11/6  
THE HIGH RESOLUTION IMAGING ATOM-PROBE WITH APPLICATION TO NICK--ETC(U)  
DEC 80 M MARTINKA

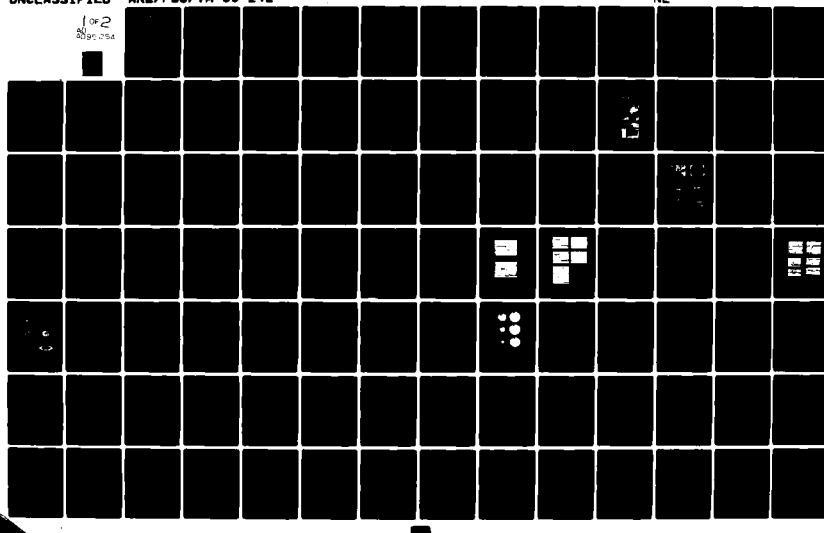
N00024-79-C-6043

UNCLASSIFIED

ARL/PSU/TM-80-242

NL

1 of 2  
2000-0000



AD A095254

LEVEL ✓

12

THE HIGH RESOLUTION IMAGING ATOM-PROBE  
WITH APPLICATION TO NICKEL PLATINGS.

Michael Martinka

Technical Memorandum  
File No. TM 80-242  
December 17, 1980  
Contract No. N00024-79-C-6043

Copy No. 12

DTIC  
ELECTRONIC  
FEB 20 1981  
S C C

The Pennsylvania State University  
Intercollege Research Programs and Facilities  
APPLIED RESEARCH LABORATORY  
Post Office Box 30  
State College, PA 16801

APPROVED FOR PUBLIC RELEASE DISTRIBUTION UNLIMITED

NAVY DEPARTMENT

NAVAL SEA SYSTEMS COMMAND

81 2 20 015

## UNCLASSIFIED

SECURITY CLASSIFICATION OF THIS PAGE (When Data Entered)

REPORT DOCUMENTATION PAGE		READ INSTRUCTIONS BEFORE COMPLETING FORM
1. REPORT NUMBER TM 80-242	2. GOVT ACCESSION NO. AD-AC95254	3. RECIPIENT'S CATALOG NUMBER
4. TITLE (and Subtitle) THE HIGH RESOLUTION IMAGING ATOM-PROBE WITH APPLICATION TO NICKEL PLATINGS	5. TYPE OF REPORT & PERIOD COVERED PhD Thesis, March 1981	
7. AUTHOR(s) Michael Martinka	6. PERFORMING ORG. REPORT NUMBER TM 80-242	
9. PERFORMING ORGANIZATION NAME AND ADDRESS The Pennsylvania State University Applied Research Laboratory P. O. Box 30, State College, PA 16801	10. PROGRAM ELEMENT, PROJECT, TASK AREA & WORK UNIT NUMBERS	
11. CONTROLLING OFFICE NAME AND ADDRESS Naval Sea Systems Command Department of the Navy Washington, DC 20362	12. REPORT DATE December 17, 1980	
14. MONITORING AGENCY NAME & ADDRESS (if different from Controlling Office)	13. NUMBER OF PAGES 179 pages & figures	
	15. SECURITY CLASS. (of this report) Unclassified, Unlimited	
	15a. DECLASSIFICATION/DOWNGRADING SCHEDULE	
16. DISTRIBUTION STATEMENT (of this Report)  Approved for public release, distribution unlimited, per NSSC (Naval Sea Systems Command), 2/6/81		
17. DISTRIBUTION STATEMENT (of the abstract entered in Block 20, if different from Report)		
18. SUPPLEMENTARY NOTES		
19. KEY WORDS (Continue on reverse side if necessary and identify by block number) thesis, high resolution, imaging, mass spectrometer, nickel		
20. ABSTRACT (Continue on reverse side if necessary and identify by block number)  This work concerns the development of a high resolution imaging atom-probe time-of-flight mass spectrometer, its performance, and its application to electro- and electroless nickel, nickel-phosphorus platings, and to hydrogen adsorbed on rhodium. An imaging atom-probe displays the distribution over a sample's surface of a constituent mass species selected from the sample's time-of-flight spectra. Imaging of the sample surface is at atomic resolution by field-ion, desorption, and gated desorption microscopy. → (over)		

## UNCLASSIFIED

SECURITY CLASSIFICATION OF THIS PAGE (When Data Entered)

## 20. ABSTRACT (continued)

cont

The mass resolution of this 13.5-cm flight-path instrument was significantly increased by minimizing dispersion in the initial energy of field evaporated ions while improving timing and gating electronics. The mass resolution,  $m/m$ , at an acceptance angle of  $5.4^\circ$  is 150 at 20% above the base line. This is equivalent to the performance of one- to two-meter straight-flight-path atom-probes, and is shown by isotopic resolution  $W^{3+}$  and  $Ni^{++}$  mass spectra. Mass determinations remain accurate at the  $31^\circ$  full acceptance angle as the low mass side of spectral peaks is sharp; however, resolution is reduced to 50 by "tailing" ions resulting from premature evaporation induced by adsorbed residual hydrogen and longer off-axis flight times. The included apertured and full angle spectra of  $Ni^{++}$  and  $Rh^{++}$  compare in the above manner. The maximum time resolution of gated images at full acceptance angle has been increased to 100 at a representative flight time of one microsecond and a gate width of 10 nanoseconds. The included gated micrographs show the spatial distributions of  $W^{3+}$  and  $W^{4+}$ ,  $Ni^{++}$  and  $P^{++}$  from Ni-P electroless plate, and  $H^+$  adsorbed on rhodium.

A preliminary application to the chemistry of hydrogen adsorbed on metallic solids displayed crystallographically and atomically specific variations in the distribution of adsorbed hydrogen over an undisturbed rhodium surface in an applied electric field. The variations in coverage observed in gated images of  $H^+$  have since been confirmed by energy-compensated atom-probe measurements. In addition, results indicate that adsorption occurs from the gas phase during both atom-probe analysis and hydrogen-promoted imaging.

The principal application is the atomic level metallurgical analysis of stripped Ni and Ni-P electro- and electroless deposited plates. The mass spectra of as-deposited Ni electroplate show it to be 99% pure, while field-ion micrographs show boundaries of atomic width between impinging crystals. Overall reorientation at depths of 30-150 atomic layers indicate a grain size of  $60-300\text{\AA}$ , while nearly uniform desorption patterns confirm extended perfect crystals are not present. The mass spectra of as-deposited Ni-P (2.7%) electroless plate and the annealed  $Ni_3P$ -Ni phase mixture show phosphorus content in agreement with expected values, while expanded Ni-P spectra show oxygen and a trace amount of chlorine. Field ion, desorption, and gated desorption micrographs show boundaries of atomic width in the otherwise amorphous Ni-P. Micrographs, after annealing, show an ordered overlayer rich in phosphorus indicating the segregation of phosphorus to the surface during the transformation to  $Ni_3P$ -Ni. The underlying structure is a mixture of ordered phases,  $Ni_3P$  and Ni, with boundaries that coincide with those present in Ni-P prior to the anneal. The existence and coincidence of the boundaries indicate Ni-P is not totally amorphous, in the sense of a liquid, as was previously thought.

UNCLASSIFIED

SECURITY CLASSIFICATION OF THIS PAGE (When Data Entered)

## ABSTRACT

This work concerns the development of a high resolution imaging atom-probe time-of-flight mass spectrometer, its performance, and its application to electro- and electroless nickel, nickel-phosphorus platings, and to hydrogen adsorbed on rhodium. An imaging atom-probe displays the distribution over a sample's surface of a constituent mass species selected from the sample's time-of-flight spectra.

Imaging of the sample surface is at atomic resolution by field-ion, desorption, and gated desorption microscopy.

The mass resolution of this 13.5-cm flight-path instrument was significantly increased by minimizing dispersion in the initial energy of field evaporated ions while improving timing and gating electronics. The mass resolution,  $m/\Delta m$ , at an acceptance angle of 5.4° is 150 at 20% above the base line. This is equivalent to the performance of one- to two-meter straight-flight-path atom-probes, and is shown by isotopic resolution  $W^{+++}$  and  $Ni^{++}$  mass spectra. Mass determinations remain accurate at the 31° full acceptance angle as the low mass side of spectral peaks is sharp; however, resolution is reduced to 50 by "tailing" ions resulting from premature evaporation induced by adsorbed residual hydrogen and longer off-axis flight times. The included apertured and full angle spectra of  $Ni^{++}$  and  $Rh^{++}$  compare in the above manner. The maximum time resolution of gated images at full acceptance angle has been increased to 100 at a representative flight time of one microsecond and a gate width of 10 nanoseconds.

The included gated micrographs show the spatial distributions of  $W^{3+}$  and  $W^{4+}$ ,  $Ni^{++}$  and  $P^{++}$  from Ni-P electroless plate, and  $H^+$  adsorbed on rhodium.

A preliminary application to the chemistry of hydrogen adsorbed on metallic solids displayed crystallographically and atomically specific variations in the distribution of adsorbed hydrogen over an undisturbed rhodium surface in an applied electric field. The variations in coverage observed in gated images of  $H^+$  have since been confirmed by energy-compensated atom-probe measurements. In addition, results indicate that adsorption occurs from the gas phase during both atom-probe analysis and hydrogen-promoted imaging.

The principal application is the atomic level metallurgical analysis of stripped Ni and Ni-P electro- and electroless deposited plates. The mass spectra of as-deposited Ni electroplate show it to be 99+% pure, while field-ion micrographs show boundaries of atomic width between impinging crystals. Overall reorientation at depths of 30-150 atomic layers indicate a grain size of 60-300 $\text{\AA}$ , while nearly uniform desorption patterns confirm extended perfect crystals are not present. The mass spectra of as-deposited Ni-P(2.7%) electroless plate and the annealed  $Ni_3P$ -Ni phase mixture show phosphorus content in agreement with expected values, while expanded Ni-P spectra show oxygen and a trace amount of chlorine. Field ion, desorption, and gated desorption micrographs show boundaries of atomic width in the otherwise amorphous Ni-P. Micrographs, after annealing, show an ordered overlayer rich in phosphorus indicating the segregation of

phosphorus to the surface during the transformation to Ni<sub>3</sub>P-Ni. The underlying structure is a mixture of ordered phases, Ni<sub>3</sub>P and Ni, with boundaries that coincide with those present in Ni-P prior to the anneal. The existence and coincidence of the boundaries indicate Ni-P is not totally amorphous, in the sense of a liquid, as was previously thought.

Accession For

NTIS GRA&I	<input checked="" type="checkbox"/>
DTIC TAB	<input type="checkbox"/>
Unannounced	<input type="checkbox"/>
Justification	
By	
Distribution	
Availability Codes	
Dist	Avail and/or Special
A	

## TABLE OF CONTENTS

	Page
ABSTRACT	iii
LIST OF FIGURES	vii
LIST OF TABLES	x
ACKNOWLEDGEMENTS	xi
I. INTRODUCTION	1
II. IMAGING ATOM-PROBE DESIGN	9
1. Principle of Operation	9
2. Vacuum and Gas Supply Systems	21
3. Tip Mount, Cold Finger, and Pulse Electronics	25
4. Timing and Oscilloscopic Electronics	36
5. Gate-Pulse and the Ion Detector	40
6. Angular Correction	46
7. Potential Measurements and Power Supplies	52
8. Imaging and Photography	53
III. PERFORMANCE AND CALIBRATION	54
1. Flight Equations	54
2. Time Dispersion and the Pulse Factor	61
3. Calibration, Final Flight Equations	79
4. Experimental Performance	58
IV. APPLICATIONS	104
1. Surface Distribution of Field Adsorbed Hydrogen	104
2. Atomic Analysis of Ni and Ni-P Deposits	112
V. SUMMARY AND CONCLUSIONS	135
APPENDIX: Detailed Electronics	139
BIBLIOGRAPHY	162

## LIST OF FIGURES

Figure	Page
1. Schematic diagram of the imaging atom-probe indicating the imaging and spectral mass detection modes . . . . .	10
2. Photographs of the imaging atom-probe: (a) evacuated flight chamber, (b) timing electronics, and (c) vacuum instrumentation . . . . .	11
3. Block diagram of the vacuum and gas supply system . . . . .	22
4. Photographs of tip section (a and b) and associated re-entrant feed-thrus (c-e) . . . . .	26
5. Oscilloscopic traces of the evaporation pulse: (a) measured at a 50 ohm termination and (b) measured at the tip . . . . .	37
6. Oscilloscopic traces of the timing sequence pulses (Tek. 485 scope, BW-350 MHz): (a) evaporation pulse into 50 ohms, (b) initial trigger from the evaporation pulser, and (c) initial and delayed output triggers from the variable time delay . . . . .	38
7. Oscilloscopic traces showing: (a) the jitter and delay between the time-mark and gate pulse, 10 traces; and the gating potential difference across the Chevron CEMA for (b) an 8 ns pulse and (c) a 1 MHz square wave . . . . .	42
8. Photographs of the gate pulse terminator (a) and the Chevron CEMA detector assembly (b) . . . . .	43
9. A tip-to-detector geometry using a spherical grid to induce on and off-axis ions to arrive nearly simultaneously at a flat detector . . . . .	49
10. A graphic and photographic display of field-ion image compression at large retarding potentials . . . . .	51
11. A simplified arrangement from which a pulse factor and time dispersion may be calculated. (a) System diagram, (b) spatial potential, (c) a potential resulting from a step pulse overshoot, and (d) an idealized pulse shape . . . . .	63
12. Time resolutions and pulse factors calculated for a few overshoot heights and widths. (a) The pulse factor's dependence on mass-to-charge and (b) a similar time resolution dependence . . . . .	75

## LIST OF FIGURES (cont.)

Figure	Page
13. The instrument's calibration curves: (top) the empirical correction to the absolute flight equation, and (bottom) the pulse factor determined from rhodium data . . . . .	82
14. Oscilloscopic time signals from a rhodium tip pulse evaporated in vacuum . . . . .	90
15. Histograms of $^{103}\text{Rh}^{++}$ time signals from a rhodium tip evaporated in vacuum . . . . .	92
16. Full characterization of a 011 oriented tungsten tip: (a) an oscilloscopic trace of the prominent charge states, (b) a single-pulse evaporation pattern, (c) a helium ion image, (d) a multilayer DC evaporation pattern, and (e,f) surface distributions of the two charge states . . . . .	95
17. Histogram showing isotopic relative abundances of $\text{W}^{3+}$ evaporated in vacuum . . . . .	98
18. A 111 oriented nickel tip imaged (a) with Ne and (b) by multilayer DC evaporation in vacuum . . . . .	100
19. Histograms of $\text{Ni}^{++}$ indicating the presence and relative abundances of nickel hydrides during evaporation in vacuum . . . . .	101
20. A 001 oriented rhodium tip imaged (a) with Ne and (b) by multilayer field evaporation in vacuum . . . . .	105
21. Oscilloscopic time signals showing the arrival of $\text{H}^+$ desorbed from a rhodium tip . . . . .	107
22. Desorption micrographs showing various degrees (a, b, and c) of selective field adsorption of hydrogen on the rhodium tip shown in Figure 20 . . . . .	109
23. A color composite displaying the atomically and crystallographically selective field adsorption of hydrogen on rhodium: (top) a field-ion micrograph of a 001 oriented rhodium tip with (bottom) a contrastingly colored, in superimposed hydrogen desorption micrograph . . . . . pocket	
24. Nickel and nickel-phosphorus chemically stripped plate material and mounted specimens . . . . .	113

## LIST OF FIGURES (cont.)

Figure	Page
25. Pure nickel electroplate as imaged with Ne . . . . .	115
26. Relative abundance histogram for pure nickel electroplate evaporated in vacuum . . . . .	118
27. Nickel-phosphorus electroless plate (as-deposited) imaged (a) with Ne, (b) by multilayer DC evaporation, and by multiple-pulse evaporation (c) gated for Ni <sup>++</sup> and (d) gated for p <sup>++</sup> . (e) Diagram of discernible atomic width boundaries . . . . .	122
28. Oscilloscopic traces of nickel-phosphorus electroless plate (as-deposited): (top) full mass sweeps with region intended for expansion intensified, (bottom) expanded mass sweeps of intensified region . . . . .	126
29. Relative abundance histograms for full and isotopic mass sweeps of as-deposited nickel-phosphorus . . . . .	127
30. The transition of Ni-P to ordered Ni-Ni <sub>3</sub> P as imaged with Ne. (a) As-deposited Ni-P electroless plate, (b) an ordered Ni-P overlayer after annealing at ~600°C for 20 s, and after field evaporation of (c) ~20 layers and (d) ~50 layers to show the underlying phase mixture of Ni and Ni <sub>3</sub> P with the retained atomic width boundaries . . . . .	130
31. Relative abundance histogram of ordered Ni-Ni <sub>3</sub> P showing the increase in phosphorus expected from the area occupied by Ni <sub>3</sub> P in Figure 30(d). . . . .	133
32. Cut-away view of the discharge line pulser . . . . .	140
33. Input and output trigger circuits for the evaporation pulser: (a) no-bounce, input trigger circuit, (b) output trigger circuit . . . . .	144
34. (a) A schematic representation of the discharge line pulser with (b) examples of its calculated and observed output pulses . . . . .	152
35. Calibration curves for the potential dividers . . . . .	160
36. Schematic diagram of the stepped DC power supply . . . . .	161

## LIST OF TABLES

Table	Page
1. Calculated mass-to-charge ratios for various materials field evaporated in vacuum . . . . .	86
2. List of parts for the evaporation pulser . . . . .	141

## ACKNOWLEDGEMENTS

The successful development and application of this imaging atom-probe has resulted from the co-operation between Prof. E. W. Müller, Prof. T. T. Tsong, Dr. S. V. Krishnaswamy, Mr. S. B. McLane, and the author.

In particular, the author wishes to acknowledge his indebtedness to the late Prof. E. W. Müller for his guidance during the formulation of the project and his active participation in its early stages. His ideas and suggestions were essential to the success of this work.

Thanks are due Mr. S. B. McLane for the wealth of electronics information he provided and for his collaboration in the development of the sophisticated electronics used in this instrument. Thanks are also due Mr. Yee S. Ng for his corroboration of the hydrogen adsorption study, and Dr. A. J. Melmed for his help in obtaining and preparing the Ni plate specimens used in this investigation.

The author wishes to express his gratitude to Mr. M. Herman and Mr. J. Sweeney for their assistance in various experiments and in the reduction of oscilloscopic mass data; and to Mr. G. Fowler for technical instruction in glass blowing, machining, and welding. Also, the author's special thanks are due Mrs. Carol Martinka for her help with the inking of technical drawings and in proofreading the manuscript.

Finally, the author's sincere thanks are due both Prof. T. T. Tsong and Prof. M. T. Pigott for their support and patience, and the Applied Research Laboratory of The Pennsylvania State University which supported this work under contract with the Naval Sea Systems Command.

## I. INTRODUCTION

An imaging atom-probe<sup>1</sup> is a field-ion, field-desorption microscope combined with an *in situ* time-of-flight, gated-desorption mass spectrometer. Such an instrument was attempted by Müller et al.<sup>2,3,4</sup> in 1972 after Müller and Walko<sup>5</sup> obtained the first successful field-desorption micrographs of tungsten in 1971. The necessarily short drift distance and large capacity of the channel plate detector resulted in low mass resolution which discouraged further development. Panitz<sup>6,7,8</sup> continued to develop a similar instrument from 1973 through 1975, and introduced significant improvements in design and timing electronics, e.g., a curved chevron-microchannel plate detector concentric to the specimen, tip, and successful time-gating of this detector. However, a low mass resolution,  $m/\Delta m$  of  $60^9$  persisted and continues to limit applications and possibly reliability.<sup>10,11,12,13</sup>

Nevertheless, the technique has been applied by Panitz, Waugh, and Wagner to a variety of problems: the distribution by gated-desorption image of the charge states of field evaporated tungsten and iridium ions<sup>7,8,14</sup> over the tip surface, similar distributions of He and Ne field-adsorbed on W and Ir,<sup>8,14</sup> the distribution of hydrogen field-adsorbed over an iridium tip and localized to carbon impurities within the iridium lattice,<sup>15,16</sup> the depth profile of deuterium ions implanted in tungsten,<sup>17</sup> the display of oxygen segregated to a grain boundary in molybdenum,<sup>18</sup> and the distribution of iron precipitates in a copper one atomic percent iron alloy.<sup>19</sup> More recently, Waugh<sup>20</sup> has imaged the

distribution of Ni-Al precipitates in drawn and heat-treated (17 Cr, 7 Ni, 1 Al, 0.7 Mn, 0.5 Si) stainless steel, while Panitz and Giaever have attempted to image protein macromolecules by desorbing an overlayer of adsorbed benzene.<sup>21,22</sup> In addition, Kellogg and Panitz<sup>23,24</sup> by means of comparison to deuterium ion implantation have attempted to probe the plasma-wall interaction in the Princeton Large Torus Tokamak. The degree of success in the above applications is by no means uniform with the metallurgical studies by Waugh and the localized adsorption of hydrogen by Panitz being the most demonstrative of the capability of the instrument.

A recent variation in approach was the introduction of laser-induced desorption and ionization in complementary papers by Kellogg and Tsong<sup>25</sup> and Drachsel, Nishigaki, and Block,<sup>26</sup> which demonstrated laser-induced atom-probe mass spectroscopy,  $m/\Delta m(10\%) \approx 30$  at a drift distance of 13 cm, and photon-induced field ionization mass spectroscopy,  $m/\Delta m(10\%) \approx 100$  at a drift distance of 30 cm, respectively. Although the data presented for the 13-cm laser-induced atom-probe exhibited low resolution, laser-induced desorption may yield significantly improved mass resolution as the initial impulse evaporating metallic ions is probably thermal. An energy spread of several  $kT$  would be at least two orders of magnitude smaller than the several hundred electron volt dispersions<sup>27</sup> common to electrically pulse desorbed ions. Hence, a laser pulse one nanosecond or less in width may improve resolution at heavier masses by a factor of ten. The laser approach is particularly promising as the improved mass resolution,  $m/\Delta m(10\%) \approx 100$  at a drift distance of 14 cm, obtained

by this author<sup>28</sup> and presented in this thesis results from minimizing the initial energy dispersion in electrically pulse evaporated ions by reducing the effective pulse width.

The basic instrumentation, principles, and phenomenon of imaging, straight, and energy compensated time-of-flight atom-probes are presented in review articles by Panitz,<sup>1,9</sup> Müller and Tsong,<sup>29</sup> and Müller and Krishnaswamy.<sup>10</sup> The articles by Panitz deal explicitly with the imaging atom-probe, its unique gated-image capability, and its relation to other surface techniques. Imaging at atomic resolution by the field ionization of an ambient gas and by field evaporation of the specimen lattice are reviewed in an article by Müller.<sup>30</sup> In particular, evaporation images show crystallographic variation in yield<sup>31,32,33</sup> which is pertinent to the interpretation of gated-desorption images and aiming<sup>34</sup> of straight and energy compensated atom-probes. Finally, the theory of field ionization, image gas adsorption, and field evaporation are reviewed in the above article<sup>29</sup> by Müller and Tsong. These publications present the basis and general state of development of the atom-probe technique, and indicate the enormous contribution of Erwin W. Müller.

Although the imaging atom-probe manages the formidable tasks of atomic resolution imaging and single atom detection, identification, and display, the instrument has retained the esthetic simplicity of its predecessor the field-ion microscope.<sup>35</sup> Hence, a million fold magnified image of the 200-1000 Å radius apex of a needle-shaped specimen, tip, is obtained by radially projecting positive ions from the apex surface a distance of ~14 cm onto a Chevron Channeltron Electron

Multiplier Array, Chevron CEMA,<sup>36</sup> whose output is proximity focused onto a phosphor screen. The imaging gas, adsorbate, or lattice atoms are ionized and then projected by a 2-5 V/Å electric field at the apex surface. This field is obtained by applying a 2-20 kV positive potential to the tip. When a portion of the tip potential is provided by a nanosecond, ns, high voltage pulse, the instant ions are induced to evaporate is strictly correlated in time to the instant they are detected by the Chevron CEMA - phosphor screen assembly. Correlation is achieved by using a small fraction, 0.4%, of the evaporation pulse to trigger a variable, nanosecond-incremented time delay, which, after a selected interval,  $\pm 0.5$  ns, triggers either an oscilloscope or a second high voltage pulser. During the oscilloscope sweep, the Chevron CEMA (at a gain of  $10^7$ ) develops a signal pulse voltage of  $\sim 20$  mV per incident ion across a 50-ohm, screen load resistor. The ion's signal and delay's fiducial mark appear on the same trace, and the ion's flight time is the delay setting plus the interval between the fiducial mark and the ion's signal. This oscilloscopic time-of-flight spectrum is used to calculate the evaporated ion's mass-to-charge ratios, and to select a species whose distribution over the apex surface is of interest. The desired distribution is obtained by triggering a second high voltage pulser which "gates" or activates the Chevron CEMA for a period of only 8 ns about the preselected species arrival time. Hence, only the selected species is imaged on the phosphor screen. The resulting gated-desorption image and the time-of-flight traces, 25 per frame, are recorded photographically.

The imaging atom-probe whose operation is discussed in the preceding paragraph was designed and constructed almost entirely by this author; and, although, its basic operation is similar to other imaging atom-probes, it incorporates a number of improvements<sup>37</sup> which have reduced the initial energy spread of pulse evaporated ions and increased stability, resolution, and accuracy. For example: the energy dispersion of evaporated ions is reduced by using a subnanosecond width initial pulse overshoot as the actual evaporation pulse; the absolute and relative flight-time uncertainty is reduced, 2 and 0.2 ns, respectively, by providing an absolute time reference,  $\pm 0.5$  ns, whose fiducial mark is positioned to any desired point on the oscilloscopic trace; finally, the jitter in the gate location is only  $\sim 1$  ns, and its width is reduced to 8 ns by pulsing the Chevron's two microchannel plates in series to reduce their capacitive load. These improvements have resulted in a spectral mass resolution,  $m/\Delta m$ , at an acceptance angle of  $5.4^\circ$  of 150 at 20% above the base line.<sup>28</sup> This is fully equivalent to the best resolution<sup>38</sup> obtained by one- and two-meter straight time-of-flight atom-probes, and it is a threefold increase as compared with other<sup>39</sup> short, 10-15 cm, atom-probe time-of-flight spectrometers. In addition, the 8 ns gate width provides an increased maximum gated-image resolution of 100 at a representative flight time of one microsecond. The demonstrated discrimination of one amu out of 200 is sufficient for reliable surface physics and metallurgical applications; and, as such, it is a significant development of the imaging atom-probe technique.

The first portion of this thesis presents the instrumental improvements indicated in the previous paragraph and sufficient results, w,

Ni, and Rh isotopic spectra, to demonstrate the performance. In addition, gated-images of the distribution of hydrogen field-adsorbed on rhodium are presented, their reliability having been confirmed by subsequent corroborating results obtained by Yee S. Ng with the energy-deficit compensated atom-probe.<sup>40</sup> Further, a rudimentary theory relating the pulse factor,  $\alpha$ ,<sup>41</sup> to energy deficits<sup>42</sup> and dispersions is presented as a basis for the calibration procedure employed in obtaining the value of  $\alpha$ . This calibration procedure, unlike previous methods,<sup>41</sup> does not present  $\alpha$  as the parameter required to converge the standard and calculated, via an approximate flight equation, mass-to-charge ratios; rather,  $\alpha$  appears as the parameter in the flight equation by which the difference between observed and calculated flight times is made independent of the varying pulse fraction of the potential. Hence, the pulse factor does not mask errors in the assumed form of the electrostatic flight equation, and these may be corrected independently. An independent correction to the flight equation is employed when a retarding potential is used to aid in correcting ion trajectories to a flat Chevron CEMA (a spherically curved Chevron CEMA was not available). Most importantly, the flight equation containing  $\alpha$  does not explicitly appear in relative mass determinations since it is nearly electrostatic. Hence, relative mass determination remains extremely accurate, 0.1%, depending only on the accurate measurement of observed flight times and the instrumentation delay,  $\delta$ .<sup>41</sup>

The second portion of this work presents the first imaging atom-probe atomic level analysis of stripped Ni and Ni-P electro- and electroless plate.<sup>28</sup> Nickel electroplate and nickel phosphorus electroless

plate represent the majority of material plated by each process, and both have had their properties (composition, structure, density, porosity, internal stress, and adhesion, etc.) studied by a variety of techniques (chemical analysis, spark source mass spectroscopy, x-ray and electron diffraction, auger, transmission and scanning electron microscopy, and metallography, etc.).<sup>43</sup> In addition, "amorphous" Ni-P electroless plate possesses the character of a "metallic glass",<sup>44,45</sup> and such materials are currently being investigated by field-emission<sup>46</sup> and field-ion<sup>47</sup> microscopy, atom-probe,<sup>48</sup> and the author's imaging atom-probe.<sup>28</sup> The results presented here demonstrate that plated materials may be investigated by the atom-probe technique, and, particularly for Ni-P, that new and significant information on the nature of these materials can be obtained at present only by the unique capabilities of the imaging atom-probe. This study of Ni-P electroless plate identified atomic width boundaries in a material thought to be totally amorphous,<sup>45</sup> and these boundaries coincide to those in the mixture of ordered Ni<sub>3</sub>P and Ni phases obtained by annealing the as-deposited Ni-P plate. In addition, field-ion micrographs taken after annealing show an ordered overlayer rich in phosphorus, indicating that phosphorus segregates to the surface during the transformation to Ni<sub>3</sub>P, Ni. The nickel and nickel phosphorus plates used in this study were obtained and prepared with the help of A. J. Melmed at the National Bureau of Standards.

This work was begun in 1976 with Erwin W. Müller as the "Atomic Microstructure and Analysis of Electroplatings," and it was supported by the Applied Research Laboratory of The Pennsylvania State University

under contract with the Naval Sea Systems Command. The work was continued after Erwin W. Müller's death on May 17, 1977 with Tien-Tzou Tsong and S. V. Krishnaswamy, and it was completed by this author and T. T. Tsong in August 1979. Finally, an extension of this work will be pursued by this author and A. J. Melmed at the National Bureau of Standards.

## II. IMAGING ATOM-PROBE DESIGN

The imaging atom-probe is a field-ion and desorption microscope with an in situ time-of-flight and gated-image mass spectrometer. The device, in principle, is relatively simple: the tip apex is imaged at atomic resolution by radially projecting field-ionized, desorbed, or evaporated ions onto a detector-phosphor screen assembly of single particle sensitivity; the mass-to-charge ratio of pulse field-desorbed or evaporated ions is determined from their measured flight time (tip to detector); and the distribution over the apex surface of a selected mass species is obtained by activating the detector only about the arrival time of the ions of interest. A schematic diagram of the device is presented in Figure 1; and Figure 2 shows the evacuated flight chamber, timing electronics, and vacuum instrumentation. Together, these figures indicate the stringent ultrahigh vacuum techniques and state-of-the-art electronics which must be employed to obtain reliable, high-resolution performance. In addition, provisions for heating and cryogenic cooling of the tip as well as for the controlled admittance of pure gases are necessary to the proper and versatile operation of this microanalytical device.

### 1. Principle of Operation

The field-ion image of the apex surface is obtained in the conventional manner. First, an imaging gas, e.g., He or Ne, is admitted at a rate sufficient to maintain a dynamically stable pressure of  $\sim 4 \times 10^{-6}$  Torr<sup>†</sup> against a slow, retained pumping speed. A positive

<sup>†</sup>1 Torr (mm Hg @ 0°C) is equal to 133.32 Pascal (Nt/m<sup>2</sup>).

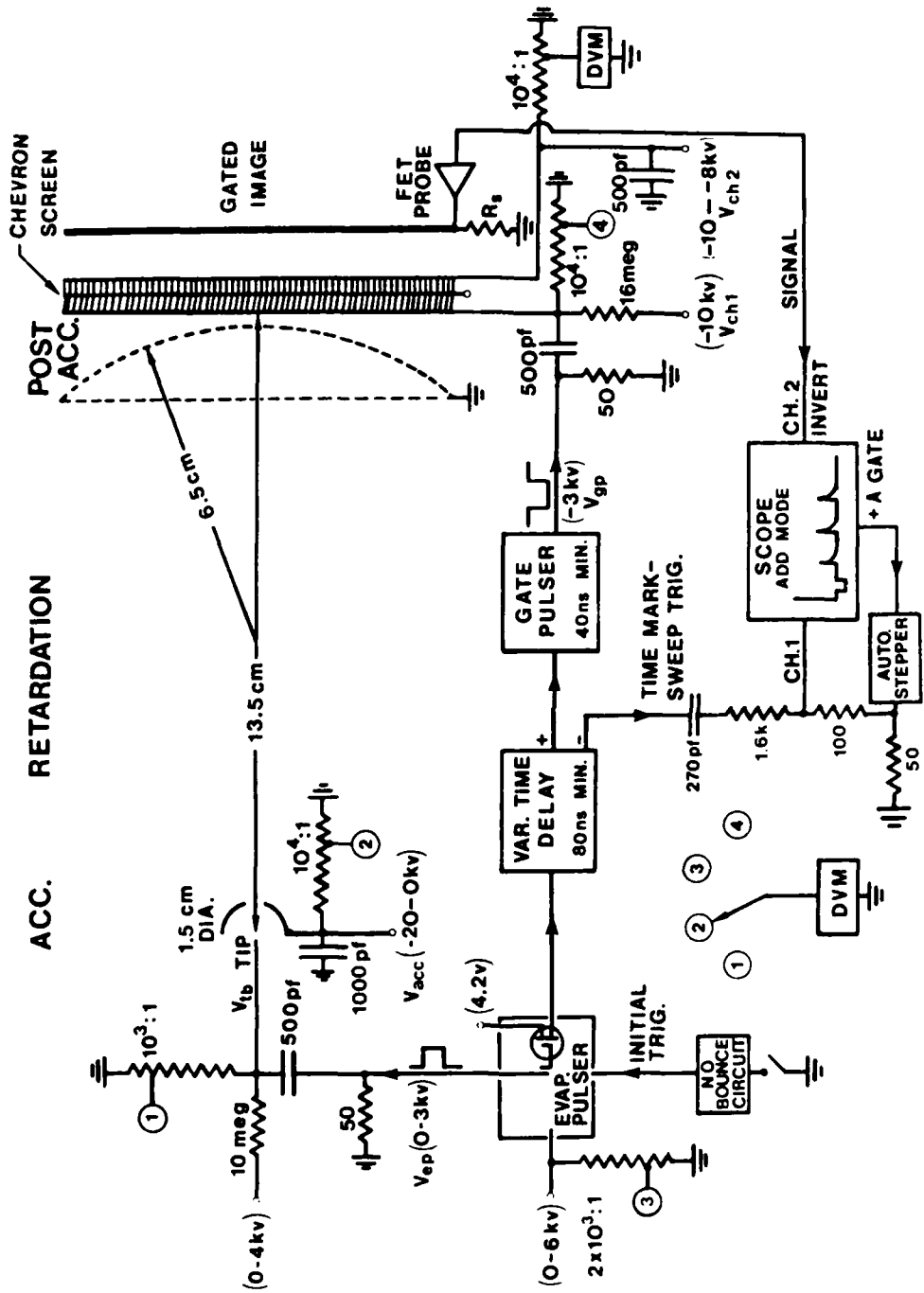


Figure 1. Schematic diagram of the imaging atom-probe indicating the imaging and spectral mass detection modes.

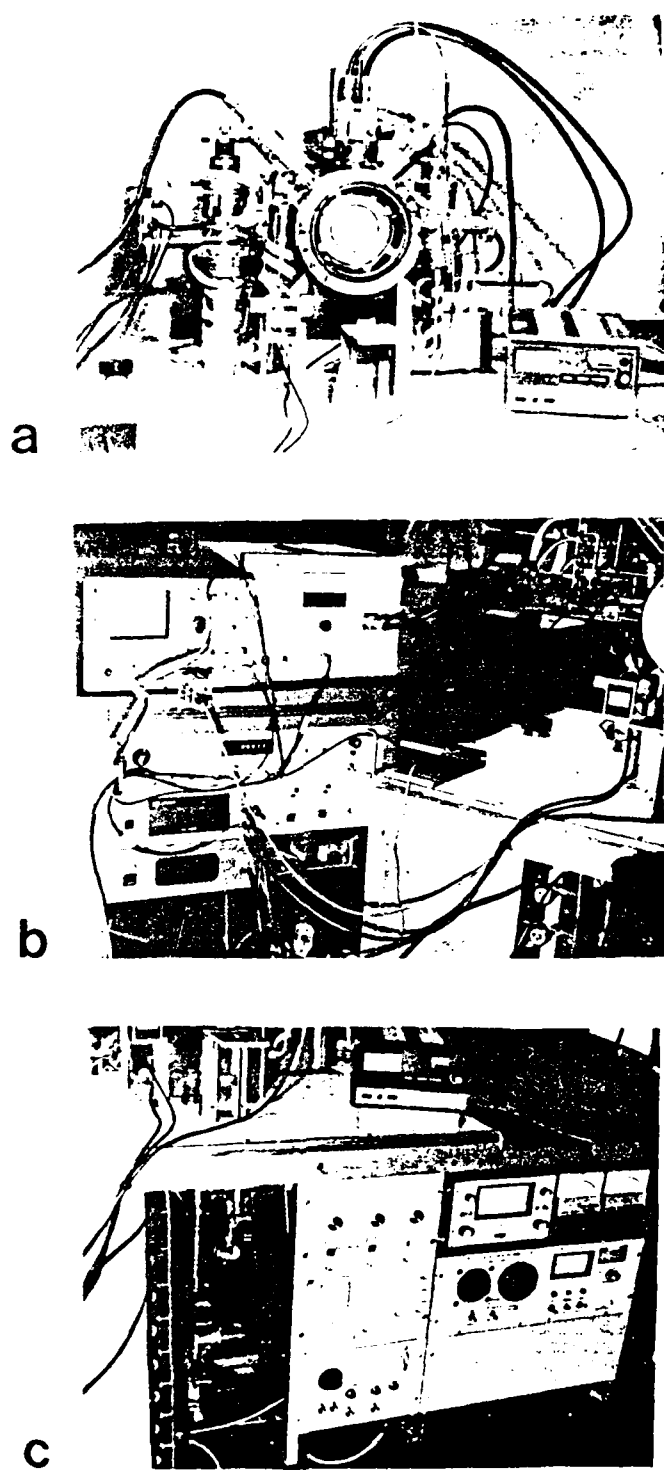


Figure 2. Photographs of the imaging atom-probe: (a) evacuated flight chamber, (b) timing electronics, and (c) vacuum instrumentation.

potential,  $v_{tb}$ , is then applied to the tip, while a zero or negative potential,  $v_{acc}$  or  $v_a$ , is applied to the concentric, 1.6-cm diameter (actual values are slightly larger than their representative values in Figure 1) hemispherical counter electrode. The potential difference,  $v_{DC}$ , between the tip and counter electrode is given by

$$v_{DC} = v_{tb} + |v_a| \quad (2.1)$$

and results in a high electric field strength at atom locations on the cryogenically cooled apex surface. The imaging gas atoms are ionized at these locations and projected toward the Chevron CEMA detector. The projection remains nearly<sup>49</sup> radial throughout the 13.8-cm flight path provided  $v_{tb}$  represents 10% or more of  $v_{DC}$ . As shown in Section 6 of this chapter, this condition on  $v_{tb}$  avoids the lens effect<sup>10</sup> associated with the almost radial retardation scheme which can be employed with this instrument. Finally, the projected positive ions which strike channels in the Chevron CEMA, gain of  $10^3$ - $10^4$ , yield "electron showers" at the channel outputs. These "electron showers" are proximity focused by the potential difference,  $v_{ch2}$ , between the Chevron output plate and the ~1.5-mm distant phosphor screen. The incidence of these electrons on the phosphor screen provides the atomically resolved and intensified ion-image of the apex surface.

The ion optics of field desorption and field evaporation are nearly<sup>31</sup> identical to those of field-ion imaging. Hence, the surface species, adsorbate or lattice atoms, which are removed by these processes, as positive ions, can be used to self-image their location or point of origin on the apex surface. The self-imaging in vacuum

is achieved by using the full gain,  $\sim 10^7$ , of the Chevron CEMA to image, via the phosphor screen, the impact position of single, incident evaporated or desorbed ions. The rate at which atoms are removed by these processes is well defined by the electric field strength at the apex surface; and, therefore, it may be controlled by either the magnitude of  $V_{DC}$  or by both the magnitude and duration<sup>50</sup> of a positive, high voltage evaporation pulse,  $V_{ep}$ , superimposed on  $V_{tb}$ . Fractional through multilayer (multiple atomic layers) desorption or evaporation patterns may be obtained by either method; however, those obtained by pulsing are usually designated as "single-pulse (shot)" or "multiple event" desorption or evaporation patterns. These desorption and evaporation patterns contain image contributions from all removed species without discrimination.

Discrimination between removed species, single species imaging and identification, may be realized through pulse evaporation or pulse desorption of the atomic constituents of the apex surface. The 18.4-ns wide evaporation pulse applied to the tip in this instrument has a rise time of  $\sim 0.3$  ns and a leading edge "overshoot". The base-width of the "overshoot" is  $\sim 0.6$  ns, and its amplitude, as indicated in Chapter III, is probably  $0.6 V_{ep}$ . As the evaporation rate is field sensitive, the "overshoot" acts as the effective evaporation pulse with the majority of the observed ions evaporating during an extremely brief interval about its peak amplitude. The ions evaporated during this instant arrive in sequence, according to their mass-to-charge ratio, at the Chevron CEMA, and their instants of detection,  $\sim 0.1$ -ns jitter, appear as voltage pulses at the screen resistor,  $R_s$ , indicated in

Figure 1. These mass signals are applied to channel 2 of a dual-channel oscilloscope where they appear on a trace whose sweep is initiated by a trigger correlated, in time, to the instant of evaporation. The trigger also appears, via scope-channel 1, as a fiducial time-mark on the same trace. The time-mark's position, in time, on the trace is set by the 1 ns-incremented, variable time-delay as indicated in Figure 1, and this delayed position with respect to the evaporation event is set with an absolute accuracy of ~0.5 ns. The integer delay setting plus the remaining interval between the time-mark and a mass signal yield the ion's flight time. Hence, the oscilloscopic display is an accurate time-of-flight spectrum of the evaporated ions. Finally, the evaporated species are identified according to their calculated mass-to-charge ratios by inserting the measured flight times and potentials into the flight equation for the instrument.

Once a species is selected from the time-of-flight spectra, its distribution over the surface of the apex may be obtained as a gated-desorption or gated-evaporation image. This is accomplished by setting the time-delay so that the time-mark is positioned 30 ns ahead of the selected species' arrival time. The time-delay is now set to trigger the high voltage, Krytron gate-pulser at the proper instant; so that, it may, in turn, activate the Chevron CEMA for a period of 8 ns about the selected species' arrival time. Both single-pulse and multiple-event images of a single species' distribution are obtained in this manner.

When the instrument is operated in the free-flight mode,  $V_a$  at ground potential, the approximate on-axis flight equation is relatively simple and is derived here to illustrate the pertinent parameters.

Consideration of the evaporated ions' energy during flight yields the following analysis.

The ions are evaporated at the beginning of an 18.4-ns pulse, which is longer than their travel times in the acceleration region near the tip. If there were no pulse "overshoot", an evaporated ion would attain a kinetic energy given by

$$\frac{1}{2} mv^2 = ne(v_{DC} + v_{ep}) \quad , \quad (2.2)$$

where  $ne$  is the ion's charge and  $v$  its terminal velocity. However, a necessary time-dependent "overshoot" is present and may be accounted for as an additional electrostatic contribution to the ion's energy by a pulse factor,  $\alpha$ . That is:

$$\frac{1}{2} mv^2 = ne(v_{DC} + \alpha v_{ep}) \quad . \quad (2.3)$$

Such a pulse factor is considered in detail in Chapter III and is nearly constant with respect to the ion's mass and the pulse fraction of the total potential.

Since the acceleration region near the tip is short compared to the total flight path,  $R_T$ , of 13.8 cm, the ion's free-flight travel time is given as

$$t \approx \frac{R_T}{v} \quad . \quad (2.4)$$

Combining equations (2.3) and (2.4) identifies the ion by its calculated mass-to-charge ratio,

$$\left(\frac{m}{n}\right) = \frac{K(v_{DC} + \alpha v_{ep}) t^2}{R_T^2} \quad , \quad (2.5)$$

where

$$K = 2(e/\text{amu}) \quad (2.6)$$

and  $(m/n)$  is expressed in atomic mass units (amu). If the distance, potential, and time are measured in meters, volts, and seconds, respectively, then,

$$K = 1.9305 \times 10^8 \text{ coul/kg} . \quad (2.7)$$

The travel time in equation (2.5) is the observed flight-time,  $t_{ob}$ , plus the net instrumentation delay,  $\delta$ . Hence, equation (2.5) is rewritten as

$$\left(\frac{m}{n}\right) = \frac{K(v_{DC} + \alpha v_{ep})(t_{ob} + \delta)^2}{R_T^2} . \quad (2.8)$$

Equation (2.8) is absolute as an unknown species may be identified without reference to a known mass if  $\alpha$  and  $\delta$  have been determined. The value of  $\delta$  may be obtained either from the relative flight-times of known masses, assuming  $\alpha$  is constant, or by direct measurement of instrumental delays as in Appendix equation (A.2), where

$$\delta = 119.7 \pm 2 \text{ ns} .$$

As  $\delta$  is now known,  $\alpha$  may be determined for a known mass, e.g., single isotopic rhodium, by equation (2.8). However, the closed form of the instrument's actual flight equation is not as well known as equation (2.8); therefore,  $\alpha$  must be obtained by the slightly more general approach presented in Chapter III which yields

$$\alpha = 1.15 \pm 0.06 .$$

The instrument's absolute accuracy may be estimated by differentiating equation (2.8) and then dividing the result by equation (2.8). This yields the maximum fractional error in  $m/n$ ,<sup>41</sup>

$$\frac{\Delta(m/n)}{(m/n)} = \frac{\Delta V_{DC} + \alpha \Delta V_{ep} + \Delta \alpha V_{ep}}{V_{DC} + \alpha V_{ep}} + \frac{2(\Delta t_{ob} + \delta)}{t_{ob} + \delta} + \frac{2\Delta R_T}{R_T} . \quad (2.9)$$

As indicated in equation (2.9), accuracy is adversely effected by errors in potentials ( $\Delta V \approx 1$  V), the flight time ( $\Delta t_{ob} \approx 1$  ns), and the flight path ( $\Delta R_T \approx 1$  mm). The given estimates reflect the uncertainty of the digital voltmeter, the resolution limit of applicable oscilloscope sweeps (e.g., 10 ns/cm), and the uncertainty in the 13.8 cm tip-to-detector distance, respectively. Substitution in equation (2.9) of representative  $^{182}\text{W}^{+++}$  free-flight data ( $V_{DC} = 3590$  V,  $V_{ep} = 679.2$  V,  $t_{ob} + \delta = 1170$  ns) and for the remaining terms given above yields a fractional error in  $m/n$  of 0.029. This represents an error in mass determination of  $\pm 1.8$  amu at  $(m/n) = 60.65$  amu. The larger part of this error is due to the uncertainty in  $\alpha$  and in the measured flight path. This portion of the error may be eliminated and the remainder reduced if a known mass is present and an absolute time reference is available.

A time reference is provided on each oscilloscopic trace in the form of a time-mark. This fiducial signal is positioned on the trace by absolute delay times,  $D$ , accurate to  $\pm 0.5$  ns. If a known species,  $(m/n)_0$ , and various unknown species,  $(m/n)_x$ , are present, their measured flight times may be written as

$$t_0 = D_0 + \tau_0 + \delta \quad \text{and} \quad t_x = D_x + \tau_x + \delta \quad . \quad (2.10)$$

In these expressions,  $\tau_0$  and  $\tau_x$  are the remaining oscilloscopic intervals between the time-marks and their associated mass signals. In addition, the known species and any  $(m/n)_x$  may be expressed by equation (2.5). That is:

$$\left(\frac{m}{n}\right)_0 = \frac{K(V_{DC} + \alpha V_{ep}) t_0^2}{R_T^2} \quad \text{and} \quad \left(\frac{m}{n}\right)_x = \frac{K(V_{DC} + \alpha V_{ep}) t_x^2}{R_T^2} \quad . \quad (2.11)$$

When the flight equation for the known species, the first of equation (2.11), is divided into the unknown species' flight equation, the second of equation (2.11), one obtains

$$\left(\frac{m}{n}\right)_x = \left(\frac{m}{n}\right)_0 \left(\frac{t_x}{t_0}\right)^2 \quad . \quad (2.12)$$

Equation (2.12) is a relative flight equation by which unknown species are identified in terms of a known, reference species and their directly measured flight times, equation (2.10). In fact, it is the general relative flight equation for this instrument, since it does not explicitly depend on the form of the electrostatic potential.

When equation (2.12) is applied to species identification in Chapters III and IV,  $t_0$  and  $t_x$  are simply entered as observed flight times without enumerating  $D$ ,  $\tau$ , and  $\delta$ . In addition, many applications, e.g., isotopic abundance, hydrides, etc., require only a single time

reference to maintain accuracy, since the known and unknown species' flight times are similar. In this case, the measured flight times would be given as

$$t_0 = D_0 + \tau_0 + \delta \text{ and } t_x = D_0 + \tau_x + \delta \quad . \quad (2.13)$$

Finally, requiring a reference species is not restrictive, since at least one can usually be readily recognized; and, if not, one may be provided as an ambient gas, Ne, Ar, etc.

If a known reference species is present, the instrument's improved accuracy may be calculated by differentiating equation (2.12) and dividing the result by equation (2.12). This yields the maximum fractional error in  $\left(\frac{m}{n}\right)_x$ ,

$$\frac{\Delta\left(\frac{m}{n}\right)_x}{\left(\frac{m}{n}\right)_x} = 2 \left[ \frac{1}{t_x} + \frac{1}{t_0} \right] \Delta t \quad . \quad (2.14)$$

Here, the uncertainty in both measured flight times has been set equal; and it,  $\Delta t$ , is obtained by differentiating equation (2.10). That is:

$$\Delta t = \Delta D + \Delta \tau + \Delta \delta \quad . \quad (2.15)$$

In equation (2.15), the error in both the delay setting ( $\Delta D \approx 0.5$  ns) and the measured instrumentation delay ( $\Delta \delta \approx 2$  ns) are as given previously; and the oscilloscopic uncertainty,  $\Delta \tau$ , still depends upon the sweep employed. The accurately positioned time-mark permits

expanded sweep measurements irregardless of known-unknown separation.

At sweeps of 10 ns/cm, this allows identification at an oscilloscopic uncertainty of 0.5 ns. However, the abundances of widely dispersed species, once identified, are still obtained at longer sweeps since the above accurate identification measurements are not simultaneous.

An estimate of the fractional error in a relatively identified  $\left(\frac{m}{n}\right)_x$  may now be obtained and compared to the fractional error previously determined, by equation (2.9), for  $^{182}\text{W}^{+++}$ . This is done by considering the relative identification of the remaining isotopes of tungsten. Since the separation between  $^{182}\text{W}^{+++}$  and the remaining isotopes,  $\left(\frac{m}{n}\right)_x$ , is small,  $t_x$  is similar to  $t_0$ . Therefore, equation (2.14) may be written as

$$\frac{\Delta \left(\frac{m}{n}\right)_x}{\left(\frac{m}{n}\right)_x} \approx \frac{4}{t_0} (\Delta D + \Delta \tau + \Delta \delta), \quad (2.16)$$

where  $\Delta \tau$  is the uncertainty in the measured oscilloscopic intervals between a time-mark and either  $^{182}\text{W}^{+++}$  or another isotope. Substitution in equation (2.16) of the 1170 ns flight time of  $^{182}\text{W}^{+++}$ ,  $t_0$ , and the uncertainties given above yields a fractional error in  $\left(\frac{m}{n}\right)_x$  of 0.01. The error in a mass determination for  $^{184}\text{W}^{+++}$  (61.32 amu) would then be  $\pm 0.63$  amu, which is about 3 times smaller than the comparable error,  $\pm 1.8$  amu, for an absolute determination.

The majority of the estimated error in relative identification is the conservative 2 ns uncertainty in the instrumentation delay. If

pursued further by direct measurement, as in the Appendix,  $\Delta\delta$  could be reduced to less than 1 ns. This uncertainty is less than that of an alternative calibration using equation (2.12). That is, errors due to  $\alpha$ 's mass dependence and the measurement of widely different flight times for known species are avoided. Inevitably,  $\Delta\delta$  may be reduced to 0.2 ns, which is the jitter in the detection and timing electronics. For the example treated above, this would reduce the error in mass determination to  $\pm 0.25$  amu at a (m/n) of 61.32 amu. This is comparable to the error observed in identifying the isotopes of tungsten from free-flight data.

## 2. Vacuum and Gas Supply Systems

For reasons which are apparent in considering a time-of-flight mass spectrometer of single ion sensitivity and for the control of gaseous adsorbates, this instrument has been constructed as an ultra-high vacuum device. Figure 3 is a block diagram of the vacuum and gas supply systems.

The vacuum chamber, oil diffusion pump, and gas manifold forelines are joined by a tee configuration of valves to a common molecular sieve trap through which they are pumped separately by a single mechanical pump. Once isolated from the foreline, the vacuum chamber or gas manifold is further evacuated by a liquid nitrogen trapped, oil diffusion pump. In addition, the vacuum chamber is continuously pumped during operation by an integral cryogenic and titanium sublimation pump, while selected gases may be admitted through a liquid nitrogen trap.

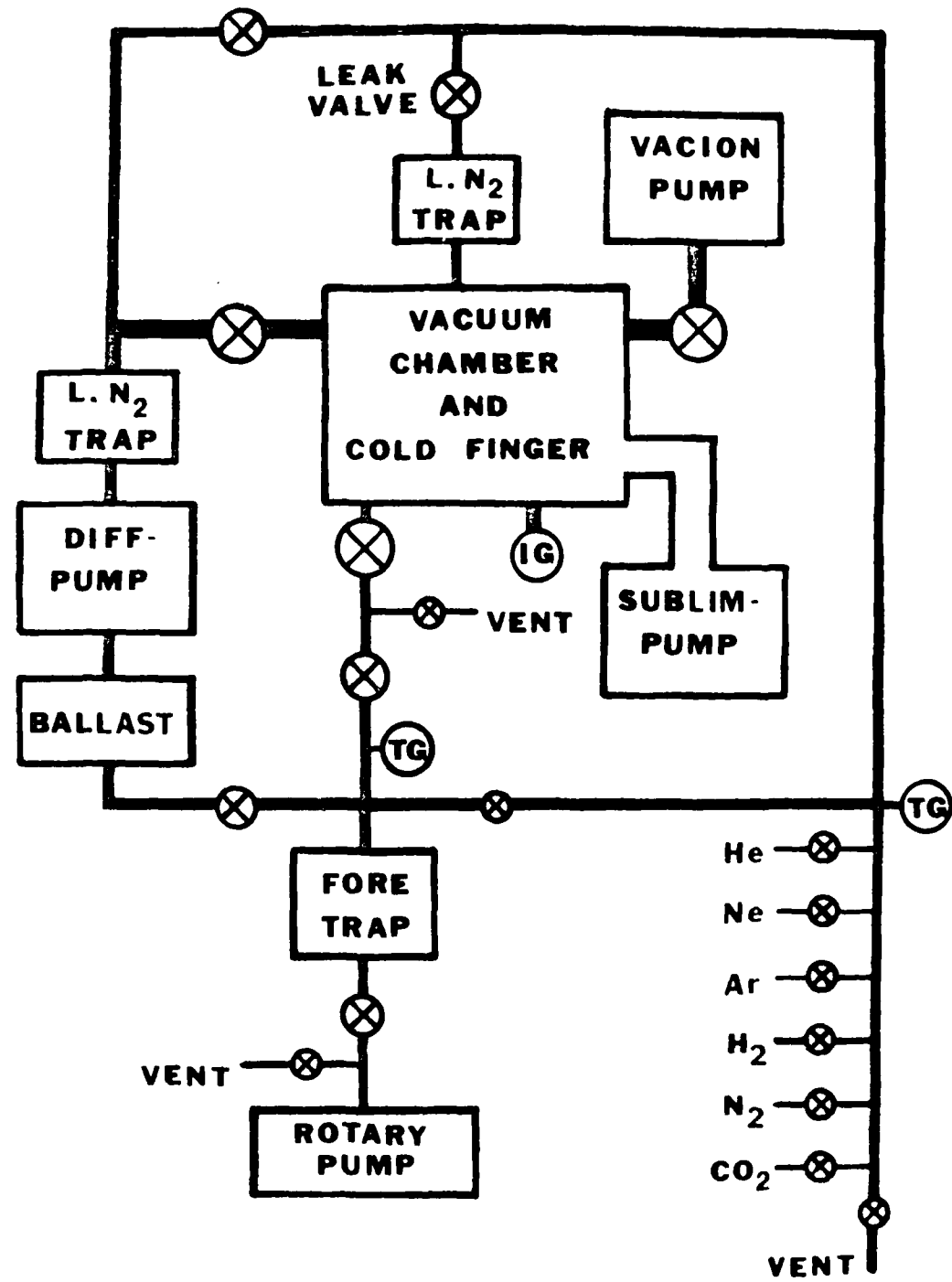


Figure 3. Block diagram of the vacuum and gas supply system.

by a controlled leak valve. Further, the diffusion pump is applied whenever appropriate during the course of an experiment. During those periods in the life of a specimen when an experiment is not in progress, the chamber's ultrahigh vacuum is maintained by the Vac Ion pump. The various pumps are applied or isolated at the chamber by three gold seal, ultrahigh vacuum valves. Either a nude ionization gauge or a cold cathode discharge gauge, integral to the Vac Ion pump, is used to measure the chamber pressure, while thermocouple gauges are employed in the remaining sections of the instrument. Finally, various sections of the instrument may be vented separately; and, in particular, the main vacuum chamber is separately vented to dry nitrogen during specimen exchange. This reduces pump-down time by minimizing the amount of water adsorbed onto the large surface area of the Chevron CEMA detector.

The vacuum chamber, like much of the vacuum system, is constructed of heliarc welded 304 stainless steel. Other chamber components, windows, feed-thrus, Chevron detector, etc., are constructed of materials, glass, ceramic, etc., which are also ultrahigh vacuum compatible and bakeable. As a result, a stable background pressure of  $\sim 3 \times 10^{-9}$  Torr is attained, without baking, 18 hours after a specimen is exchanged. The chamber is pumped overnight by the liquid nitrogen trapped, oil diffusion pump and, subsequently, by both gettering of the sublimation pump and cryogenic cooling. Generally, this exchange procedure provided a working background pressure in a reasonable turn-around time without baking the system. If a further reduction in background pressure is desired, the chamber and its associated components may be baked to  $200^{\circ}\text{C}$  by a 3000-watt system of thermostatically controlled

flexible, Briskeat heating tapes. For example, baking at 170°C for 4 hours and, subsequently, both cooling and gettering yields a background pressure of  $\sim 3 \times 10^{-10}$  Torr.

Standard ultrahigh vacuum equipment has been utilized wherever possible. The system's pumps consist of: a 30 l/s, Varian, Vac Ion pump; a cryogenically cooled, 0.03 g/h @ 44 amperes, Varian, cartridge, titanium sublimation pump; a 150 l/s, Edwards, E02, oil (ultimate pressure  $< 10^{-10}$  Torr) diffusion pump; and a 100 l/min, ED-100, Edwards, mechanical pump. The oil diffusion pump is trapped by a Grandville-Phillips, 2-in. I.D., Cryosorb cold trap to minimize oil creep and back-streaming; while the output of the Grandville-Phillips variable, 100 to  $10^{-10}$  cc/s, leak valve is liquid nitrogen trapped to remove condensable gaseous impurities. At the main chamber, there are two series 205, 2-in., and one series 204, 1-in., gold seal, Grandville-Phillips valves; while two series 309, 0.5-in., polyimid seal, Varian valves allow diffusion pumping of the gas manifold and isolation of the main chamber for venting. Finally, the chamber is vented by a 0.25-in. stainless steel Nupro bellows valve.

The chamber has two view ports manufactured by Huntington Laboratories and a number of alumina ceramic-metal, high voltage feed-thrus such as produced by Ceramaseal, Inc. The main view port is a 6-in. diameter, "zero-length", Pyrex window, while a 1-in. diameter, "zero-length" sapphire window permits the tip to be observed during loading and annealing or irradiated, if desired.

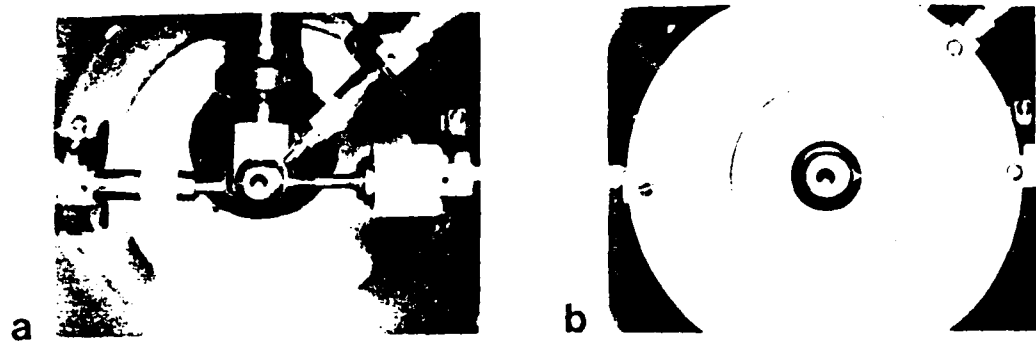
Chamber pressures from  $10^{-3}$  to  $10^{-10}$  Torr are measured to  $\pm 4\%$  by an Edwards, IG5M, ionization gauge with an Ion-7 control unit; while pressures from 0-2000 microns in the chamber, pumping lines, and gas manifold are measured by NRC, 531, thermocouple gauges with 801 control units.

The gas supply manifold is constructed of silver brazed copper tubing, and research grade, most impurities at 2 PPM, gases in glass bottles are connected to the manifold through a series of Nupro bellows valves. Since this assembly is attached by a flange to the system's stainless steel gas supply line, gases may be replaced or added with relatively little difficulty. The gases used were obtained from the Rare and Specialty Gases Department of the Air Reduction Company.

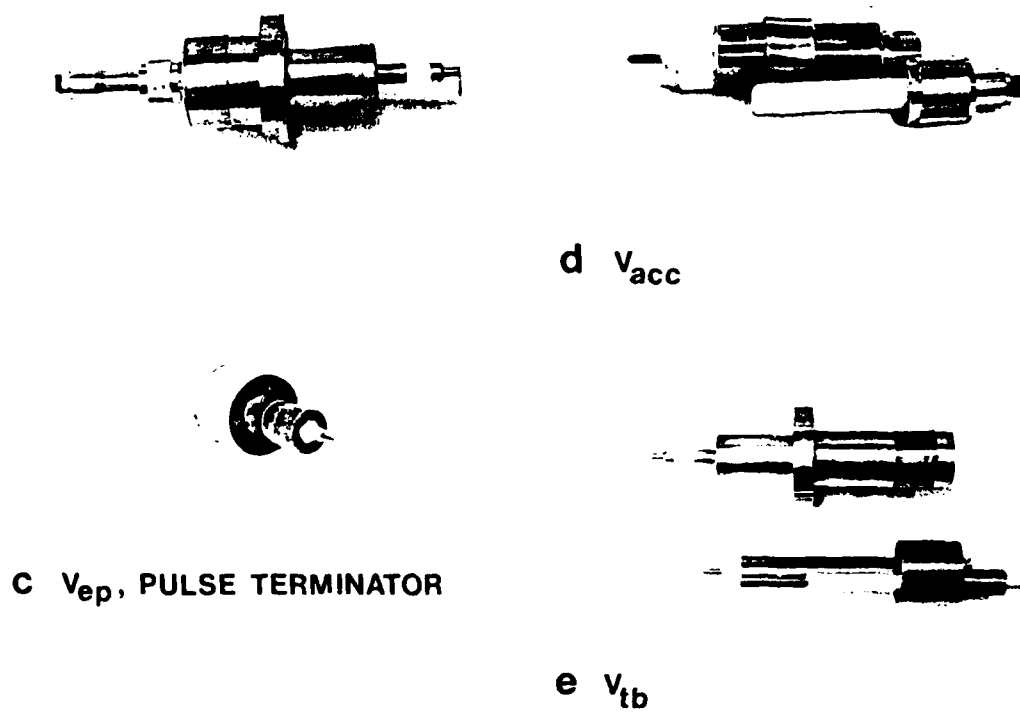
### 3. Tip Mount, Cold Finger, and Pulse Electronics

In the sample section of this instrument, the specimen tip is simultaneously electrically insulated from ground and cryogenically cooled. This permits the application of high voltage, both bias and pulse potentials, while maintaining cryogenic temperatures. In addition, the specimen tip may be annealed in situ and easily exchanged. This section of the imaging atom-probe together with its hemispherical counter electrode is shown in Figure 4(a). The addition of a ground plane, Figure 4(b), completes a fixed, vacuum pulse line to the specimen, while shielding the ion beams in the retardation, free flight, region from the bias and pulse lines in the sample section.

The tip is attached to the cryogenic cold finger dewar which enters the instrument directly from above, as shown in Figure 4(a). The tip



### RE-ENTRANT FEED - THRU



C  $v_{ep}$ , PULSE TERMINATOR

Figure 4. Photographs of tip section (a and b) and associated re-entrant feed-thrus (c-e).

is spot welded onto a 6.0-mil molybdenum loop whose ends are then inserted into two drilled, 0.125-in. diameter copper slugs. These are embedded in the cold finger's 0.775-in. diameter boron nitride insulator and held by screws. The loop's insertion is continued until the tip apex is 5-mm,  $\pm 0.25$  mm, distant from the face of the copper slugs; and, then, its stainless steel screws are tightened. The front of each slug and the loop may be seen through the aperture in the hemispherical counter electrode in Figure 4(a). To the rear of each slug is attached a Cu-Be strip, and these strips contact the thin stainless steel "feet" of both the pulse and tip-bias electrodes. Thus, the necessary cooling power and insulation from ground are provided by the boron nitride (thermal conductivity, 0.2 to 0.4 watts/cm<sup>2</sup>/°C/cm and resistance  $\sim 10^{14}$  ohms), while the stainless steel "feet" provide the required electrical contacts and minimize heat conduction to the tip. Finally, the bias and pulse external, electrical terminations can be easily removed; and the sample may then be annealed *in situ* by passing a current directly through the electrical feed-thrus.

With the added ground plane, the central conductors of the re-entrant feed-thrus for both the evaporation pulse, top in Figure 4(c), and the tip bias, top in Figure 4(e), form a fixed vacuum transmission line to the tip. The characteristic impedance,  $Z_v$ , and capacitance per inch,  $c'$ , of this line may be estimated by<sup>51</sup>

$$Z_v = 60 \ln \left( \frac{4h}{d} \right), \quad d \ll h \text{ and } c' = \frac{\tau}{Z_v} \quad , \quad (2.17)$$

where  $\tau$  is the 0.125 to 0.167 ns/in propagation delay,  $d$  is the diameter of the central conductor, and  $h$  is the distance between the central conductor and the ground plane. Roughly,  $h$  is 0.75 inches and  $d$  varies from 0.125 to 0.25 inches, which yields a  $Z_v$  of 150-190 ohms and a  $c'$  of 0.7-1 pf/inch. Since the line geometry is fixed within the 6-in. inner diameter chamber, the added ground plane yields a pulse line of roughly constant impedance with a capacitive load to ground of ~6 pf.

Since the vacuum pulse line is at the tip bias of  $V_{tb}$ , the 0.3-ns rise-time evaporation pulse must be capacitively coupled to the vacuum pulse line. This high voltage pulse of amplitude  $V_{ep}$  is developed across the resultant impedance of the 50-ohm-to-ground, coupling terminator, bottom in Figure 4(c), and the vacuum pulse line. This resultant impedance,  $Z_R$ , is the parallel combination of the 50-ohm terminator and the input impedance,  $Z'_v$ , of the vacuum pulse line.<sup>52</sup> As the vacuum line is short, it may be treated as a lump element whose impedance is approximately given by the line's nearly open end termination, ~20 megohm  $V_{tb}$  leak resistor, in parallel with its ~6 pf total capacitance,  $c'$ .<sup>52</sup> At the high frequencies of interest,  $Z'_v$  is essentially equal to its capacitive reactance,  $1/wc'$ . The load presented to the evaporation pulser by the instrument's tip section is then given by the resultant impedance:

$$Z_R \approx \frac{50\Omega(1/wc')}{[(50\Omega)^2 + (1/wc')^2]^{1/2}} \quad (2.18)$$

Since the ~6pf shunt capacitance is small, this load matches the 50-ohm internal impedance of this instrument's cable discharge

evaporation pulser over a wide range of frequencies. The frequencies to which equation (2.18) may be applied are given by

$$\omega\tau\ell \ll 1 , \quad (2.19)$$

where  $\omega$  is  $2\pi$  times the frequency,  $\ell$  is the length of the vacuum line, and, as before,  $\tau$  is the propagation delay per unit length of line. For example, setting equation (2.19) equal to 1 and substituting 0.125 ns/in for  $\tau$  and 6 inches for  $\ell$  yields ~200 MHz as the frequency limit for equation (2.18), at which  $Z_R$  has only declined to 47 ohms. Hence, much of the rise time and shape of the evaporation pulse may be retained.

The 50-ohm high voltage, 0-2.5 kV, pulse terminator must be able to conduct pulsed currents of 50 amperes,  $10^5$  watts, for the ~18 ns duration of the evaporation pulse. The terminator shown at the bottom in Figure 4(c) consists of a 500-pf high voltage coupling capacitor and a 100-watt, continuous, resultant 50-ohm-to-ground resistor. Since the coupling capacitor is in series with the shunt capacitance of the instrument's tip section, its value must be large compared to ~6 pf in order to maximize the pulse voltage at the tip. The resultant 50-ohm resistor is constructed of 20, 1000-ohm, non-inductive (Aryton-Perry winding) beryllium oxide core resistors in parallel and arranged symmetrically about a circular ground in two layers. The small "cord-wood-like" array of carbon resistors, shown as part of the terminator, may, in certain instances, be used to damp the pulse "overshoot". However, since their use reduces mass resolution they are nearly always replaced by a solid aluminum conductor.

Figure 4(e) shows the re-entrant feed-thru and internal terminator at the nearly open end of the vacuum pulse line. The short element is the 20-megohm tip bias leak resistor, while the long element is a 200-megohm potential divider for measuring the bias. A 390-ohm carbon resistor (not visible in Figure 4(e)) between the plug and the above resistors mildly damps the vacuum pulse line. The  $V_{acc}$  bias to the gold plated hemispherical counter electrode is the final potential required for the specimen section and is obtained through the terminator shown in Figure 4(d). A Murata, feed-thru, microwave capacitor (directly behind the plug in Figure 4(d)) with a capacitance - to - ground of 1000 pf prevents possible variations in the potential of the counter electrode from capacitive coupling during the evaporation pulse.

Since the pulse line is not terminated to 50-ohms directly at the tip, the leading edge of the pulse "overshoots". This high frequency behavior is desirable, since, by careful design, the "overshoot" may be shaped and used as an extremely short duration evaporation pulse. The re-entrant feed-thru design is the first shaping step because it yields the shortest vacuum line compatible with the mechanical constraints of this instrument. In this instrument, the length,  $l$ , is approximately

$$l \approx \frac{2t_r}{\tau} , \quad (2.20)$$

where  $t_r$  is the evaporation pulse rise time and  $\tau$  is given previously. This geometrically determines the minimum base width,

w, of the "overshoot", while the reflection coefficients at both ends of the line may act to increase the width.

The shaping may be clarified by considering a vacuum line with its open end directly at the tip, and with a length of

$$l \approx \frac{t_r}{\tau} . \quad (2.21)$$

The reflection coefficient at the open end of this line would be

$$\rho_t = 1 , \quad (2.22)$$

while the reflection coefficient at the input or 50-ohm terminator end is given as

$$\rho = \frac{R - Z_v}{R + Z_v} . \quad (2.23)$$

Here,  $Z_v$  is, as before, the characteristic impedance of the vacuum line, and R is the resultant of the 50-ohm terminator in parallel with the input impedance of the pulser. The contribution of the pulser may be ignored in a worse-case estimate. That is,

$$\rho_{\text{MIN}} \approx \frac{50\Omega - Z_v}{50\Omega + Z_v} . \quad (2.24)$$

If a value of 150 ohms is substituted for  $Z_v$  in equation (2.24), then the minimum reflection coefficient at the input end of the vacuum line is

$$\rho_{\text{MIN}} \approx -0.5 . \quad (2.25)$$

The actual negative coefficient may be somewhat larger, but the implication remains the same. The pulse is essentially confined

to "ring" within the 6-inch diameter of the chamber yielding an extremely short duration "overshoot" whose rise and fall times are  $\sim t_r$ .

By graphically considering several pulse reflections between the input and open end of the vacuum line,<sup>51</sup> the width and maximum amplitude,  $V_{MAX}$ , may be estimated. An input pulse with an amplitude  $V_{ep}$  and linear rise  $V_{ep}/t_r$ , no "overshoot", enters the vacuum line and is reflected in phase from the open end,  $\rho_t = 1$ . The incident and positive first reflection add at the tip to yield the pulse and "overshoot" leading edge, which rises in a time  $t_r$  to an amplitude of

$$V_{MAX} = 2V_{ep} \text{ as } l \geq \frac{t_r}{2\tau} . \quad (2.26)$$

The resultant pulse remains at this amplitude for a time  $t_r$  until the negative second reflection returns to the tip from the input end,  $\rho_{MIN} \approx -0.5$ . The instant this reflection reaches the tip, it is reflected back in phase yielding a negative third reflection. Adding the incident and first, second, and third reflections at the tip yields the trailing edge of the "overshoot" which falls in a time  $t_r$  to an amplitude of  $V_{ep}$ . The base width of the "overshoot" is then

$$W = 2.5 t_r . \quad (2.27)$$

For various lengths of vacuum line terminated in this manner, the base width and maximum "overshoot" amplitude may be given as

$$\left[ \begin{array}{l} 0 < W < nt_r \\ V_{ep} < V_{MAX} < 2V_{ep} \end{array} \right] \quad \text{for } l < \frac{t_r}{2\tau} \quad (2.28)$$

and

$$\left[ \begin{array}{l} (2\tau l - t_r) < w \leq (2\tau l - t_r) + nt_r \\ v_{ep} < v_{MAX} \leq 2v_{ep} \end{array} \right] \text{ for } l \geq \frac{t_r}{2\tau} . \quad (2.29)$$

Here,  $n$  is a positive number which depends on both reflection coefficients, and its value would be 1.5 for the above example, in equation (2.27). Equations (2.28) and (2.29) clearly show that the "overshoot" width may be minimized by reducing both the geometric length of the vacuum line and the pulse rise time provided that appropriate reflection coefficients are established.

Because of physical constraints, the open end of this instrument's vacuum line is not directly at the tip. Actually, the tip is at the center of a  $\sim 2t_r/\tau$  length of vacuum line with an input and open end termination equivalent to that of the previous analysis. If analyzed as above, the "overshoot" at the tip will still retain an amplitude of  $2v_{ep}$  for a time,  $t_r$ , but it will be delayed a time,  $t_r$ , yielding a shoulder on the pulse leading edge. In addition, its rise,  $t_r$ , and fall,  $t_r$  to  $1.5v_{ep}$  or  $3t_r$  to  $v_{ep}$ , will be slower. In practice, the predicted slower rise and fall times are probably reduced by both a slight "overshoot" on the smooth, incoming pulse and a larger input reflection coefficient, equation (2.23). This probably yields a peaked pulse "overshoot" comparable to that obtained previously. That is:

$$v_{MAX} \leq 2v_{ep} , \quad w \sim 2t_r . \quad (2.30)$$

Finally, it is necessary to produce the subnanosecond rise-time evaporation pulse and, thereby, the brief "overshoot" both of which are needed for high mass resolution identification of field evaporated species. Here, as in nearly all atom-probe designs, this is accomplished by a high voltage, 0-2.5 kV, discharge line pulser. The one used in this instrument is the author's modified version of a Huggins Laboratory design, Model 961E,<sup>53</sup> and detailed diagrams and information on its construction are provided in the Appendix.

A coaxial cable is charged through a high impedance leakage resistor to a voltage of 0-2.5 kV. This cable is then discharged by shorting it, momentarily through a switch, with an output cable of the same impedance properly terminated at the far end. The amplitude of the output voltage across the far termination is approximately half the voltage on the charging line. The output pulse width is simply twice the propagation delay of the charging line,

$$\text{p.w. (ns)} = 2T\ell_c \quad , \quad (2.31)$$

where  $T$  is the delay (ns) per unit length, and  $\ell_c$  is the length of the charging line. Typically,  $T$  is 1.54 ns/ft. for 50-ohm coaxial cable, and a coiled charging line (RG-54A low attenuation cable) 6 feet in length is needed for an 18.4-ns evaporation pulse. This pulse should be long enough for the heaviest ion to traverse the acceleration zone near the tip.

The rise-time and amplitude of the output pulse are dependent on the switch which is a magnetically activated mercury-wetted reed

encapsulated in glass at 10 atm of hydrogen. Both the electrodes and capsule are axially symmetric and intended for 50-ohm impedance applications. A 0.3 to 0.5 ns pulse rise-time is characteristic of the closure arc build-up time, and a reduction in the ideal output voltage,

$$v_{ep} \approx \frac{v_{charging}}{2} , \quad (2.32)$$

of 10% is not uncommon for that due to the arc, or internal resistance, of such a switch. In fact, this system's pulser exhibits an 11% reduction in output amplitude. This reduction was directly measured at low voltage, and established relatively at high voltage by the conformity between an observed and an analytically predicted output pulse shape. The analytic treatment<sup>52</sup> of the discharge line pulse and a comparison of the observed and predicted pulse amplitudes is presented in the Appendix. There, the pulser is treated as discrete and distributed, cables, circuit elements by the method of Laplace Transforms.<sup>52,54</sup>

The expression for the evaporation pulse voltage is obtained from equation (A.15) and may be written as

$$v_{ep}(t) = \begin{cases} \left(1 - \frac{\beta}{2}\right) \frac{v_{charging}}{2} & 0 < t < 2T\ell_c \\ \frac{\beta}{4} \frac{v_{charging}}{2} & 2T\ell_c < t < 4T\ell_c \\ 0 & t > 4T\ell_c \end{cases} , \quad (2.33)$$

where  $\beta$  is such that  $\beta Z_0$  is the internal resistance of the mercury switch with  $Z_0$  being the 50-ohm characteristic impedance of the discharge cable. For this instrument, the  $\beta$  of 0.22 yields a switch

resistance of 11 ohms and evaporation pulse voltage of

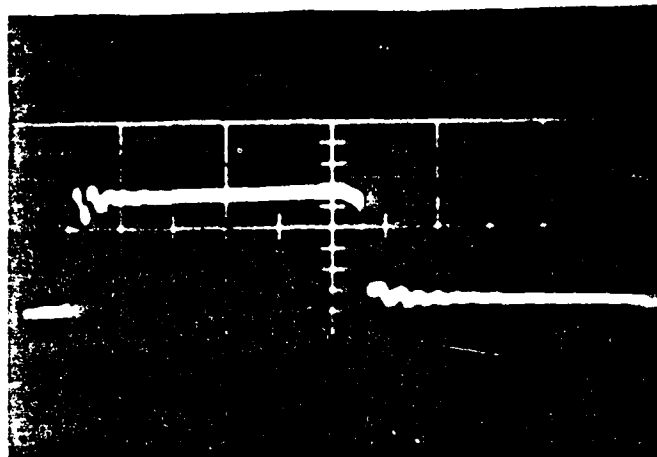
$$V_{ep} = 0.89 \left[ \frac{V_{charging}}{2} \right], \quad 0 < t < 2T\ell_c \quad . \quad (2.34)$$

The value obtained from equation (2.34) is entered for  $V_{ep}$  in the flight equations for this mass spectrometer.

The pulser's output, properly terminated into 50-ohms is shown at a band width of 1 GHz in Figure 5(a) and at 350 MHz in Figure 6(a). A drawing of the pulse in Figure 6(a) is included in Figure 34(b) of the Appendix for comparison with that predicted by equation (A.15) or (2.33). The evaporation pulse as measured at the tip loop is shown in Figure 5(b) with the observed shape being limited by both the 3 pF shunt capacitance of a Field Effect Transistor, FET, (Tek. P6201) probe and the 350 MHz band width of the Tek. 485 oscilloscope.

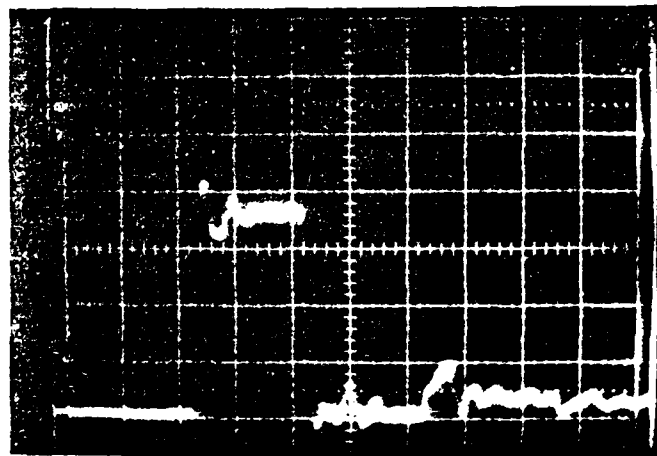
#### 4. Timing and Oscilloscopic Electronics

This instrument's timing sequence is initiated by the evaporation pulse, and the zero of time is the instant that the evaporation pulse, Figure 6(a), and the initial trigger, Figure 6(b), simultaneously leave the evaporation pulser. From this point on, the flow of both timing triggers and mass signals (gated image and oscilloscopically observed voltage pulses) is indicated in Figure 1. The mass signal path is paralleled by two associated electronic pathways whose trigger pulses either activate, gate, the Chevron detector for gated-image mass discrimination, or initiate and appear on a time-of-flight oscilloscopic trace of incoming mass signals. The initial or delayed



a. EVAP. PULSE (TEK.519, BW-1GHz)

RISE TIME < .5ns  
PULSE WIDTH 13.7ns  
HOR. 5ns/cm  
VERT. 9.3 v/cm



b. EVAP. PULSE AT TIP  
(TEK.485, BW-350 MHz)

PULSE WIDTH 18.4ns  
HOR. 10ns/cm  
VERT. 1v/cm

Figure 5. Oscilloscopic traces of the evaporation pulse: (a) measured at a 50 ohm termination and (b) measured at the tip.

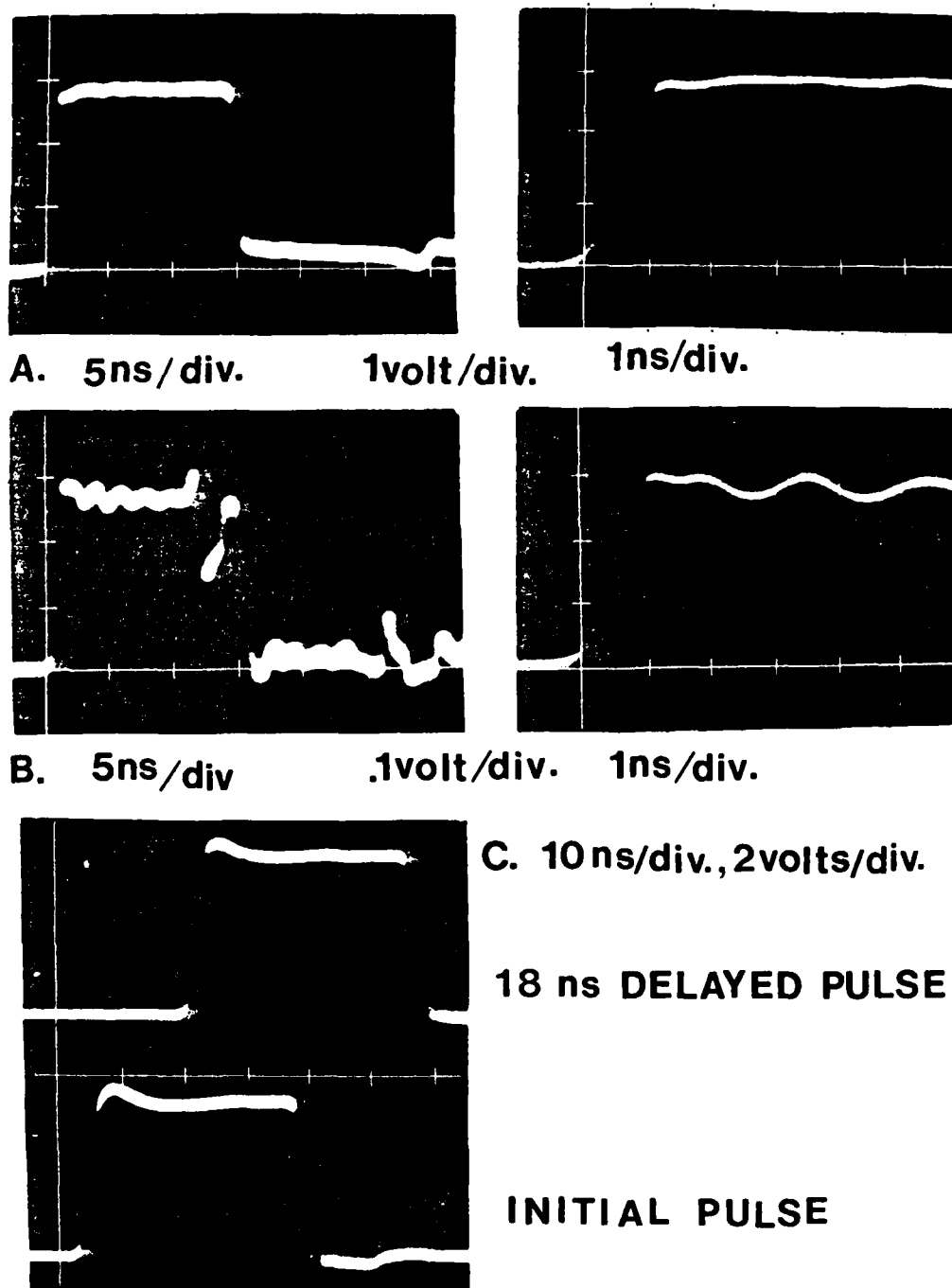


Figure 6. Oscilloscopic traces of the timing sequence pulses (Tek. 485 scope, BW-350 MHz): (a) evaporation pulse into 50 ohms, (b) initial trigger from the evaporation pulser, and (c) initial and delayed output triggers from the variable time-delay.

trigger pulse, shown in Figure 6(c), in each electronic pathway originates from a variable time delay, which is activated by the original trigger from the evaporation pulser.

Instruments within the timing sequence, whether low or high voltage output, and the flight chamber are interconnected by properly terminated 50-ohm coaxial cables (e.g., RG-58A or RG-8). The associated cable and instrument delay times have been accurately measured and are listed in the Appendix. The resulting net instrumental delay, 119.7 ns, is sufficiently short to permit the detection of the lightest species,  $H^+$ .

The original trigger is acquired by proximity, capacitive coupling of a portion, 0.4%, of the main evaporation pulse to a D.C. to 500 MHz FET in a source follower circuit. The output of this "pick-off" circuit develops a 0.2 to 2 volt, 18-ns wide trigger pulse at the threshold input of the time-delay. Any timing error due to the increase in trigger amplitude with evaporation voltage is held to a tenth of a nanosecond by setting the delay's threshold to 0.2 volts on the trigger's 1-ns rise-time leading edge. The details of this "pick-off" circuit and its location within the pulser are given in the Appendix.

Once triggered, the Berkeley Nucleonics Model 7067 digital time-delay generator provides an accurate time reference and synchronizes gated-image mass discrimination with time-of-flight mass identification. The absolute accuracy of the unit is ~0.1-0.5 ns, while the electronic jitter between input trigger and delayed output is ~0.1 ns. There are two output pairs, one initial and the other delayed, each having simultaneous +5 and -2.5 volt outputs.

The time-delay's initial positive output triggers the full sweep, time base A, of a dual channel Tektronics 485 oscilloscope, while the negative delayed output is displayed as a positioned fiducial mark via channel one. Also, the negative delayed output simultaneously triggers and appears on the trace of the expanded sweep, delayed time base B. This references and triggers both the full and expanded mass sweeps. During these sweeps, the output voltage pulses of the detector, mass signals, are fed through an FET probe (Tek. P6201) into channel two. Channels one and two are algebraically added yielding either the full or expanded time-of-flight mass spectra. In addition, a stepped DC potential is applied to channel one to permit up to 30 traces to be recorded per oscilloscope. The accuracy to which the oscilloscopes may be read is dependent upon the particular rate of sweep; e.g.,  $\pm 1$  ns at 20 ns/cm.

Since the remaining positive delayed output is coincident with the fiducial mark, it may be used to synchronously gate the detector to a preselected species' arrival time. Thus, a gated image is obtained of a single, identified species, accurate to within the 8-ns gate interval, by setting the time-delay so that the fiducial mark is positioned 30 ns prior to the selected mass signal.

##### 5. Gate-Pulse and the Ion Detector

Since the gain of the Chevron CEMA detector is a rapid function of the potential difference, zero to several kilowatt, applied between its input and output surfaces, the detector may be gated,

activated for a brief period rather than continuously, by the application of a high voltage pulse. In addition, the detector may be gated about a time preselected with the time-delay by using a pulser whose jitter between input trigger and output high voltage pulse is minimal, ~1 ns. This instrument's gate pulser is a Lasermetrics Model 8601, which uses a Krytron switch tube<sup>55</sup> in a Blumlein configuration. This pulser generates a negative 2-7 kV, 8-ns wide pulse across a proper 50-ohm termination. The output pulse shape is shown on the right in Figure 7(a), while the high power termination is shown in Figure 8(a). This negative pulse is applied about a preselected time to the input plate, that facing the tip, of the detector.

The jitter (~1 ns) and throughput delay (57 ns) were measured by simultaneously triggering the gate pulser and the Tek. 485 oscilloscope with the dual delayed outputs of the time-delay. This is nearly the same configuration (except for an additional 2-ns cable delay) of delay and pulser used in the instrument. Both the trigger and the high voltage output pulse (proximity coupled to an FET probe) are displayed on the dual channel oscilloscope. Ten superimposed traces, where the delay between the trailing edge of the trigger and the leading edge of the high voltage pulse is 36 ns, are shown on the left side of Figure 7(a).

The single ion detector utilized in this instrument is a 75-mm diameter, flat, Galileo Electro-Optics Corporation's Chevron CEMA.<sup>36</sup> This detector is shown in Figure 8(b), upper left, combined with the

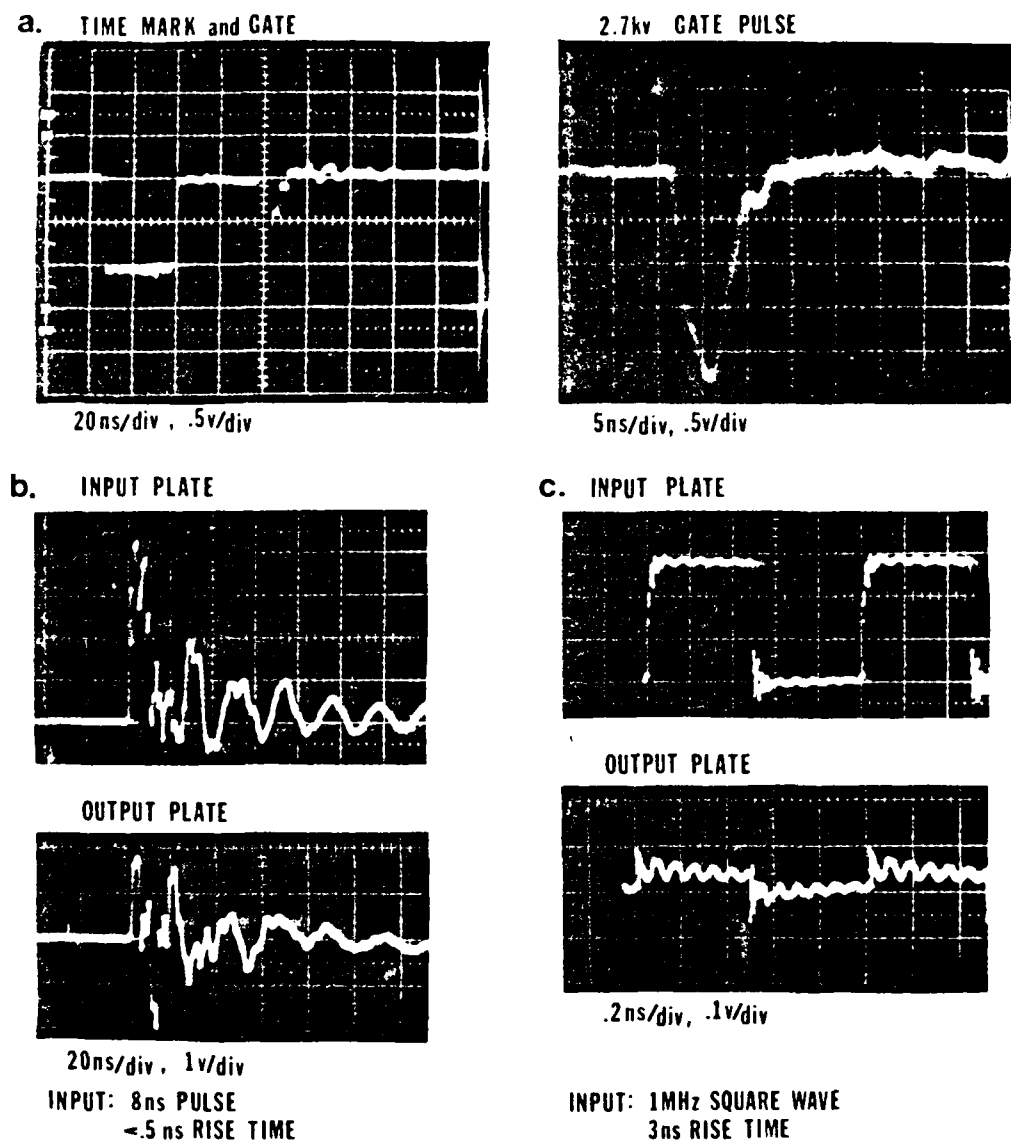


Figure 7. Oscilloscopic traces showing: (a) the jitter and delay between the time-mark and gate pulse, 10 traces; and the gating potential difference across the Chevron CEMA for (b) an 8 ns pulse and (c) a 1 MHz square wave.

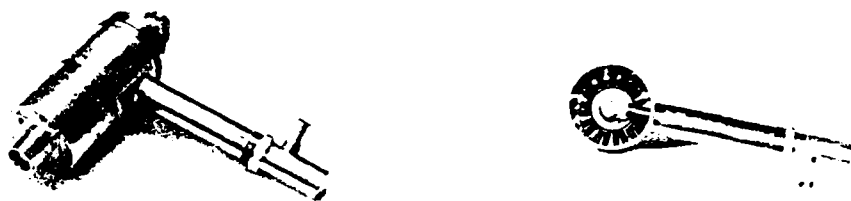
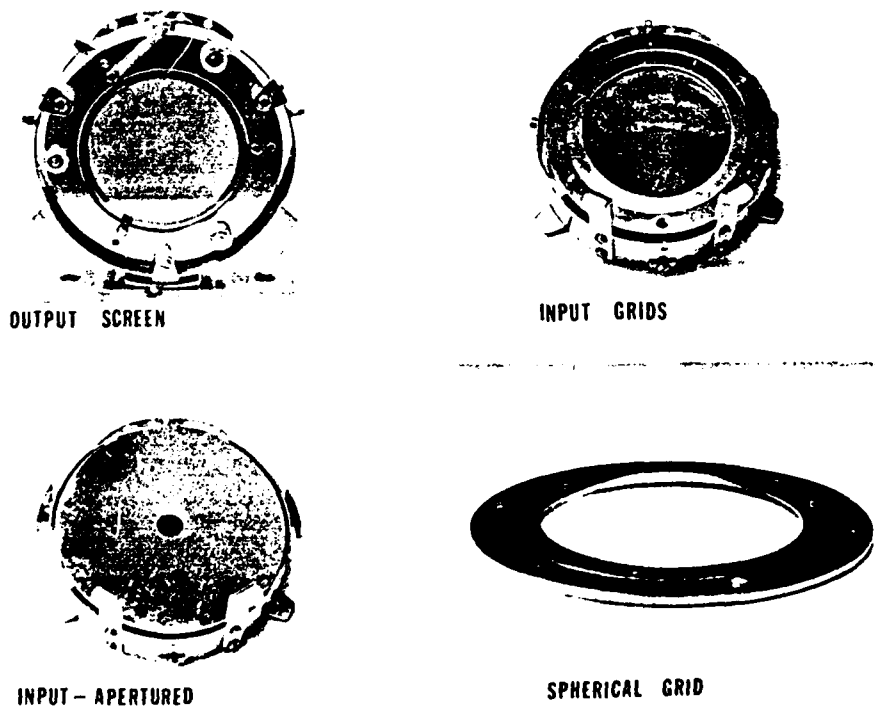
**a. GATE PULSE TERMINATOR****b. DETECTOR ASSEMBLY**

Figure 8. Photographs of the gate pulse terminator (a) and the Chevron CEMA detector assembly (b).

phosphor screen onto which its output is proximity focused for imaging. The application of single or dual, Chevron, Channeltron Electron Multiplier Arrays to field-ion,<sup>56,57</sup> field-desorption<sup>5</sup> microscopy, and atom-probe analysis has been discussed in detail by several authors.<sup>1,27,29</sup>

Both channel-plate multipliers in a Chevron consist of a two-dimensional array of glass capillaries, each a continuous strip electron multiplier. The dual, tandem plate assembly is ~5 mm thick with a 53- $\mu\text{m}$  center-to-center spacing between each 45- $\mu\text{m}$  diameter channel. This represents an open area ratio of ~60%, nominal detection efficiency. Actually, the detection efficiency for positive ions may depend on energy,<sup>58</sup> mass,<sup>29</sup> and biasing conditions.<sup>59</sup> In this instrument, the negative bias and the negative gate pulse on the input plate repel spatially uncorrelated secondary electrons created by interchannel ionic impacts, while post-accelerating the incoming positive ions to a minimum energy of ~8 kV. This yields a probable detector efficiency of 60%, while insuring spatial correlation. Resolution for the Chevron used is specified by the manufacturer as 5 line pairs/mm or a minimum spatial separation at the screen of ~0.2 mm. This, if projected back 13.8 cm onto a 1000 Å radius tip, will yield an object resolution of 2 Å.<sup>29</sup> For field-ion images, this spatial resolution is sufficient; however, it ultimately limits field-desorption images.

This efficiency and resolution are sufficient for practical, spatially resolved, single ion detection; however, for single ion mass discrimination, it is necessary to avoid the detector's inherent

dark count, 1.4 counts/s/cm<sup>2</sup> at full gain. The instrument's detection systems essentially eliminated the noise problem by only briefly activating either the oscilloscope or the detector about a time correlated to the original evaporation event, time-gating. This permits both single ion mass identification by time-of-flight mass spectroscopy and spatially resolved single species desorption imaging.

There are two remaining detector characteristics to consider, one of which principally effects the time-of-flight mass identification, detector afterpulsing; the other is the detector's large capacity, ~120 pf. The Chevron detector's afterpulsing is minimal and dependent on background pressure. At a background pressure of  $3 \times 10^{-9}$  Torr, a 1% afterpulse was noted. This is somewhat higher than the previously reported value of less than 0.25%.<sup>60</sup> However, since the afterpulse occurs at a specific interval after a mass signal, it may be identified and, therefore, is not a significant problem.

The maximum gated image mass resolution results from a minimum gate interval. However, the gate interval resists reduction because of the large shunt capacitance of the detector.<sup>1,61,62</sup> The detector's capacitance heavily loads the 50-ohm Krytron gate-pulser by shunting the high power 50-ohm terminator. The resultant load impedance at 200 MHz may be calculated from equation (2.18) by substituting a typical value of 120 pf. This yields a resultant impedance of 6.6 ohms which results in a reflection coefficient of -0.8. This high frequency impedance mismatch has been partially corrected by pulsing the dual detector plates in series, thereby reducing their capacitance.<sup>37</sup>

The reduced capacitance, 60 pf., yields a 200 MHz terminal impedance of 13 ohms with an associated reflection coefficient of -0.6. The actual potential difference across the detector during gating may be inferred from the detector's response, shown in Figure 7(b) and (c), to the two low voltage gating signals which effectively bracket the expected frequency behavior of the high voltage gate. Because of the detector's rapid increase in gain with voltage, only the initial high voltage gate pulse, and not the subsequent rings expected from the trace in Figure 7(b), would significantly activate the detector. Hence, a gate width of 8 ns may be obtained and, in fact, may be demonstrated by gating for  $H^+$ . As the spread in hydrogen's arrival time is less than 1 ns, it may be used to profile the actual gate by varying the gate position about its arrival time. This only yields observed image dots when the gate position is within 8 ns of the actual arrival time. Typically, during gating, the Chevron is activated by superimposing a 3 kV gate pulse onto a DC bias of 1 kV.

The impedance mismatch may be fully overcome in the future by using a pulser designed to drive 5 ohms. In fact, such a high voltage pulser can be built by incorporating a Krytron switch tube into an already existing design.<sup>63</sup>

#### 6. Angular Correction

The ions which originate at the tip follow nearly radial trajectories in their flight to the detector, but the Chevron detector is flat rather than hemispherically curved. This results in off-axis

flight paths,  $P_f$ , which are somewhat longer than the axial path,  $P_o$ . If this were not compensated for, an ion's flight time would depend on its initial projection angle,  $\theta$ .<sup>1</sup> In the case of free-flight, the on-axis,  $t_o$ , and off-axis,  $t_f$ , flight times for a single species can be given as

$$t_o \propto \frac{P_o}{\sqrt{V}} \quad \text{and} \quad t_f \propto \frac{P_f}{\sqrt{V}} \quad , \quad (2.35)$$

where  $V$  is the initial accelerating potential and  $P_f$  is

$$P_f = P_o \sec \theta \quad . \quad (2.36)$$

This yields a fractional error in the flight time which may be written as

$$\frac{t_f - t_o}{t_o} = \left[ \sec \theta - 1 \right] \quad . \quad (2.37)$$

At a distance of 13.8 cm from the tip, the 7.5-cm flat, Chevron detector presents a full acceptance angle of  $\sim 30^\circ$  or a maximum projection angle of  $15^\circ$ . If this value of  $\theta$  is substituted into equation (2.37), it yields 3.5% error between off- and on-axis flight times. Such an error could severely limit full acceptance angle mass resolution, and successful gated images with an 8-ns gate width would be impossible for all but the lightest species,  $H^+$ . For example, a 3.5% error in a typical 150-ns flight time for hydrogen would yield a 5-ns spread in the arriving ions.

The ion's angular dependent flight path in this instrument is compensated for in two stages. During their flight, ions are first retarded and then briefly post-accelerated. Ignoring the retardation

for the present, the compensation scheme may be analyzed, in principle, with the free-flight arrangement in Figure 9. Here, it is assumed that the ions are instantaneously accelerated at the tip, and then travel with a velocity of  $v_1$  toward the detector. This velocity is proportional to the square root of the accelerating potential,  $V_1$ :

$$v_1 \propto \sqrt{V_1} . \quad (2.38)$$

Prior to encountering the detector they are instantaneously post-accelerated at the 6-cm radius corrector, which could be nearly done by a set of closely spaced ( $\sim 2$  mm) concentric grids held at a potential difference  $V_2$ . This yields a final velocity,  $v_2$ , which is proportional to the square root of the sum of the potentials. That is:

$$v_2 \propto \sqrt{V_1 + V_2} . \quad (2.39)$$

Consequently,  $\epsilon$  in Figure 9 is given as

$$\epsilon = \frac{1}{\sqrt{1 + \alpha}} , \quad (2.40)$$

where  $\alpha$  is the ratio of  $V_2$  to  $V_1$ . From this point on, the geometry dictates the on- and off-axis flight times and the ideal curve required for the corrector. The remaining pertinent equations are shown in Figure 9, where the ideal curve is given as

$$P = \left[ \frac{P_0}{1 - \epsilon} \right] \left( 1 - \epsilon \sec \theta \right) . \quad (2.41)$$

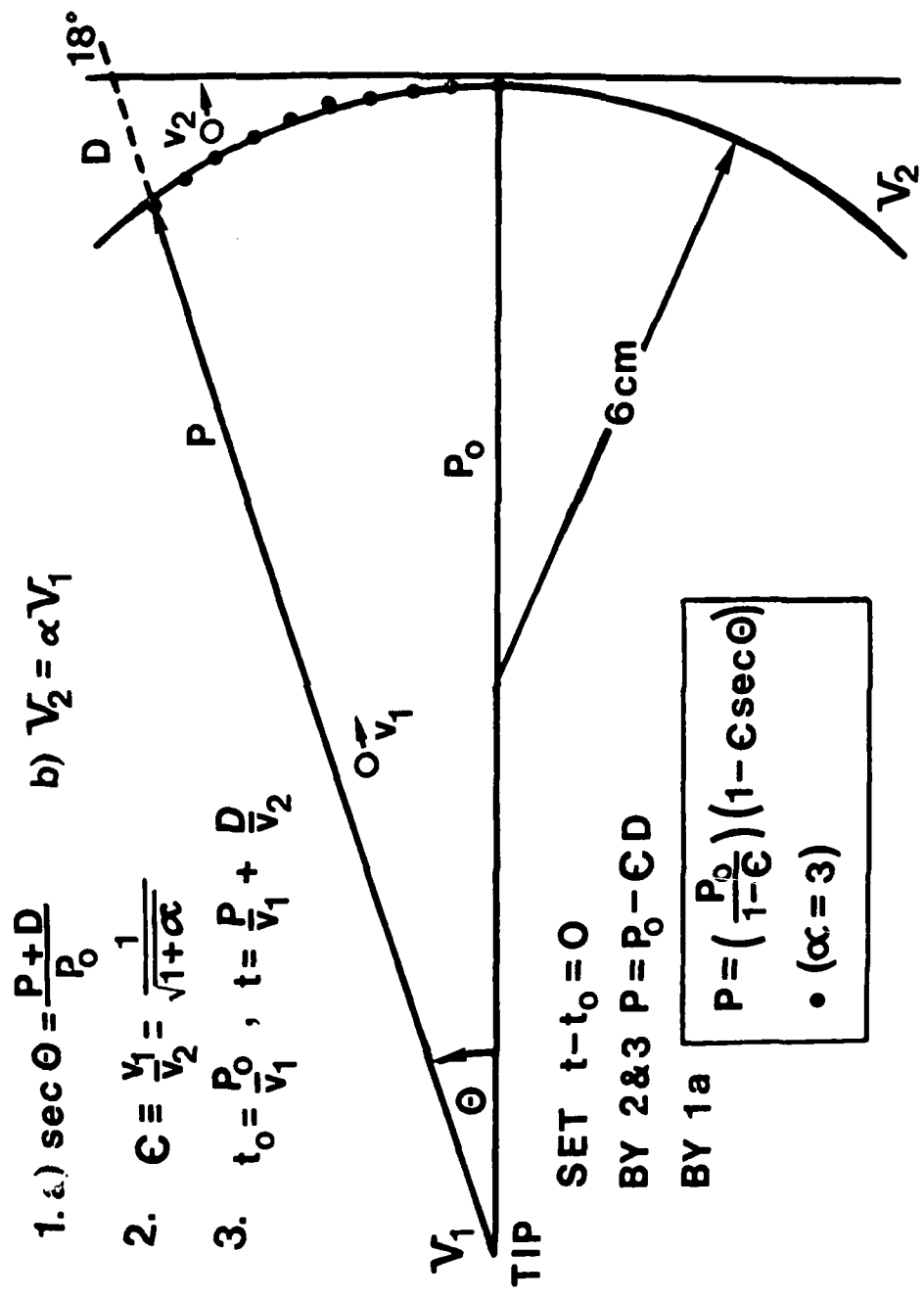


Figure 9. A tip-to-detector geometry using a spherical grid to induce on and off-axis ions to arrive nearly simultaneously at a flat detector.

Here,  $P_o$  and  $P$  are the on- and off-axis flight paths, respectively, and  $\theta$  and  $\epsilon$  are as given previously. For a  $P_o$  of 12 cm and an  $\alpha$  equal to 3, equation (2.41) gives a curve which closely approximates the 6-cm radius corrector for  $\theta$  less than  $18^\circ$ .

More detailed calculations with a double grid corrector indicate that  $\alpha$  may be somewhat larger due to a slight outward refraction of an ion's trajectory at the corrector. In any case,  $\alpha$  is prohibitively large; e.g., a tip potential of 5 kV would require a corrector potential difference of at least 15 kV. For this reason, a retardation scheme is employed which retards off-axis ions less than on-axis ions. This "folds" a front of evaporated ions forward prior to encountering a corrector, which reduces the required post-accelerating potential. The retarding field is obtained by applying a negative potential to the 1.6-cm diameter counter electrode in front of the tip. The effect of this field can be seen in the image compression which results when excessive retardation is applied as is shown in Figure 10. In practice, no more than 70% retardation is employed in order to avoid this distortion of the ion optics.

In this instrument, a single spherical corrector grid, shown in the lower right of Figure 8(b), is used in combination with a flat grid which terminates the retardation region. The transparency of the combined, grounded, stainless steel grids is 64% at normal incidence. These are shown at the input of the detector in the upper right of Figure 8(b). The proper retardation settings are achieved by adjusting the retardation potential until a single species' gated image fills the screen.

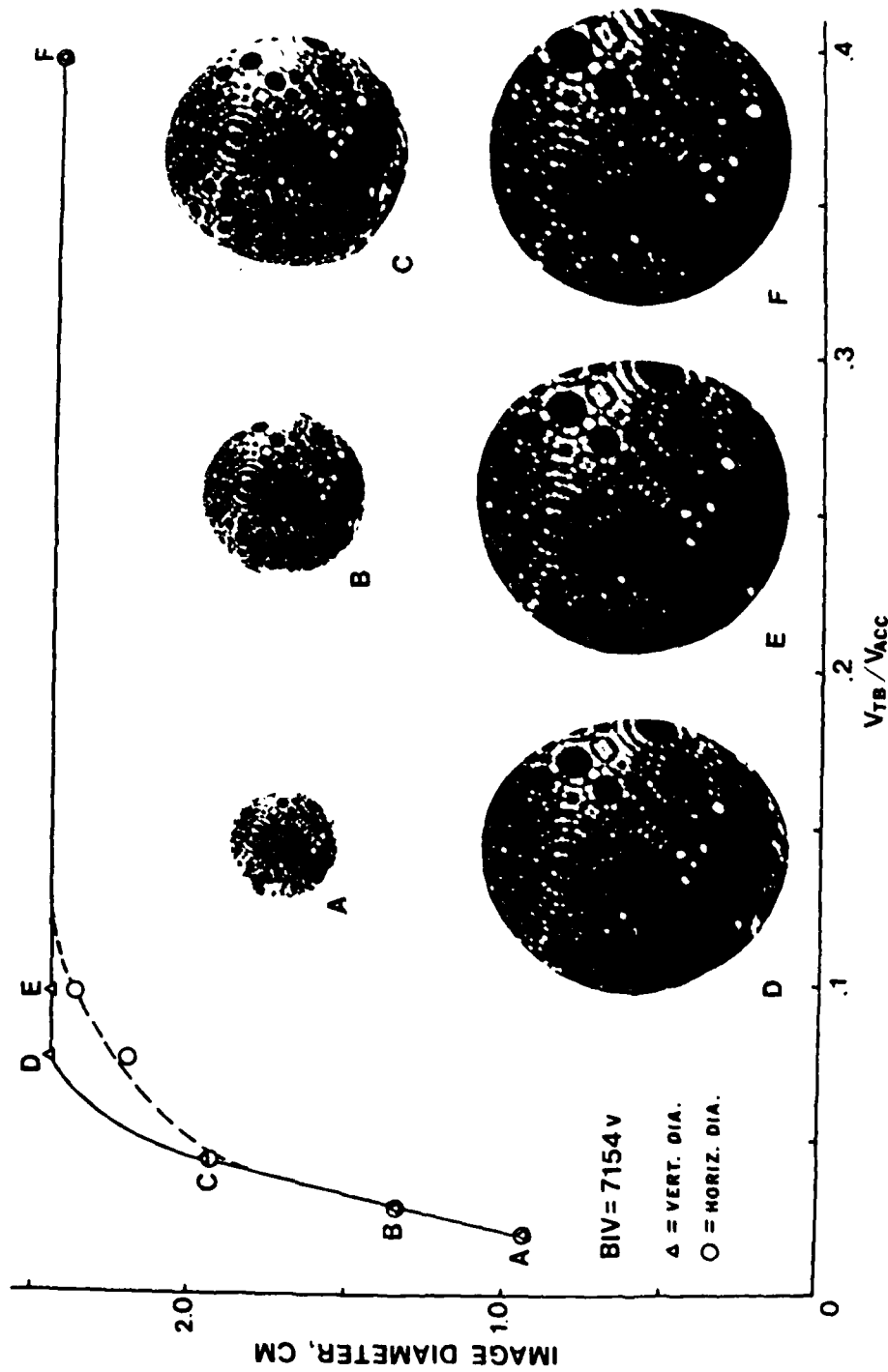


Figure 10. A graphic and photographic display of field-ion image compression at large retarding potentials.

In addition, the instrument may be apertured to an acceptance angle of  $5.4^{\circ}$  by a half-inch, on-axis opening in the aluminum plate shown in the lower left of Figure 8(b). The high resolution data obtained from the apertured configuration may be consistently obtained by incorporating an integral, effective aperture. This aperture may be made simply by providing a phosphor screen with a separate on-axis collector.

Finally, since this instrument is capable of separating the isotopes of tungsten in free-flight, this entire, elaborate, angular correction would have been unnecessary had a hemispherically curved, 5-in diameter Chevron been available.

#### 7. Potential Measurements and Power Supplies

The high voltage DC bias to the tip is provided by a precision 0-30 kV power supply (CPS Model 100P). The remaining high voltage DC bias potentials are provided by precision 0-20 kV power supplies (CPS Model 500L-P or N). All these supplies are regulated to better than 0.01%, and they are stable to within 0.02% per 8-hour period. Their ripple components are less than 2 volts and are further filtered to be ripple free to 0.1 PPM, 2 mV out of 20 kV. The details of the filtering arrangement are presented in the Appendix.

The applied potentials are measured by Victoreen, MOX-5RD, metal oxide glaze on alumina potential dividers, which have been calibrated against a precision standard CPS high voltage divider probe. Their calibration curves are given in the Appendix. All dividers, except

that on the screen side of the Chevron, are read by a high input impedance,  $10^9$  ohm,  $4\frac{3}{4}$  digit Newport (Model 2000 AS-2) digital voltmeter, with a maximum error per 8-hour period of 0.005% of reading  $\pm$  0.005% of full scale. The remaining Chevron to screen potential is read by a less precise  $3\frac{3}{4}$  digit Newport (Model 400A-3) digital voltmeter.

#### 8. Imaging and Photography

Field-ion, desorption, and gated-desorption images are observed on the output phosphor screen and photographed through the instrument's main 6-in. diameter view port. The phosphor is applied by sedimentation with a water glass binder onto a glass plate which has been conductively coated on both sides with transparent tin oxide. For the purpose of proximity focusing, a gap of ~1.5 mm is maintained with ceramic washers between the Chevron output plate and the phosphor screen.

The field-ion images are photographed on ASA 400 Tri-X film with a conventional 35-mm single lens reflex camera using an f:1.4 lens. Similarly, field-desorption images are photographed with either Tri-X or ASA 1000 2475 recording film.

A similar camera with an f:1.2 lens is used to photograph the oscilloscopic traces using 2475 recording film "push" processed to an ASA of ~3000. The oscilloscope camera attachment, as with others, provides for simultaneous viewing and photography.

### III. PERFORMANCE AND CALIBRATION

During free-flight, equation (2.8) would correctly identify an unknown mass-to-charge species except for the small error incurred by neglecting the final post-acceleration. That is, provided both the pulse factor and instrumentation delay are known. In what follows, a more exact flight equation is calculated which permits species identification during either free or retarded flight. Also, the pulse factor is presented in relation to the expected time resolution of the instrument, and both the pulse factor and the instrumentation delay are determined.

After calibration, time-of-flight mass spectra and specimen micrographs are presented which depict the instruments experimental performance. The time-of-flight mass spectra show a resolution,  $m/\Delta m$  (20%), of 150 with the system apertured, and a resolution  $\sim 50$  at full acceptance angle. Both here and in Chapter IV, the gated-desorption micrographs have a time resolution,  $t/\Delta t$ , of 100 for a species flight-time of 1000 ns.

#### 1. Flight Equations

The on-axis travel time for each section of an ion's flight path through the instrument may be calculated and the resultant flight-time may then be used to determine the ion's mass-to-charge ratio.

Between the tip apex and the hemispherical counter electrode, the spatial potential and on-axis travel time may be calculated by assuming either a best, concentric spheres,<sup>64,65</sup> or worse case, confocal paraboloids,<sup>65,66</sup> geometry. For concentric spheres, the travel time is

essentially that due to an instantaneous acceleration and subsequent free-flight, since the  $\sim 1000 \text{ \AA}$  apex radius is extremely small in comparison with the 0.008 m radius,  $R_a$ , of the counter electrode. However, the travel time for a confocal paraboloid geometry would be  $\sim 5\%$ <sup>66</sup> longer than the free-flight estimate. This worse case would yield only a 0.3% increase in the total flight time, since the travel time in the acceleration region of this instrument is at most  $\sim 6\%$  of the total. This is well below the 3% uncertainty in absolute species identification predicted by equation (2.9), and, therefore, a free-flight estimate as in equations (2.3) and (2.4) may be used to obtain the travel time in the acceleration section,  $t_1$ . That is:

$$t_1 = \left( \frac{m}{2qV_T} \right)^{1/2} R_a \text{ for } q = ne \quad . \quad (3.1)$$

Here, the distance, tip apex to counter electrode, is essentially the above radius of the counter electrode; and  $V_T$ , the total potential difference between the tip and counter electrode, is

$$V_T = V_{DC} + \alpha V_{ep} \quad (3.2)$$

as in equation (2.3).

The travel time in the retardation or free-flight zone,  $t_2$ , may be estimated by using the spatial potential,  $V(r)$ , between two concentric spheres.<sup>65</sup> This second region is bounded by the counter electrode at a negative potential,  $V_a$ , and the flat grid (or aperture plate) at ground or zero potential. The flight path in this region, 0.114 m, is

given as  $R_g - R_a$ , where  $R_g$  is the on-axis tip to grid distance and  $R_a$  is as given previously. Laplace's equation for the potential within this region may be given in spherical co-ordinates as

$$\frac{d^2V}{dr^2} + \frac{2}{r} \frac{dV}{dr} = 0 \quad , \quad (3.3)$$

where  $r$  is measured from the center of curvature of the tip apex. This yields the potential

$$V(r) = c_1 + \frac{c_2}{r} \quad , \quad (3.4)$$

where the constants  $c_1$  and  $c_2$  are given by the boundary conditions

$$V_a = c_1 + \frac{c_2}{R_a} \quad \text{and} \quad 0 = c_1 + \frac{c_2}{R_g} \quad . \quad (3.5)$$

The spatial potential within the region may then be written as

$$V(r) = K \left[ \frac{1}{R_a} - \frac{1}{r} \right] - |V_a| \quad \text{for} \quad K = - \frac{|V_a|}{\left[ \frac{1}{R_a} - \frac{1}{R_g} \right]} \quad , \quad (3.6)$$

where  $K = -c_2$ .

The energy of an ion within the region must equal its initial energy as it enters through the aperture in the counter electrode. That is:

$$\frac{1}{2} mv^2 + qV(r) = qV_T + qV_a \quad , \quad (3.7)$$

where  $qV_T$  and  $qV_a$  are the ion's initial kinetic and potential energy, respectively. Here,  $V_T$  may be written as

$$V_T = V_t + |V_a| \quad (3.8)$$

by substituting equation (2.1) for  $V_{DC}$  in equation (3.2) and letting  $V_t$  be the total potential applied to the tip,

$$V_t = V_{tb} + \alpha V_{ep} \quad . \quad (3.9)$$

If equation (3.8) is substituted for  $V_T$  in equation (3.7) and the result rearranged, one obtains

$$\frac{1}{2} mv^2 = q \left[ V_t - V(r) \right] \quad , \quad (3.10)$$

as  $V_a = - |V_a|$ . If the spatial potential given by equation (3.6) is substituted for  $V(r)$  in equation (3.10) and the resulting expression solved for the velocity, one obtains

$$\frac{dr}{dt} = \left( \frac{2q|V_a|}{m} \right)^{1/2} \left( \frac{R_a}{R_g - R_a} \right)^{1/2} \left( \frac{R_g}{r} + A \right)^{1/2} \quad . \quad (3.11)$$

Here,  $A$  is defined as

$$A \equiv \left( \frac{V_t}{|V_a|} \right) \left( \frac{R_g - R_a}{R_a} \right) - 1 \quad . \quad (3.12)$$

If equation (3.11) is separated, the travel time in the second region may be given as

$$t_2 = \left( \frac{m}{2q|V_a|} \right)^{1/2} \left( \frac{R_g - R_a}{R_a} \right)^{1/2} \int_{R_a}^{R_g} \sqrt{\frac{dr}{\frac{R_g}{r} + A}} \quad . \quad (3.13)$$

By performing the indicated integration, the travel time in the second region can be expressed as

$$t_2 = \left( \frac{m}{2q|V_a|} \right)^{1/2} (R_g - R_a) B \quad , \quad (3.14)$$

where  $B$  is given as

$$B \equiv A^{-1/2} \left[ \left( \frac{R_g^2(1+A)}{AR_a(R_g-R_a)} \right)^{1/2} - \left( \frac{R_g+AR_a}{A(R_g-R_a)} \right)^{1/2} + \frac{R_g}{A\sqrt{R_a(R_g-R_a)}} \ln \left( \frac{\sqrt{R_a} + \left( \frac{R_g+R_a}{A} \right)^{1/2}}{\sqrt{R_g} + \left( \frac{R_g+R_a}{A} \right)^{1/2}} \right) \right] \quad (3.15)$$

and  $A$  is as defined in identity (3.12).

In the third region, between the grounded flat and 6.5-cm radius hemispherically curved grid, the potential is everywhere zero, and ions traverse the 0.015-m path,  $R_g - R_a$ , in free-flight. Here,  $R_g$  and  $R_a$  are the on-axis distances between the tip and the hemispherically curved or flat grid, 0.137 and 0.122 m, respectively. Ions enter this region with the terminal kinetic energy obtained in the second region. That is:

$$\frac{1}{2} mv^2 = q V_t \quad , \quad (3.16)$$

where equation (3.16) is obtained from equation (3.10) at the boundary, equations (3.5),  $V(R_g) = 0$ . The free-flight travel time in the third region is then given by

$$t_3 = \left( \frac{m}{2qV_t} \right)^{1/2} (R_g - R_a) \quad . \quad (3.17)$$

The 0.0015-m on-axis flight path,  $R_T - R_G$ , in the fourth and final region is between the grounded hemispherically curved grid and the negative 4.5-kV potential,  $V_{chl}$ , input plate of the Chevron CEMA. This post-acceleration region is terminated by the detector input plate at a distance,  $R_T$ , of 0.138 m from the tip. The on-axis potential,  $V'(r)$ , within this region between the closely spaced grid and detector plate is essentially linear and may be written as

$$V'(r) = \left[ \frac{V_{chl}}{R_T - R_G} \right] (r - R_G) \quad . \quad (3.18)$$

An ion's energy within the post-acceleration region must equal the initial energy with which it entered. Since the third region is free-flight, the ion's initial energy is  $qV_t$  from equation (3.16) and the ion's energy within the region is given as

$$\frac{1}{2} mv^2 + qV'(r) = qV_t \quad . \quad (3.19)$$

By substituting equation (3.18) for  $V'(r)$  and solving for the velocity, one obtains

$$\frac{dr}{dt} = \left( \frac{2q}{m} \right)^{1/2} \left[ V_t - \frac{V_{chl}}{R_T - R_G} (r - R_G) \right]^{1/2} \quad . \quad (3.20)$$

If equation (3.20) is separated and the substitution  $V_{chl} = -|V_{chl}|$  made, the on-axis travel time,  $t_4$ , in the post-acceleration region may be given as

$$t_4 = \left(\frac{m}{2q}\right)^{1/2} \int_{R_g}^{R_T} \left[ v_t - \frac{|v_{chl}| R_g}{R_T - R_g} + \frac{|v_{chl}| r}{R_T - R_g} \right]^{-1/2} dr . \quad (3.21)$$

By performing the integration indicated in equation (3.21), the travel time in the post-acceleration region is obtained. That is:

$$t_4 = \left(\frac{m}{2q}\right)^{1/2} \left( \frac{R_T - R_g}{|v_{chl}|} \right) \left( \frac{\sqrt{v_t + |v_{chl}|} - \sqrt{v_t}}{2} \right) . \quad (3.22)$$

An ion's total flight time through the instrument is the sum of time required to traverse the four regions. That is:

$$T = \sum_{i=1}^4 t_i . \quad (3.23)$$

By substituting equations (3.1), (3.14), (3.17), and (3.22) into equation (3.23) and solving for  $m/n$ , one obtains the absolute flight equation for this instrument,

$$\frac{m}{n} = K \left[ \left( \frac{1}{v_T} \right)^{1/2} R_a + \left( \frac{1}{|v_a|} \right)^{1/2} (R_g - R_a) B + \left( \frac{1}{v_t} \right)^{1/2} (R_g - R_g) \right. \\ \left. + \left( \frac{R_T - R_g}{|v_{chl}|} \right) \left( \frac{\sqrt{v_t + |v_{chl}|} - \sqrt{v_t}}{2} \right)^{-2} T^2 \right] . \quad (3.24)$$

Here,  $m/n$  is expressed in atomic mass units (amu) since  $q$  has been replaced by  $n_e$ , and  $K$  is as given in equation (2.6). In equation (3.24),  $\alpha$  is implicit in  $V_T$  and  $V_t$  as is  $\delta$  in  $T$ , and both the pulse factor and instrumentation delay are required to calibrate the instrument.

Finally, it is evident that the relative flight equation given in expression (2.12) remains valid, since it may be obtained from equation (3.24) in the same manner as it was obtained from equation (2.11).

## 2. Time Dispersion and the Pulse Factor

Equation (3.24) may be used to identify an isolated unknown mass-to-charge species provided the instrument is calibrated by determining both the pulse factor,  $\alpha$ , and the instrumentation delay,  $\delta$ . The instrumentation delay is simply the net instrumental "through-put" time between mass and timing signals, and it is easily determined by direct measurement, Appendix equation (A.2), or from relative flight times of known species. However, the determination of the pulse factor is not straightforward, and it is not readily evident that it is effective in accounting for the time-dependent pulse "overshoot."

The following treatment describes the effect of a simple time-dependent "overshoot" on an ion's energy, flight time, and time dispersion. This rudimentary treatment is based on the concepts of energy deficit<sup>42</sup> and field enhancement.<sup>29</sup> It demonstrates that the effect of a time-dependent "overshoot" may be approximately accounted for by an average additional electrostatic contribution,  $\alpha V_{ep}$ , to the ion's energy. Here,  $V_{ep}$  is the pedestal value of the evaporation pulse potential as given by equation (2.34). In addition, the pulse factor

and field enhancement factor,  $f$ , are related and their influence on the time-dispersion, or mass resolution, of the mass spectrometer is established. Finally, this approach indicates that at a constant evaporation rate  $\alpha$  varies very slowly with the pulse to bias potential ratio for reasonable spatial potentials, and this provides the means for determining the pulse factor. In fact, both  $\alpha$  and  $f$  may be simultaneously obtained for a known species by varying the pulse to bias ratio while maintaining a constant rate of field evaporation. This procedure is employed in the next section to complete the desired calibration.

The simplified system upon which this calculation is based is shown in Figure 11(a). There,  $r_t$  is the radius of the tip apex and  $V(r_t, t)$  is the time-dependent tip potential shown in Figure 11(d). Also, the counter electrode negative or ground potential,  $V_a$ , and the radii  $R_a$  and  $R_T$  are identical to those given in Section 1. The time-dependent tip potential may be written as

$$V(r_t, t) = V_{tb} + V_{ep} + v(t) , \quad (3.25)$$

where  $V_{tb}$  is the positive tip bias as in equation (2.1), and  $v(t)$  expresses the time-dependent portion of the potential. Here,  $v(t)$  is given as

$$v(t) = \begin{cases} (f-1)V_{ep} & 0 < t < \tau \\ 0 & \tau < t < t_w \\ -V_{ep} & t > t_w \end{cases} , \quad (3.26)$$

where  $\tau$  is the duration of the potential "overshoot,"  $(f-1)V_{ep}$  and  $f$  are the field enhancement factor.<sup>29</sup> If the duration,  $t_w$ , of the pulse

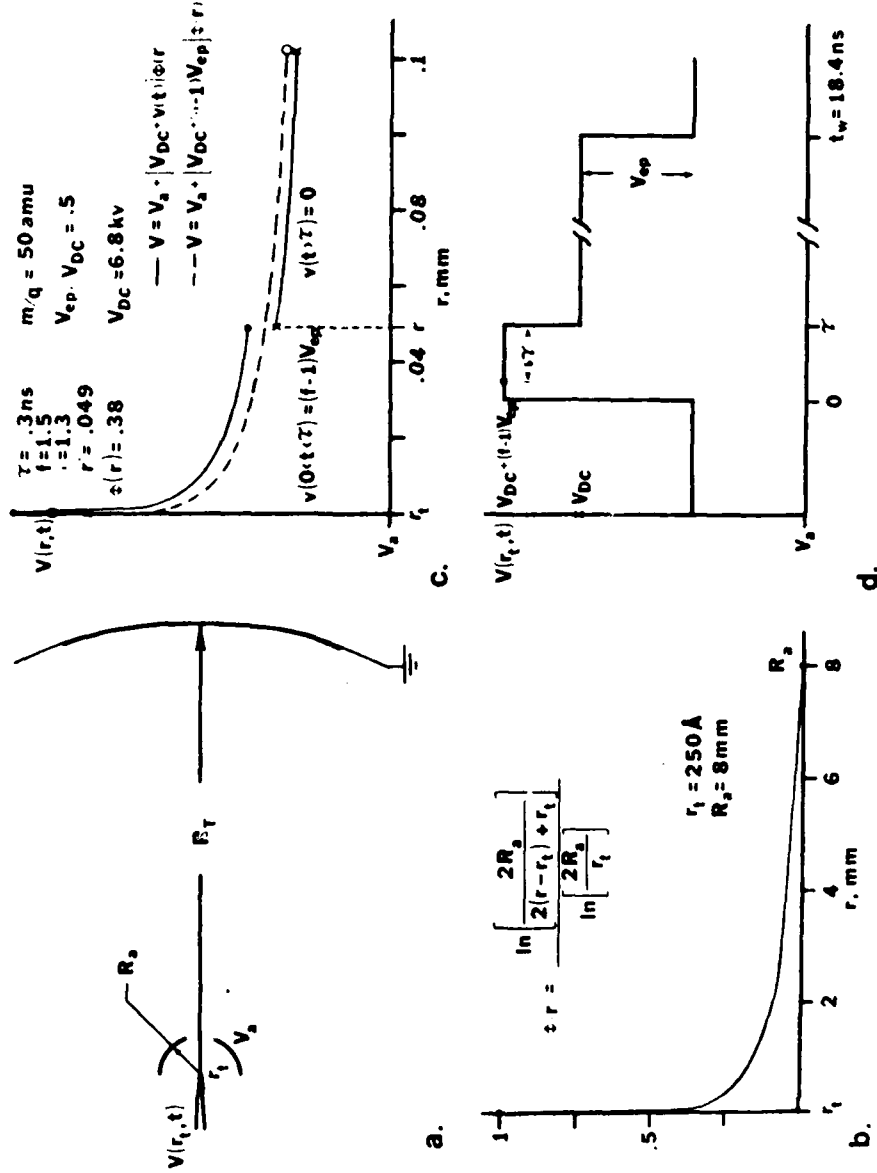


Figure 11. A simplified arrangement from which a pulse factor and time dispersion may be calculated. (a) System diagram, (b) spatial potential, (c) a potential resulting from a step pulse overshoot, and (d) an idealized pulse shape.

pedestal is sufficiently long, e.g., 18 ns, an ion will acquire the full pedestal contribution to its kinetic energy,  $qV_{ep}$ , and  $V_{ep}$  may be treated as an electrostatic potential. That is, equation (3.26) may be rewritten as

$$v(t) = \begin{cases} (f-1)V_{ep} & 0 < t < \tau \\ 0 & t > \tau \end{cases} . \quad (3.27)$$

The experimentally measured electrostatic potentials,  $V_{DC}$ , provide an evaporated ion with a kinetic energy at  $R_a$  given by

$$KE(R_a) = qV_{DC} . \quad (3.28)$$

Here,  $V_{DC}$  includes the pedestal contribution. That is:

$$V_{DC} = V_{tb} + V_{ep} - V_a . \quad (3.29)$$

Equation (3.25) may now be rewritten as

$$V(r_t, t) = V_{DC} + V_a + v(t) . \quad (3.30)$$

Since the time required to alter the spatial potential at a distance  $r$  is brief compared to ion travel times, the spatial potential,  $V(r, t)$ , in the region between the tip and the counter electrode may be separated into time and space dependent parts. That is:

$$V(r, t) = V_a + [V(r_t, t) - V_a]\phi(r) . \quad (3.31)$$

If equation (3.30) is substituted for  $V(r_t, t)$ , equation (3.31) may be written as

$$V(r, t) = V_a + [V_{DC} + v(t)]\phi(r) , \quad (3.32)$$

where  $v(t)$  is given by equation (3.27), and  $\phi(r)$  must satisfy the boundary conditions

$$\phi(r) = \begin{cases} 1 & r = r_t \\ 0 & r = R_a \end{cases} . \quad (3.33)$$

The spatial dependence,  $\phi(r)$ , may be approximated from a confocal paraboloid geometry.<sup>65,66</sup> That is:

$$\phi(r) = \frac{\ln \left[ \frac{2R_a}{2(r-r_t) + r_t} \right]}{\ln \left[ \frac{2R_a}{r_t} \right]} . \quad (3.34)$$

Equation (3.34) is graphed in Figure 11(b) using representative values for the radii of the tip apex,  $r_t = 250 \text{ } \text{\AA}$ , and the counter electrode,  $R_a = 8 \text{ mm}$ .

Although the separation of  $V(r,t)$  into space and time portions is reasonable for the indicated period of the evaporation pulse, it should be understood that both the pulse shape and the spatial dependence are rough approximations. This is clear in the assumed square wave evaporation pulse, Figure 11(d), but the extent of the approximations is not evident in  $\phi(r)$ . For example, the effect of the counter electrode on  $\phi(r)$  is small during the early portion of the "overshoot",  $\tau - \delta\tau \sim 100 \text{ picoseconds}$ , and  $\phi(r)$  is principally dependent on the geometry of the tip. This implicit time dependence is present in  $\phi(r)$ , since a change in tip potential (transmitted at the speed of light) requires  $\sim 30 \text{ picoseconds}$  to reach the counter electrode. Further, in the initial 6 picoseconds an evaporated ion will acquire 20 to 40% (200 to 1 amu, respectively) of its terminal kinetic energy at  $R_a$ . Despite these limitations, the following analysis provides a

means for determining  $\alpha$  and, hence, calibrating the instrument. In addition, it yields time dispersions which are in reasonable agreement with those observed and indicates those conditions which favor improved mass resolution.

The solid curve in Figure 11(d) is a plot of the time dependent spatial potential given by equation (3.32) for a pulse fraction of 50%,  $V_{ep} / V_{DC} = 0.5$ . There,  $r^*$  is the distance an ion of mass  $m$ , i.e., 50 amu, travels during the effective width,  $\delta\tau$ , of the "overshoot", i.e.,  $\delta\tau = \tau = 0.3$  ns, and  $\phi(r^*)$  is the value of  $\phi(r)$  at  $r^*$ . The dashed curve is a plot of an electrostatic potential,

$$V(r) = V_a + [V_{DC} + (\alpha-1)V_{ep}] \phi(r) , \quad (3.35)$$

which yields a total flight time,  $t_T$ , equivalent to that resulting from  $V(r,t)$ . Here,  $t_T$  is the time required for an ion to transverse the distance  $R_t - r_t$ , and  $q(\alpha-1)V_{ep}$  is the average additional electrostatic contribution to an ion's energy required to account for the effect of  $v(t)$ . The pulse factor,  $\alpha$ , is mainly dependent upon  $f$  and  $\phi(r^*)$ , and its value of 1.3 is obtained from  $f = 1.5$  and  $\phi(r^*) = 0.38$  in the following manner.

Within the region  $r_t < r < r^*$ , an ion's kinetic energy may be given as

$$\frac{1}{2} mv^2 = q [V(r_t, \tau - \delta\tau) - V(r, t)] . \quad (3.36)$$

By using equations (3.32) and (3.27) and the boundary condition (3.33), equation (3.36) may be rewritten as

$$\frac{1}{2} mv^2 = q [V_{DC} + (f-1)V_{ep}] [1 - \phi(r)] . \quad (3.37)$$

Solving equation (3.37) for the velocity yields

$$\frac{dr}{dt} = \left[ \frac{2qV_{DC}}{m} \right]^{\frac{1}{2}} \left[ 1 + \frac{(f-1)V_{ep}}{V_{DC}} \right]^{\frac{1}{2}} \left[ 1 - \phi(r) \right]^{\frac{1}{2}}. \quad (3.38)$$

If equation (3.38) is separated, the travel time,  $\delta\tau$ , from  $r_t$  to  $r^*$  may be written as

$$\delta\tau = \left[ 1 + \frac{(f-1)V_{ep}}{V_{DC}} \right]^{-\frac{1}{2}} \left[ \frac{m}{2qV_{DC}} \right]^{\frac{1}{2}} \int_{r_t}^{r^*} \frac{dr}{[1-\phi(r)]^{\frac{1}{2}}}. \quad (3.39)$$

Similarly, an ion's kinetic energy within the region  $r^* < r < R_a$  may be given as

$$\frac{1}{2}mv^2 = q[V(r^*, t) - V(r, t)] + KE(r^*). \quad (3.40)$$

Since  $v(t)=0$  for  $t > \tau$ , equation (3.27), the potential difference,  $V(r^*, t) - V(r, t)$ , may be rewritten by using equation (3.32). That is:

$$V(r^*, t) - V(r, t) = V_{DC}[\phi(r^*) - \phi(r)]. \quad (3.41)$$

Further, the ion's kinetic energy at  $r^*$  may be obtained from equation (3.37). That is:

$$KE(r^*) = q[V_{DC} + (f-1)V_{ep}] [1-\phi(r^*)]. \quad (3.42)$$

If equations (3.41) and (3.42) are substituted into equation (3.40), one obtains

$$\frac{1}{2}mv^2 = qV_{DC}[1-\phi(r)] + q(f-1)V_{ep}[1-\phi(r^*)]. \quad (3.43)$$

Solving equation (3.42) for the velocity yields

$$\frac{dr}{dt} = \left[ \frac{2qV_{DC}}{m} \right]^{\frac{1}{2}} \left[ 1-\phi(r) \right]^{\frac{1}{2}} \left[ 1 + \frac{(f-1)V_{ep}}{V_{DC}} \left( \frac{1-\phi(r^*)}{1-\phi(r)} \right) \right]^{\frac{1}{2}}. \quad (3.44)$$

By separating relation (3.44) and indicating the required integration, the travel time,  $t_1 - \tau$ , from  $r^*$  to  $R_a$  may be written as

$$t_1 - \tau = \left[ \frac{m}{2qV_{DC}} \right]^{\frac{1}{2}} \int_{r^*}^{R_a} \frac{dr}{\left[ \frac{1-\phi(r)}{1-\phi(r^*)} \right]^{\frac{1}{2}} \left[ 1 + \frac{(f-1) V_{ep}}{V_{DC}} \left( \frac{1-\phi(r^*)}{1-\phi(r)} \right)^{\frac{1}{2}} \right]} . \quad (3.45)$$

Since

$$\frac{(f-1) V_{ep}}{V_{DC}} \left( \frac{1-\phi(r^*)}{1-\phi(r)} \right) \leq 1 \quad (3.46)$$

and, in particular, much less than 1 for reasonable values, 0.1 to 0.2, of  $V_{ep} / V_{DC}$ , the second term in the denominator under the integral may be expanded. That is:

$$\left[ 1 + \frac{(f-1) V_{ep}}{V_{DC}} \left( \frac{1-\phi(r^*)}{1-\phi(r)} \right) \right]^{-\frac{1}{2}} \approx 1 - \frac{1}{2} \frac{(f-1) V_{ep}}{V_{DC}} \left( \frac{1-\phi(r^*)}{1-\phi(r)} \right) . \quad (3.47)$$

Expression (3.45) may now be written as

$$t_1 = \left[ \frac{m}{2q V_{DC}} \right]^{\frac{1}{2}} \left[ \int_{r^*}^{R_a} \frac{dr}{[1-\phi(r)]^{\frac{1}{2}}} - \frac{1}{2} \frac{(f-1) V_{ep}}{V_{DC}} [1-\phi(r^*)] \right. \\ \left. \int_{r^*}^{R_a} \frac{dr}{[1-\phi(r)]^{\frac{3}{2}}} \right] + \tau . \quad (3.48)$$

Since  $R_a \gg r^*$  and  $\phi(r)$  decreases rapidly with increasing  $r$ , the integrals in equation (3.48) may be approximated.

That is:

$$\int_{r^*}^{R_a} \frac{dr}{[1-\phi(r)]^{1/2}} \approx R_a - r^* \text{ and } \int_{r^*}^{R_a} \frac{dr}{[1-\phi(r)]^{3/2}} \approx R_a - r^*. \quad (3.49)$$

Here, only the first terms from the integration of the binomial expansion of each integral argument are retained. The full expressions,

$$\int_{r^*}^{R_a} [1-\phi(r)]^{-1/2} dr = R_a - r^* + \sum_{i=1}^{\infty} \frac{\prod_{j=0}^{i-1} (\frac{1}{2} + j)}{i!} \int_{r^*}^{R_a} \phi(r)^i dr \quad (3.50)$$

and

$$\int_{r^*}^{R_a} [1-\phi(r)]^{-3/2} dr = R_a - r^* + \sum_{i=1}^{\infty} -\frac{(1+2i)}{i!} \prod_{j=0}^{i-1} (\frac{1}{2} + j) \int_{r^*}^{R_a} \phi(r)^i dr, \quad (3.51)$$

may be used to obtain further accuracy at heavy masses,  $r^*$  decreases with decreasing values of both  $m$  and  $R_a$ . In particular, the integral terms of the series may be evaluated for a confocal paraboloid potential. That is:

$$\int_{r^*}^{R_a} \phi(r)^i dr = \left( \ln \frac{2R_a}{r_t} \right)^i \int_{r^*}^{R_a} [\ln 2R_a - \ln(2r - r_t)]^i dr. \quad (3.52)$$

These integrals are in standard form and may be evaluated once  $r^*$  is obtained from equation (3.39) for a given value of  $\delta\tau$ . If  $\delta\tau$  is of reasonable duration,  $\geq 0.3$  ns,  $r^*$  may be approximated, from equation (3.39), as

$$r^* \approx \left[ 1 + \frac{(f-1)V_{ep}}{V_{DC}} \right]^{\frac{1}{2}} \left[ \frac{2q V_{DC}}{m} \right]^{\frac{1}{2}} \delta\tau + r_t , \quad (3.53)$$

while for short periods, e.g.,  $\delta\tau = 6$  picoseconds, the integral in equation (3.39) must be evaluated. For a confocal paraboloid potential, the integral in equation (3.39) may be given as

$$\int_{r_t}^{r^*} \frac{dr}{[1-\phi(r)]^{\frac{1}{2}}} = \left[ \ln \frac{r_t}{2R_a} \right]^{\frac{1}{2}} \int_0^{r^*-r_t} \frac{dr'}{\left[ \ln \frac{r_t}{2r'+r_t} \right]^{\frac{1}{2}}} , \quad (3.54)$$

where  $r' = r - r_t$ . The integral on the right side of equation (3.54) can be written in standard form by the substitution:

$$u = \left[ \ln \frac{r_t}{2r' + r_t} \right]^{\frac{1}{2}} . \quad (3.55)$$

That is:

$$\int_{r_t}^{r^*} \frac{dr}{[1-\phi(r)]^{\frac{1}{2}}} = -r_t \left[ \ln \frac{r_t}{2R_a} \right]^{\frac{1}{2}} \int_0^{\left[ \ln \frac{r_t}{2r^*-r_t} \right]^{\frac{1}{2}}} e^{-u} du . \quad (3.56)$$

The value of the integral on the right side of (3.56) is given by the error function. This completes the evaluation of equation (3.39).

That is:

$$\delta\tau = \left[ \frac{m}{2q[V_{DC} + (f-1)V_{ep}]} \right]^{\frac{1}{2}} \left[ \ln \frac{2R_a}{r_t} \ln \frac{2r^*-r_t}{r_t} \right]^{\frac{1}{2}} r_t$$

$$\left[ 1 + \sum_{i=1}^{\infty} \frac{\left( \ln \frac{2r^*-r_t}{r_t} \right)^i}{i! (2i+1)} \right] . \quad (3.57)$$

Equation (3.57) provides the necessary relation between  $\delta\tau$  and  $r^*$  for extremely brief evaporation periods.

Since the required terms have now been obtained, the evaluation of equation (3.48) may be completed. By using relation (3.49), the travel time from  $r^*$  to  $R_a$  may be given as

$$t_1 \approx \left[ \frac{m}{2q V_{DC}} \right]^{\frac{1}{2}} \left[ 1 - \frac{1}{2} \frac{(f-1) V_{ep}}{V_{DC}} \left[ 1 - \phi(r^*) \right] \right] (R_a - r^*) + \tau. \quad (3.58)$$

The remaining travel time,  $t_2$ , from  $R_a$  to  $R_T$  is now obtained for an ion in free flight,  $v_a = 0$ . This is representative of most atom-probe mass spectrometers, and the results are applicable to both the free and retarded modes of this instrument. The time  $t_2$  may be given as

$$t_2 = \frac{1}{v_a} (R_T - R_a) \quad (3.59)$$

where the initial velocity at  $R_a$ ,  $v_a$ , is represented by

$$v_a = \left( \frac{2KE(R_a)}{m} \right)^{\frac{1}{2}}. \quad (3.60)$$

Here, the kinetic energy at  $R_a$ ,  $KE(R_a)$ , may be obtained from equation (3.43). That is:

$$KE(R_a) = q V_{DC} [1 - \phi(R_a)] + q (f-1) V_{ep} [1 - \phi(r^*)]. \quad (3.61)$$

Since  $\phi(R_a) = 0$  by the boundary condition (3.33), equation (3.60) may be rewritten as

$$v_a = \left[ \frac{2q V_{DC}}{m} \right]^{\frac{1}{2}} \left[ 1 + \frac{(f-1) V_{ep}}{V_{DC}} \left[ 1 - \phi(r^*) \right] \right]^{\frac{1}{2}}, \quad (3.62)$$

and equation (3.59) may be given as

$$t_2 \approx \left[ \frac{m}{2q V_{DC}} \right]^{\frac{1}{2}} \left[ 1 - \frac{1}{2} \frac{(f-1)V_{ep}}{V_{DC}} [1-\phi(r^*)] \right] (R_T - R_a). \quad (3.63)$$

Here, the reciprocal of the second square-root term in equation (3.62) has been expanded retaining only first-order terms as in equation (3.47).

The total flight time,  $t_T$ , from  $r_t$  to  $R_T$  is the sum of  $t_1$  and  $t_2$ .

By substituting equations (3.63) and (3.58) into  $t_T = t_1 + t_2$ , the total flight time may be written as

$$t_T = \left[ \frac{m}{2q V_{DC}} \right]^{\frac{1}{2}} \left[ 1 - \frac{1}{2} \frac{(f-1)V_{ep}}{V_{DC}} [1-\phi(r^*)] \right] (R_T - r^*) + \tau. \quad (3.64)$$

The total flight time, given to first order by equation (3.64), is that of an ion with an initial velocity  $v_a$  at  $\tau$  in free flight for a distance  $R_T - r^*$ . The total flight time obtained from (3.64) is less ( $\tau$  is extremely brief) than that which would result solely from the measured electrostatic potentials,

$$t_T (\text{el.}) = \left[ \frac{m}{2q V_{DC}} \right]^{\frac{1}{2}} (R_T - r_t). \quad (3.65)$$

This decrease results from the additional kinetic energy,

$q (f-1) V_{ep} [1-\phi(r^*)]$ , imparted to the field evaporated ions by the potential "overshoot",  $(f-1)V_{ep}$ . A pulse factor,  $\alpha$ , may now be defined such that the total calculated flight time,  $t_T$  (cal.), is given by

$$t_T (\text{cal.}) = \left[ \frac{m}{2q [V_{DC} + (\alpha-1)V_{ep}]} \right]^{\frac{1}{2}} \left[ \int_{r_t}^{R_a} \frac{dr}{[1-\phi(r)]^2} + (R_T - R_a) \right]. \quad (3.66)$$

Here,  $V_{DC}$  is given by equation (3.29), and, as before, it is the sum of the measured electrostatic potentials (including the pedestal value,  $V_{ep}$ , of the evaporation pulse). If the first term on the right side of equation (3.66) is expanded and the integral approximated by  $R_a - r_t$ , equation (3.66) may be given as

$$t_T \text{ (cal.)} \approx \left[ \frac{m}{2q V_{DC}} \right]^{\frac{1}{2}} \left[ 1 - \frac{1}{2} \frac{(\alpha-1) V_{ep}}{V_{DC}} \right] (R_T - r_t) \quad (3.67)$$

By equating equations (3.67) and (3.64), an expression for evaluating  $\alpha$  may now be obtained. That is:

$$\left[ 1 - \frac{1}{2} \frac{(\alpha-1) V_{ep}}{V_{DC}} \right] = \left[ 1 - \frac{1}{2} \frac{(f-1) V_{ep}}{V_{DC}} \left[ 1 - \phi(r^*) \right] \right] \frac{R_T - r^*}{R_T - r_t} + \frac{\tau}{t_T (el.)} \quad (3.68)$$

Since an atom-probe may be calibrated using the "sharp" leading edge of a given spectral line (earliest arriving ions),  $\alpha$  at  $\delta\tau = \tau$  (defined as  $\alpha_\tau$ ) is the appropriate parameter. Using either equation (3.53) or (3.57) with  $\delta\tau = \tau$ , equation (3.68) may be used to obtain  $\alpha_\tau$ . In particular, equation (3.53) may be solved for  $\tau$  (the reciprocal square root expanded), and the result then substituted for  $\tau$  in relation (3.68). This substitution in conjunction with that for  $t_T \text{ (el.)}$  from equation (3.65) yields

$$1 - \frac{1}{2} \frac{(\alpha_{\tau-1}) V_{ep}}{V_{DC}} = 1 - \frac{1}{2} \frac{(f-1) V_{ep}}{V_{DC}} + \frac{1}{2} \frac{(f-1) V_{ep}}{V_{DC}} \phi(r^*) \left( \frac{R_T - r^*}{R_T - r_t} \right). \quad (3.69)$$

Here, part of the multiplication indicated on the right side of (3.68) has been performed and the expression regrouped to cancel terms.

Equation (3.69) may now be written as

$$(\alpha_T - 1) = (f-1) \left[ 1 - \left( \frac{R_T - r^*}{R_T - r_t} \right) \phi(r^*) \right] , \quad (3.70)$$

or, since  $R_T$  is much greater than  $r^*$  and  $r_t$ ,

$$(\alpha_T - 1) \approx (f-1) [1 - \phi(r^*)] . \quad (3.71)$$

In equation (3.70),  $f$  and  $R_T$  are fixed by the system-sample geometry as is the functional form of  $\phi$ , and variations in  $r_t$  (200 - 800 Å) do not result explicitly in significant changes in  $\alpha_T$ . However,  $r^*$  varies with both the ionic mass-to-charge ratio and the total specimen potential, equations (3.30) and (3.27). This results in the slow decrease of  $\alpha_T$  with  $m/q$  shown in Figure 12(a). For a given species,  $m_o$ ,  $r^*$  and, hence,  $\alpha_T$  will remain constant at a slow and constant pulse field evaporation rate,

$$r_t \approx \text{constant and } V_{DC} + (f-1) V_{ep} = \text{constant}, \quad (3.72)$$

respectively. That is, an experimental value,  $\alpha_T(m_o)$ , of the pulse factor may be determined which will calibrate the spectrometer. Such a calibration is conducted in the next section using singly isotopic rhodium.

Finally, it is possible to obtain the approximate form and range of the instrument's time dispersion and, consequently, the expected mass resolution. Here, the maximum time dispersion,  $D(t_T)$ , is given as

$$D(t_T) \equiv t_T(0) - t_T(\tau) , \quad (3.73)$$

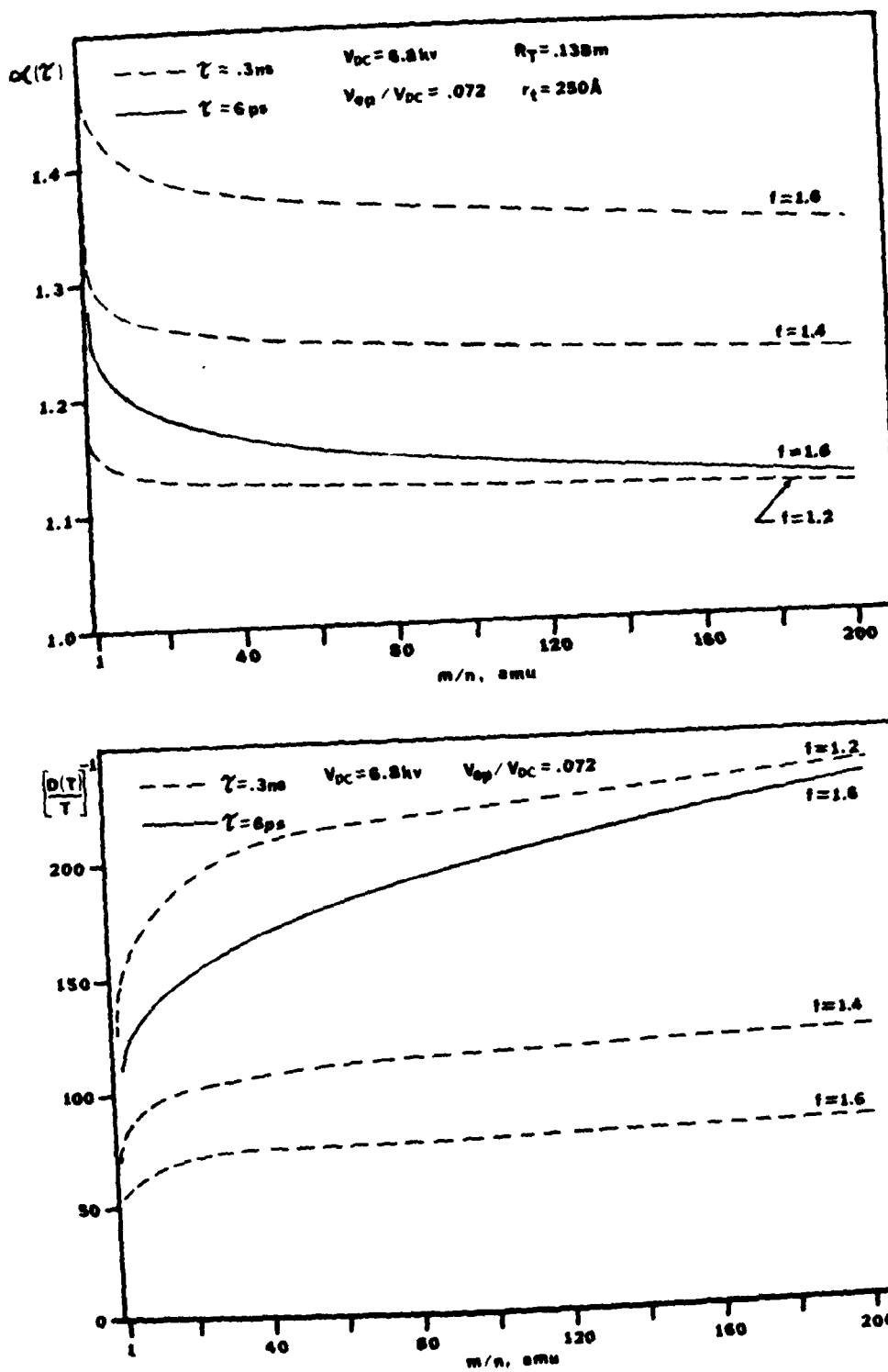


Figure 12. Time resolutions and pulse factors calculated for a few overshoot heights and widths. (a) The pulse factor's dependence on mass-to-charge and (b) a similar time resolution dependence.

where

$$t_T(0) = t_T @ \delta\tau = 0$$

and

$$t_T(\tau) = t_T @ \delta\tau = \tau. \quad (3.74)$$

For an ion which evaporates at the beginning of the pulse "overshoot", the total flight time,  $t_T(\tau)$ , may be obtained from equation (3.64), where  $r^*$  and  $\tau$  are related by equation (3.53) with  $\delta\tau = \tau$  or similarly using equation (3.57). By replacing  $(R_T - r^*)$  with  $(R_T - r_t) - (r^* - r_t)$ , equation (3.64) yields

$$t_T(\tau) = \left[ \frac{m}{2q V_{DC}} \right]^{\frac{1}{2}} (R_T - r_t) + \tau - \left[ \frac{m}{2q V_{DC}} \right]^{\frac{1}{2}} (R_T - r_t) \left[ \frac{r^* - r_t}{R_T - r_t} + \frac{1}{2} \frac{(f-1)V_{ep}}{V_{DC}} \left[ 1 - \phi(r^*) \right] \left[ 1 - \frac{r^* - r_t}{R_T - r_t} \right] \right]. \quad (3.75)$$

Here, the first two terms on the right side of equation (3.75) are equivalent to the flight time,  $t_T(0)$ , of an ion evaporated at the end of the "overshoot". That is,  $t_T(0)$  as obtained from equation (3.64) is

$$t_T(0) = \left[ \frac{m}{2q V_{DC}} \right]^{\frac{1}{2}} (R_T - r_t) + \tau, \quad (3.76)$$

since  $\delta\tau = 0$  implies  $r^* = r_t$  and  $[1 - \phi(r_t)] = 0$  by boundary conditions (3.33). Hence,  $D(t_T)$  as defined in relation (3.73) may be written as

$$D(t_T) = \left[ \frac{m}{2q V_{DC}} \right]^{\frac{1}{2}} (R_T - r_t) \left[ \frac{r^* - r_t}{R_T - r_t} + \frac{1}{2} \frac{(f-1)V_{ep}}{V_{DC}} \left[ 1 - \phi(r^*) \right] \left[ 1 - \frac{r^* - r_t}{R_T - r_t} \right] \right]. \quad (3.77)$$

The fractional time dispersion,

$$\frac{D(t_T)}{t_T(\tau)} = \frac{t_T(0) - t_T(\tau)}{t_T(\tau)}, \quad (3.78)$$

may be obtained from equations (3.77) and (3.75) once  $\tau$  in (3.75) is represented in terms of  $r^*$ . In particular,  $\tau$  may be obtained from equation (3.53). That is:

$$\tau \approx \left[ \frac{m}{2q V_{DC}} \right]^{\frac{1}{2}} \left[ 1 - \frac{1}{2} \frac{(f-1) V_{ep}}{V_{DC}} \right] (r^* - r_t). \quad (3.79)$$

By replacing  $\tau$  in relation (3.75) with expression (3.79) and canceling like terms of opposite sign, equation (3.75) may be rewritten as

$$t_T(\tau) = \left[ \frac{m}{2q V_{DC}} \right]^{\frac{1}{2}} (R_T - r_t) \left[ 1 - \frac{1}{2} \frac{(f-1) V_{ep}}{V_{DC}} \left[ 1 - \phi(r^*) + \phi(r^*) \left( \frac{r^* - r_t}{R_T - r_t} \right) \right] \right] \quad (3.80)$$

If equation (3.80) is divided into equation (3.77) and the resulting denominator expanded,

$$\left[ 1 - \frac{1}{2} \frac{(f-1) V_{ep}}{V_{DC}} \left[ 1 - \phi(r^*) + \phi(r^*) \left( \frac{r^* - r_t}{R_T - r_t} \right) \right] \right]^{-1} \approx 1 + \frac{1}{2} \frac{(f-1) V_{ep}}{V_{DC}} \left[ 1 - \phi(r^*) + \phi(r^*) \left( \frac{r^* - r_t}{R_T - r_t} \right) \right], \quad (3.81)$$

the fractional time dispersion is given as

$$\frac{D(t_T)}{t_T(\tau)} \approx \left[ 1 + \frac{1}{2} \frac{(f-1) v_{ep}}{v_{DC}} \left[ 1 - \phi(r^*) + \phi(r^*) \left( \frac{r^* - r_t}{R_T - r_t} \right) \right] \right] \\ \left[ \frac{r^* - r_t}{R_T - r_t} + \frac{1}{2} \frac{(f-1) v_{ep}}{v_{DC}} \left[ 1 - \phi(r^*) \right] \left[ 1 - \frac{r^* - r_t}{R_T - r_t} \right] \right] . \quad (3.82)$$

If the indicated multiplication is performed, like terms of opposite sign canceled, and terms in  $\frac{(f-1) v_{ep}}{v_{DC}}^2$  and  $\left( \frac{r^* - r_t}{R_T - r_t} \right)^2$  neglected, the fractional dispersion may be approximated as

$$\frac{D(t_T)}{t_T(\tau)} \approx \frac{1}{2} \frac{(f-1) v_{ep}}{v_{DC}} \left[ 1 - \phi(r^*) \right] + \frac{r^* - r_t}{R_T - r_t} . \quad (3.83)$$

Alternatively, by equations (3.71), (3.79), and (3.80), a rough experimental estimate of the maximum fractional time dispersion at mass  $m_0$  can be written as

$$\frac{D(t_T)}{t_T} \approx \frac{1}{2} \frac{[\alpha_T(m_0) - 1] v_{ep}}{v_{DC}} + \frac{\tau}{t_T} . \quad (3.84)$$

The reciprocal of the fractional dispersion for several "overshoot" heights and widths is plotted against mass-to-charge ratio in Figure 12(b) yielding the time resolution for various ionic species. Spectral lines obtained by collecting a large number of ions exhibit a base line resolution of about 60, which is in agreement with the curve in Figure 12(b) for an "overshoot" height and width of  $0.6 v_{ep}$  ( $f=1.6$ ) and 0.3 ns, respectively. In addition, observed resolution increases rapidly when measured at larger percentages of abundance, e.g.,  $t/\Delta t \approx 150$  at 20% above the base line, which indicates a peaked rather than rectangular

pulse "overshoot" profile. That is, the maximum yield of ions occurs during a brief interval about the "overshoot" peak and results in a minimal time dispersion, while reduced ion yields during the leading and trailing edge of the "overshoot" arrive later in time with a broader spread. For ions evaporated during the peak, the time resolution may be represented by the curve in Figure 12(b) for a height and width of  $0.6 V_{ep}$  ( $f=1.6$ ) and 6 ps, respectively. This proposed peak profile is further supported in the next section where the "overshoot" height is experimentally determined to be  $0.6 V_{ep}$  ( $f=1.6$ ).

Finally, it is clear from equation (3.83) or (3.84) that resolution may be increased by reducing both the width and height of the electrical pulse "overshoot" or that order of magnitude increases may be obtained by using pulsed laser-induced evaporation. In the case of laser-induced evaporation, the first term on the right of either (3.83) or (3.84) would be negligible, while the second term depends only on the laser pulse width and the total flight time.

### 3. Calibration, Final Flight Equations

Both the pulse factor,  $\alpha_T(m_0)$ , and the field enhancement factor,  $f$ , may be simultaneously obtained for a known species,  $m_0$ , by varying the pulse to bias ratio while maintaining a slow and constant, equation (3.72), rate of field evaporation. In addition, the counter electrode potential,  $V_a$ , must remain constant to insure that an error in the analytical form assumed for this instrument's electrostatic retarding potential does not implicitly effect the value of  $\alpha_T(m_0)$ , and that this error may be treated separately.

The experimental data used to determine  $\alpha_T(m_0)$  and  $f$  were obtained by field evaporating several layers of a 001 oriented rhodium tip at a constant rate of  $8$  to  $10^{10}$   $Rh^{++}$  ions every 25 pulses. Data for each run,  $V_a = -4063$  and  $-2466$  volts, were obtained with the tip in vacuum ( $4 \times 10^{-9}$  Torr) and with the instrument's full acceptance angle apertured to  $5.4^\circ$ . The tip was at a temperature of  $78$  K, and each run yielded some 80 collected ions. Finally, particular care was taken to avoid collecting data during the increase in yield which accompanied the collapse of the 001 plane.

The conditions, equation (3.72), from which the enhancement factor is obtained may be fully expressed as

$$r_t \approx \text{constant}$$

and

$$V_{tb} + |V_a| + f V_{ep} = V \text{ (constant).} \quad (3.85)$$

In terms of the original definition of  $V_{DC}$ , equation (2.1), where  $V_{ep}$  was not included in  $V_{DC}$ , relation (3.85) may be written as

$$r_t \approx \text{constant}$$

and

$$V_{DC} + f V_{ep} = V \text{ (constant),} \quad (3.86)$$

where  $V$  is a constant at a fixed evaporation rate and  $V_{ep}$  is given by equation (2.34). The field enhancement factor is obtained from the slope,  $-f$ , of the straight line plot of  $V_{DC}$  against  $V_{ep}$  by means of equations (3.86).<sup>29</sup> The slopes of the two straight line least-squares fits<sup>67</sup> to the experimental rhodium data yielded:

$$f = 1.60 \pm 0.01 \quad \text{and} \quad f = 1.63 \pm 0.02, \quad (3.87)$$

where the error in each case is a standard deviation from the estimated value of  $f$ . This yields a value of  $0.6 V_{ep}$  for the pulse "overshoot",  $(f-1) V_{ep}$ , as indicated in the previous section.

The pulse factor may be determined iteratively from the same rhodium data by choosing values for  $\alpha_T^{(Rh^{++})}$  until one is found for which the difference,  $\Delta T$ , between the experimentally observed and calculated flight time is independent of the pulse fraction. Specifically, at a fixed field evaporation rate, the total potential,  $V$ , is constant, and  $\Delta T$  becomes independent of the pulse voltage,  $V_{ep}$ , when the correct value of  $\alpha_T^{(Rh^{++})}$  is obtained. The observed rhodium ion flight times,  $T_{EXP.}$  or  $T_{ob}$ , and those calculated from equation (3.23),  $T_{TH}$ , using the correct value, 1.15, for  $\alpha_T^{(Rh^{++})}$  are plotted against  $V_{ep}$  in Figure 13 (bottom). Here, the difference between  $T_{EXP}$  and  $T_{TH}$  is independent of  $V_{ep}$  to the extent that the root mean squared deviation about the mean difference ( $\bar{\Delta}T = 47.1 @ V_a = -4063V$  and  $\bar{\Delta}T = 20.4 @ V_a = -2466V$ ) for each run is 2.3 and 1.9 nanoseconds, respectively.

The iteration was done by varying  $\alpha_T^{(Rh^{++})}$  in 0.01 increments until the calculated lines were brought parallel to the observed lines as in Figure 13 (bottom). The slope of the calculated line changes sufficiently with the choice of pulse factor that the process is accurate and rapid. For example, an incorrect value of 1.00 for  $\alpha_T^{(Rh^{++})}$  yields a calculated line for the  $V_a = -4063V$  run which converges toward the observed line ( $\Delta T = 1.5 \text{ ns} @ V_{ep} = 1392V$ ) from an initial separation,  $\Delta T$ , of 36 ns at  $V_{ep} = 560V$ .

This method yields a value of  $\alpha_T$  specific to rhodium. That is,

$$\alpha_T^{(Rh^{++})} = 1.15 \pm 0.01. \quad (3.88)$$

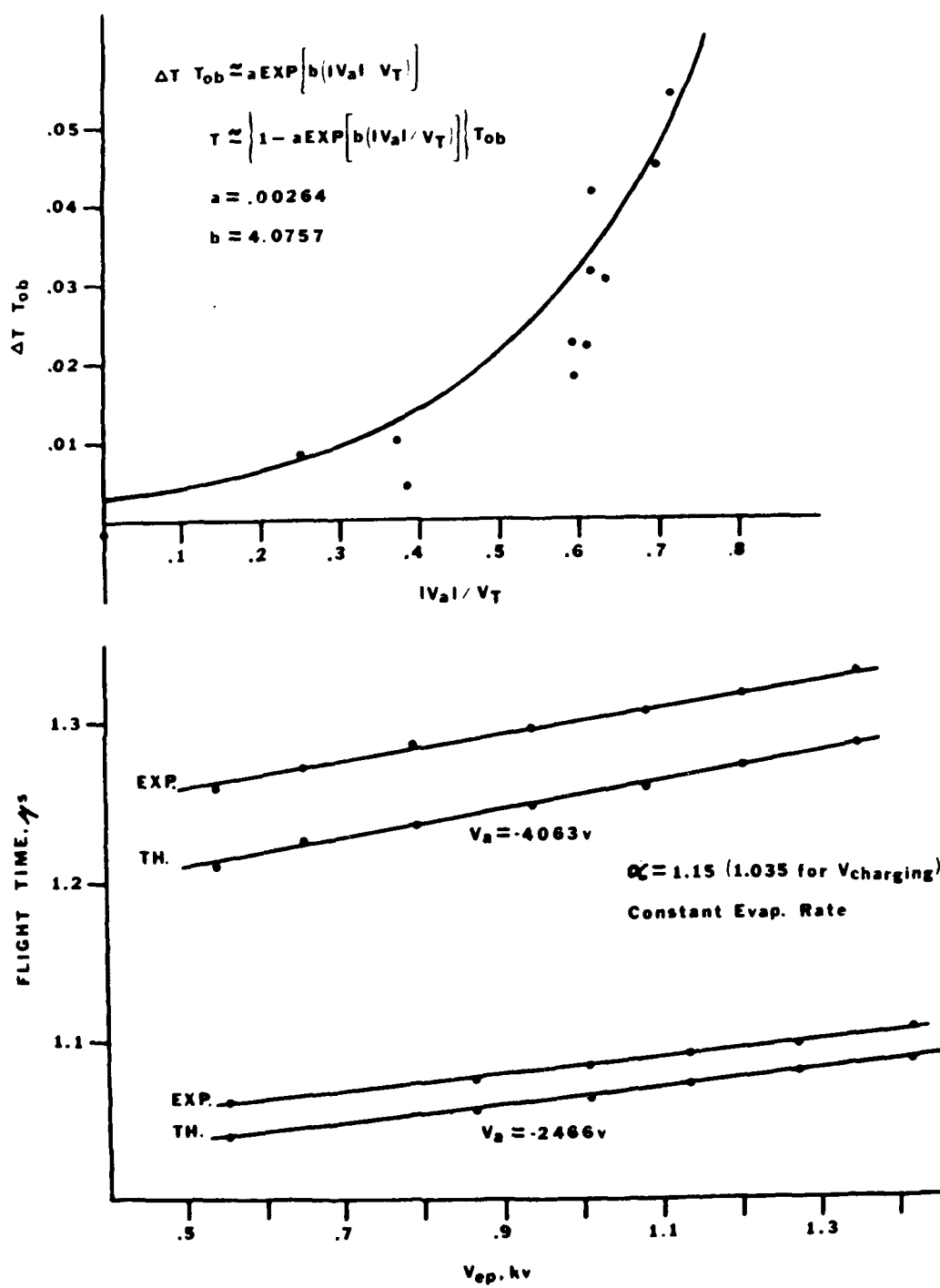


Figure 13. The instrument's calibration curves: (top) the empirical correction to the absolute flight equation, and (bottom) the pulse factor determined from rhodium data.

Should a more accurate calibration be necessary, the mass dependence of  $\alpha$  may be obtained by repeating this procedure for various other ionic species. In this work, the value obtained for  $\alpha_T$  ( $\text{Rh}^{++}$ ) was simply generalized with an appropriate estimate of the increased uncertainty, see Figure 12(a). That is:

$$\alpha \approx 1.15 \pm 0.06. \quad (3.89)$$

Although the difference,  $\Delta T = T_{\text{ob}} - T_{\text{TH}}$ , is independent of the pulse fraction when  $\alpha$  is chosen correctly, the difference remains dependent on the retarding fraction,  $|v_a|/v$ . Here,  $V$  is the total potential from equation (3.85). This dependence persists because the analytic form assumed for the retarding potential is not an exact representation of the electrostatic potential within the retarding region of the instrument except during free flight when both  $|v_a|$  and  $\Delta T$  are zero. This dependence is accounted for separately in the flight equation by an empirical function fitted to the totality of collected mass data. In other words, the fractional error in the observed flight time is some function of the retarding fraction. That is:

$$\frac{\Delta T}{T_{\text{ob}}} = f \left( \frac{|v_a|}{v} \right). \quad (3.90)$$

In view of the limited data and the uncertainty in  $\alpha$ , it is sufficient to approximate the retarding fraction by  $|v_a|/v_T$ , where  $v_T$  is given by equations (3.8) and (3.9). The data taken at various retarding fractions and an empirical function,

$$\frac{\Delta T}{T_{\text{ob}}} \approx a \exp \left[ b \left( \frac{|v_a|}{v_T} \right) \right], \quad (3.91)$$

fitted to it are shown in Figure 13 (top). The points in Figure 13 (top)

have relative statistical weights from 0.2 to a maximum of 5 depending on the fraction of data represented and the fractional uncertainty in the flight time difference,  $\Delta T$ . In all, the twelve sets of data indicated represent 53 individual points, and the root mean squared deviation of the  $\Delta T/T_{ob}$  data about the curve is 0.007. The values of the curve fit parameters  $a$  and  $b$  are 0.0026 and 4.07, respectively. If further data had been available a function of the form

$$\frac{\Delta T}{T_{ob}} \approx a \exp \left[ b \left( \frac{|v_a|}{v} \right)^x \right] \quad (3.92)$$

would have been used to obtain a more exact fit by varying  $x$  from 1 to about 2 to adjust the curvature of the function.

Equation (3.91) yields the empirically corrected flight time used in the final absolute flight equation. That is:

$$T \approx \left\{ 1 - a \exp \left[ b \left( \frac{|v_a|}{v_T} \right) \right] \right\} T_{ob} \quad (3.93)$$

where  $T_{ob}$ , the observed flight time, includes the instrumentation delay,  $\delta$ . Equation (3.24) with  $T$  given by equation (3.93) is the absolute flight equation for this instrument. The relative flight equation (2.12) remains unchanged provided  $\alpha$ 's mass dependence may be ignored. If required, a more accurate relative flight equation may be obtained by retaining the pulse factor. For example, a free flight drift region would yield a relative flight equation given as

$$\left( \frac{m}{n} \right)_x = \left( \frac{m}{n} \right)_o \left( \frac{v_{DC} + \alpha_x v_{ep}}{v_{DC} + \alpha_o v_{ep}} \right) \left( \frac{t_x}{t_o} \right)^2. \quad (3.94)$$

Here, the value of  $\alpha$  at each mass must be determined.

AD-A095 254

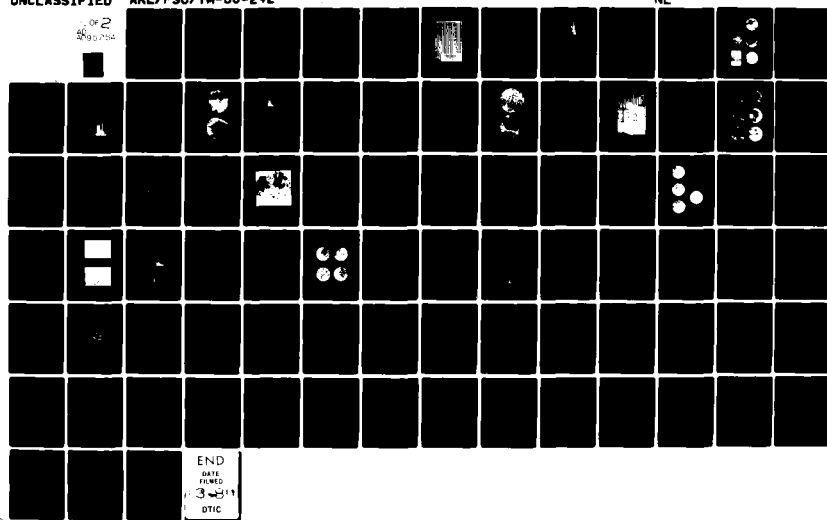
PENNSYLVANIA STATE UNIV. UNIVERSITY PARK APPLIED RESE--ETC F/6 11/6  
THE HIGH RESOLUTION IMAGING ATOM-PROBE WITH APPLICATION TO NICK--ETC(U)  
DEC 80 M MARTINKA  
ARL/PSU/TH-80-242

N00024-79-C-6043

NL

UNCLASSIFIED

1 of 2  
Signature



END  
DATE FILMED  
3-81  
DTIC

A summary of the spectral mass data collected with this instrument appears in Table 1. The first two sets of data in Table 1 summarize the rhodium calibration data, and the remaining entries correspond to mass spectra found in the last section of this chapter and in Chapter V. For each ionic species detected, both absolute and relative mass determinations and their errors relative to a reference value are listed in Table 1.

#### 4. Experimental Performance

The varied results presented in this section portray the nature and scope of the experimental information which may be obtained by imaging atom-probe mass spectrometry. They also reflect the instrument's performance and serve as reference for the applications involving rhodium and nickel presented in Chapter IV.

Figure 14 shows the oscilloscopic output of the instrument while apertured and at a background vacuum of  $2 \times 10^{-9}$  Torr. This data from a rhodium tip at 78 K was photographed just prior to acquiring the second set of calibration data given in Table 1. The DC evaporation voltage was 6.3 kV and the retarder fraction during pulsing was 0.5884. The oscilloscope was set for a vertical sensitivity of 50 mV per major division and at a sweep rate of 20 ns per major division. Each signal is caused by the arrival of a single rhodium ion, and the observed flight time (e.g., 1268 ns) is the delay setting plus the instrumentation delay, 1240 ns, added to the time interval remaining on the oscilloscopic photograph, 28 ns. The oscilloscopic intervals are measured from the trailing edge of the fiducial mark to the sharp leading edge of each mass signal. The observed flight time is then entered into the flight

Table 1: Calculated mass-to-charge ratios for various materials field evaporated in vacuum.

Histogram Figure No.	Observed Ionic Species	m/n Reference Value	m/n Calculated from Flight Times	Error	Retarder Fraction	Observed Flight Time	
		(amu)	Relative (amu)	Absolute (amu)	Rel. (%)	$ V_a /V_T$	$T_{ob}$ (ns)
13. (bottom) Pulse factor calibration data	$^{103}\text{Rh}^{++}$	51.452400	50.84	50.84	1.3	0.3750	1064.0
			50.63	50.63	1.6	0.3818	1076.0
			50.89	50.89	1.1	0.3854	1086.0
			50.50	50.50	1.9	0.3893	1090.0
			50.40	50.40	2.0	0.3927	1096.0
			50.78	50.78	1.3	0.3956	1106.0
			50.95	50.95	1.0	0.5918	1258.0
			50.56	50.56	1.7	0.5993	1270.0
			50.91	50.91	1.1	0.6044	1286.0
			50.77	50.77	1.3	0.6086	1294.0
			50.68	50.68	1.5	0.6134	1304.0
			50.38	50.38	2.1	0.6201	1316.0
			50.42	50.42	2.0	0.6249	1328.0
15. (bottom)	$^{103}\text{Rh}^{++}$ $\text{RhH}_2^{++}$ $\text{RhH}_2^{++}$	51.452400 51.956313 52.460225	51.22 51.79 52.27	51.22 51.79 52.27	0.5 0.3 0.4	0.3726	1075.0 1081.0 1086.0
15. (top)	$^{103}\text{Rh}^{++}$ $\text{RhH}_3^{++}$	51.452400 52.964138	52.29 53.85	52.29 53.85	-1.6 -1.7	0.6211	1016.0 1031.0

Table 1. (cont.)

Histogram	Observed Ionic Species	m/n Reference <sup>†</sup>	m/n Calculated from Flight Times	Error	Retarder Fraction	Observed Flight Time	
Figure No.		Value	Relative (amu)	Abs. (amu)	Rel. (%)	V <sub>a</sub>  /V <sub>T</sub>	T <sub>ob</sub> (ns)
—	<sup>182</sup> W <sup>++</sup>	60.649423	60.12	0.9	Free	1170.0	
	<sup>183</sup> W <sup>++</sup>	60.983430	60.48	-0.05	Flight	1173.5	
	<sup>184</sup> W <sup>++</sup>	61.316997	60.79	-0.01	0.9	1176.5	
	<sup>186</sup> W <sup>++</sup>	61.984780	61.51	-0.12	0.8	1183.5	
17.	<sup>182</sup> W <sup>++</sup>	60.649423	61.12	-0.8	0.7208	1837.0	
	<sup>183</sup> W <sup>++</sup>	60.983430	61.45	0.01	-0.8	1842.0	
	<sup>184</sup> W <sup>++</sup>	61.316997	61.79	0.01	-0.8	1847.0	
	<sup>186</sup> W <sup>++</sup>	61.984780	62.46	0.01	-0.8	1857.0	
19. (bottom)	<sup>58</sup> Ni <sup>++</sup>	28.967671	28.84	0.4	0.70077	916.0	
Dark	<sup>58</sup> NiH <sup>++</sup>	29.471584	29.35	-0.03	0.4	924.0	
	<sup>60</sup> Ni <sup>++</sup>	29.965392	29.86	-0.08	0.4	932.0	
	<sup>62</sup> Ni <sup>++</sup>	30.964173	30.89	-0.20	0.2	948.0	
	<sup>64</sup> Ni <sup>++</sup>	31.963980	31.88	-0.17	0.3	963.0	
	<sup>64</sup> NiH <sup>++</sup>	32.467892	32.34	-0.05	0.4	970.0	
	<sup>64</sup> NiH <sub>2</sub> <sup>++</sup>	32.971805	32.81	0.05	0.5	977.0	
19. (bottom)	<sup>58</sup> Ni <sup>++</sup>	28.967671	29.00	-0.1	0.2499	870.0	
Light	<sup>58</sup> NiH <sup>++</sup>	29.471584	29.54	-0.11	-0.2	878.0	
	<sup>60</sup> Ni <sup>++</sup>	29.965392	30.01	-0.03	-0.2	885.0	
	<sup>62</sup> Ni <sup>++</sup>	30.964173	31.04	-0.12	-0.3	900.0	
	<sup>64</sup> Ni <sup>++</sup>	31.963980	31.97	32.01	-0.03	914.0	
	<sup>64</sup> NiH <sup>++</sup>	32.467892	32.86	-1.08	-1.2	926.0	
	<sup>64</sup> NiH <sub>2</sub> <sup>++</sup>	32.971805	33.28	-0.82	-0.9	932.0	

Table 1. (cont.)

Histogram Figure No.	Observed Ionic Species	m/n Reference <sup>†</sup> Value	Relative (amu)	Absolute (amu)	Rel. (%)	Abs. (%)	Error  v <sub>a</sub>  /v <sub>T</sub>	Retarder Fraction	Observed Flight Time T <sub>ob</sub> (ns)
19. (top)	<sup>58</sup> Ni <sup>++</sup> <sup>60</sup> Ni <sup>++</sup> <sup>62</sup> Ni <sup>++</sup> <sup>62</sup> NiH <sup>++</sup> , <sup>60</sup> NiH <sub>3</sub> <sup>++</sup>	28.967671 29.965392 30.964173 31.468086	29.92 30.97 31.50	28.88 29.83 30.87 31.40	0.3 0.15 -0.01 -0.09	0.3 0.5 0.3 0.2	0.6162	796.0 809.0 823.0 830.0	
26. Nickel Plate	<sup>1</sup> H <sup>+</sup> <sup>20</sup> Ne <sup>+</sup> <sup>58</sup> Ni <sup>++</sup> <sup>58</sup> NiH <sub>2</sub> <sup>+</sup>	1.007825 19.992440 28.967671 59.950992	1.01 19.77 28.32 58.65	0.99 19.33 28.32 58.65	-0.02 1.12 2.2 -0.06	1.8 3.3 2.2 2.2	0.5960	140.0 620.0 750.5 1080.0	
29. Ni-P Plate	<sup>1</sup> H <sup>+</sup> <sup>20</sup> Ne <sup>++</sup> <sup>31</sup> P <sup>+</sup> <sup>20</sup> Ne <sup>+</sup> <sup>58</sup> Ni <sup>++</sup> <sup>60</sup> Ni <sup>++</sup> <sup>62</sup> Ni <sup>++</sup> <sup>16</sup> O <sup>+</sup> <sup>58</sup> NiH <sub>2</sub> <sup>+</sup>	1.007825 9.996220 15.486882 19.992440 28.967671 29.965392 30.964173 31.989830 59.950992	1.03 10.07 15.49 19.74 28.46 29.93 30.98 32.05 59.96	1.01 9.90 15.22 19.40 28.46 29.41 30.44 31.49 58.91	-2.32 -0.75 0.01 1.27 1.75 0.11 -0.06 -0.19 -0.01	-0.22 0.96 1.72 2.96 1.75 1.85 1.69 1.56 1.74	0.5914	160.0 500.0 620.0 700.0 848.0 862.0 877.0 892.0 1220.0	

Table 1. (cont.)

Histogram Figure No.	Observed Ionic Species	m/n Reference Value	m/n Calculated from Flight Times	Error	Retarder Fraction	Observed Flight Time	
		(amu)	Relative (amu)	Rel. (amu)	Abs. (%)	$ v_a /v_T$	$T_{ob}$ (ns)
31. Ni-P Annealed Plate	$^1H^+$	1.007825	1.08	1.05	-7.67	-4.18	0.63337
	$^2_0Ne^{++}$	9.996220	10.32	10.02	-3.20	-0.24	444.0
	$^3_1P^{++}$	15.486882	15.49	15.05	0.00	2.82	544.0
	$^2_0Ne^+$	19.992440	19.73	19.17	1.32	4.11	614.0
	$^{58}Ni^{++}$	28.967671	28.15	28.15	2.82		744.0

<sup>†</sup>J. Roboz, "Introduction to Mass Spectrometry," John Wiley and Sons, New York (1968), pp. 503-510.

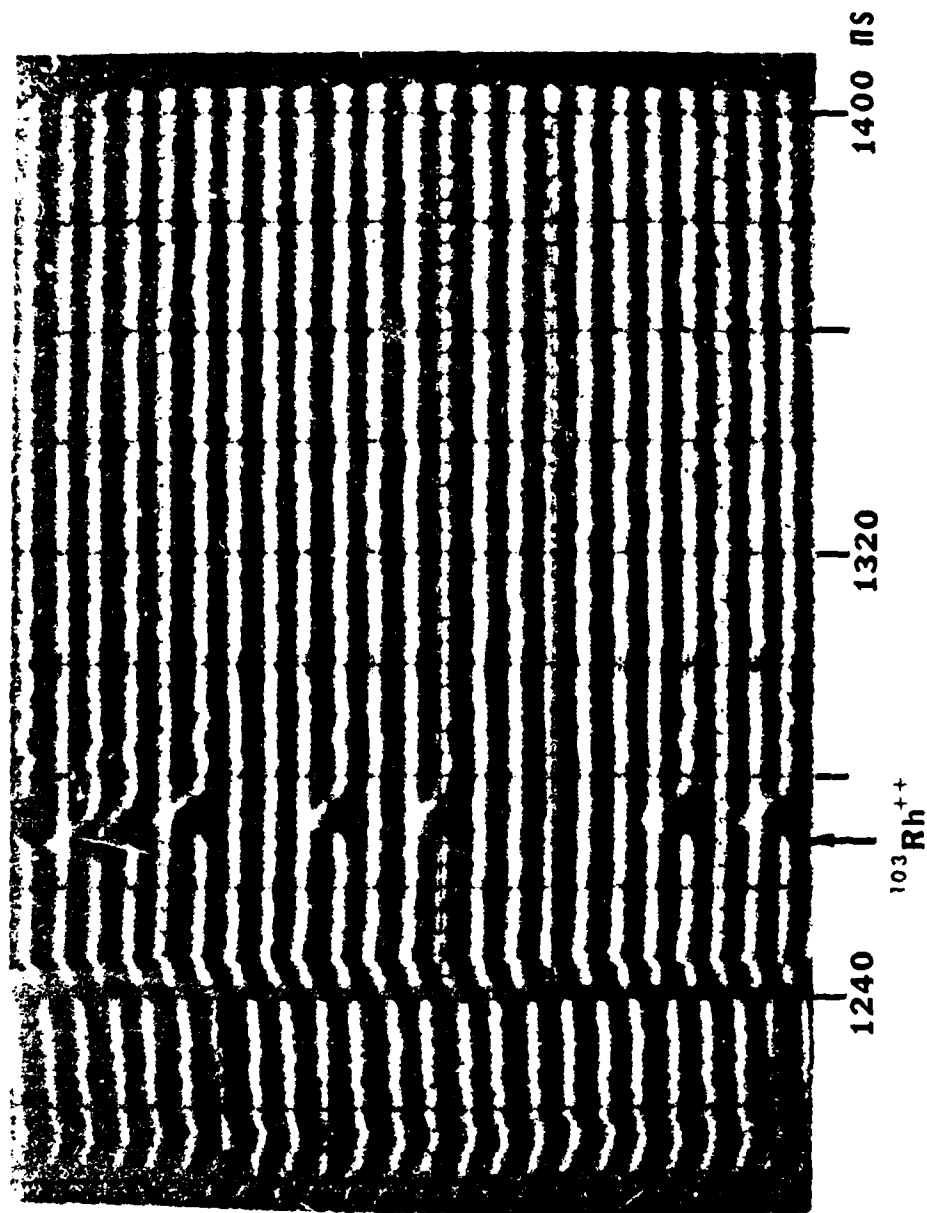


Figure 14. Oscilloscopic time signals from a rhodium tip pulse evaporated in vacuum.

equation as in the previous section in order to determine the mass-to-charge ratio.

A histogram of 180 pulse evaporated ions was obtained from the rhodium sample prior to its use in the calibration sequence and is shown in Figure 15 (bottom). The rhodium tip was at a temperature of 78 K in a background pressure of  $4 \times 10^{-9}$  Torr, and the instrument was apertured to an acceptance angle of 5.4 degrees. The ions were pulse field evaporated at an average rate of one ion every 4 pulses. The observed flight time obtained for the leading edge of the spectral line for each detected species and the corresponding mass-to-charge ratio are given in Table 1.

The full width of the  $\text{Rh}^{++}$  line at 10 and 50% of the peak's total height is 5 and 2 nanoseconds, respectively. For a total flight time of 1075 ns, this represents time resolutions of  $t/\Delta t$  (10%) = 215 and  $t/\Delta t$  (50%) = 538, and mass resolutions of  $m/\Delta m$  (10%) = 100 and  $m/\Delta m$  (50%) = 270. Here, a full peak width at 10% of peak height represents the instrument's resolution at low abundances in concurrence with the approach taken by S. V. Krishnaswamy.<sup>27</sup> It would be inappropriate to define the instrument's resolution from a 10% valley between peaks one amu apart<sup>68</sup> since the peaks from electrically pulsed atom-probes are asymmetric. As with mass spectrometers using sputter ion sources,<sup>68</sup> atom-probes exhibit "tailing" toward higher masses due to an initial energy spread. For atom-probes, this "tailing" causes sufficient asymmetry below 10 to 20% of peak height that a "percent valley" is not an equivalent of the full peak width definition.

A reproducible procedure for comparing the resolution of various atom-probes would be to compare the full width resolution at a fixed

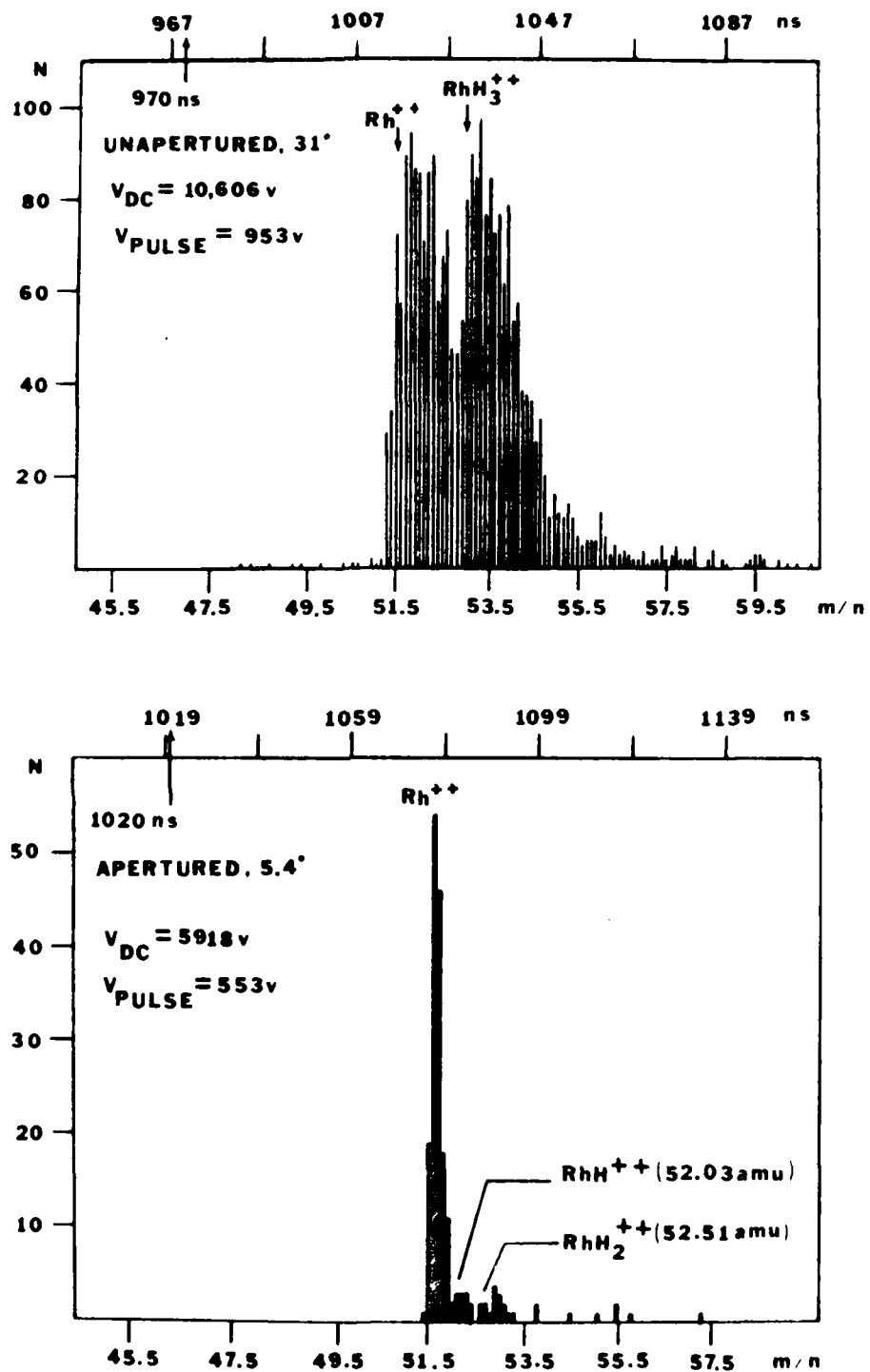


Figure 15. Histograms of  $^{101}\text{Rh}^{++}$  time signals from a rhodium tip evaporated in vacuum.

percentage of the height of a smooth peak obtained from a histogram of a large number of collected, singly isotopic ions. Coping with the increased data would be facilitated by the use of a desktop computer. For example, such a smoothing as conducted with the moderate number of ions collected for the histogram in Figure 15 (bottom) yields a mass resolution at half-height,  $m/\Delta m$  (50%), of 150. The smoothing about each time interval was done by considering one interval, 1 ns, before and after with all intervals weighted equally and the results normalized to the total number of detected ions, 180. In addition, this procedure yielded a more recognizable line shape which in the future may aid in separating closely spaced spectral lines for improved low abundance sensitivity.

Figure 15 (top) shows a histogram of 2450 ions collected from a rhodium tip at 78K in a background pressure of  $3 \times 10^{-9}$  Torr. The ions were evaporated at an average rate of one to two ions every pulse, and the data was collected at the instrument's full acceptance angle of 31 degrees. The observed flight times for the leading edges of the  $Rh^{++}$  and  $RhH_3^{++}$  spectral lines and their calculated mass-to-charge ratios are given in Table 1.

The full width at half-height of the spectral lines in Figure 15 (top) show a mass resolution of 50. This decrease in resolution at full acceptance angle is most probably due to a combination of two effects. Firstly, there is an increase in the number of ions prematurely evaporating at lower pulse potentials causing greater "tail-ing". These ions are those whose metal-metal bonds have been weakened by adsorbed residual hydrogen. Such an ion arrives later in time since it has not received its full initial kinetic energy. The increase in

prematurely evaporated ions can be attributed to the greater role of adsorbed hydrogen in full acceptance angle spectra. That is, at full angle, the sampled area of the tip surface is 30 times larger than that viewed in the apertured mode. Further, it is shown in Section 1 of Chapter IV that the 001 plane of Rh sampled for the apertured mode histogram given in Figure 15 (bottom) shows far less field adsorption of hydrogen than other crystallographic regions of rhodium specimens. Secondly, off-axis ions may incur longer flight times if the correction of spherically projected ions for coincident arrival at a flat detector given in Section 6 of Chapter II is incomplete.

Fortunately, those species which are resolved may be accurately identified since the leading edge of the spectral lines remains "sharp".

Further improvements in full acceptance angle resolution will be pursued with A. J. Melmed at the National Bureau of Standards. There, an instrument will be constructed with spherical detectors and a base pressure of  $10^{-11}$  Torr. It will provide sample manipulation for the comparison of residual gas adsorption effects at apertured and full acceptance angles along various crystallographic directions.

Figure 16 depicts the variety of atomically resolved displays of an 011 oriented tungsten surface obtained by imaging atom-probe mass spectrometry and their synchronization with time-of-flight spectra. The sample was at a temperature of 78 K and its surface was imaged with helium at a pressure of  $5 \times 10^{-6}$  Torr at a best image potential of 7 kV, Figure 16(c). The remaining displays, 16(b) and 16(d) through 16(f), are self-images of the sample in vacuum,  $7 \times 10^{-9}$  Torr, obtained by field evaporating the surface. Figure 16(b) is a photograph at f/1.4 of a single pulse evaporation, and Figure 16(d) is a photographic

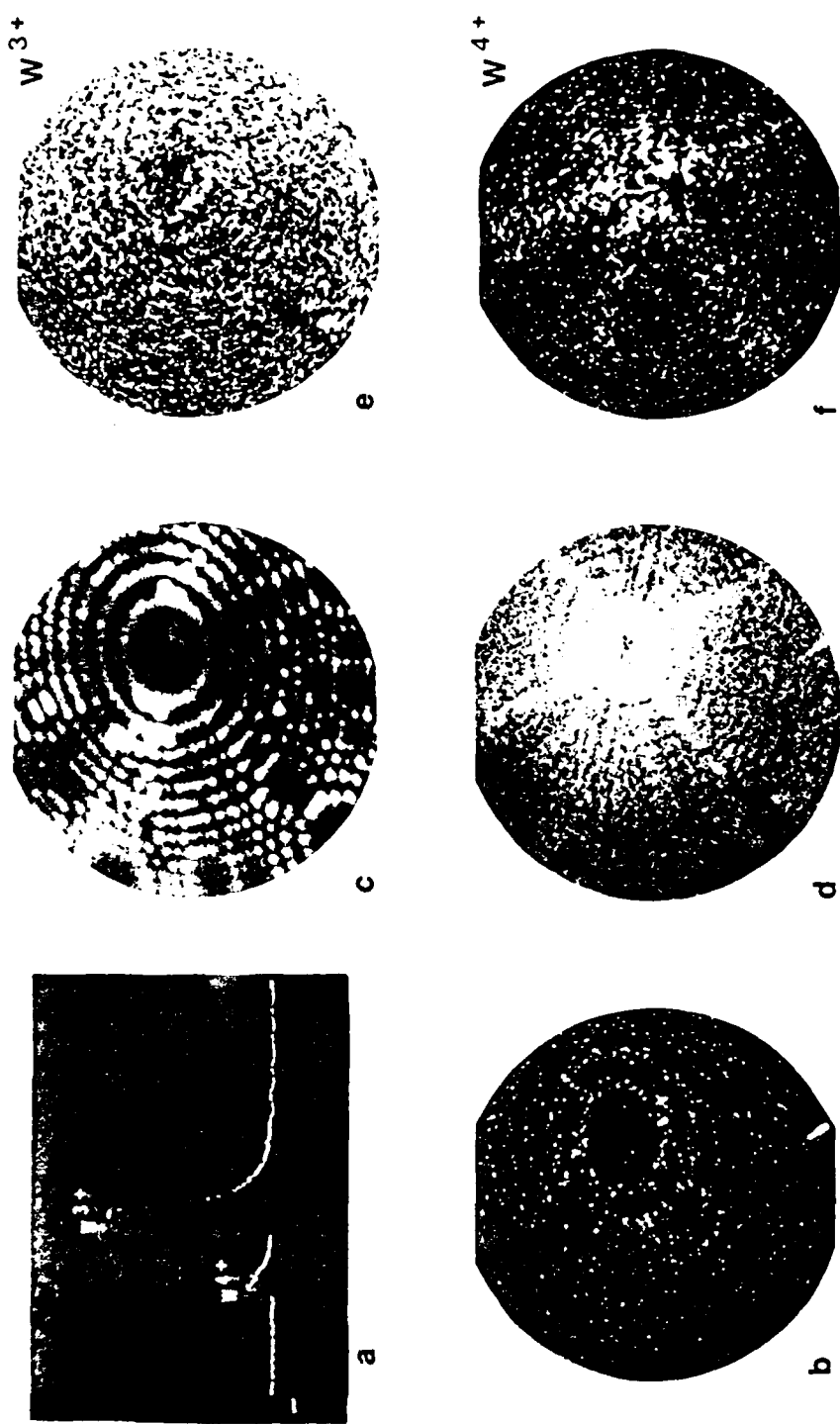


Figure 16. Full characterization of a 011 oriented tungsten tip: (a) an oscilloscopic trace of the prominent charge state, (b) a single-pulse evaporation pattern, (c) a helium ion image (d) a multilayer DC evaporation pattern, and (e,f) surface distributions of the two charge states.

integration at f/5.6 (the detector was at reduced gain) of the DC evaporation of 40 atomic layers. The evaporation potential at the end of the multilayer sequence was 9.5 kV. Figures 16(b) and 16(d) are not gated and contain image points resulting from the arrival of both  $W^{3+}$  and  $W^{4+}$  ions; whereas, Figures 16(e) and 16(f) are obtained by gating the detector on only during the arrival of either  $W^{3+}$  or  $W^{4+}$ , respectively. The cumulative photographs at f/1.4 of 100, Figure 16(e), and 50, Figure 16(f), single-pulse evaporation were taken with tip bias and pulse potentials of 9.3 kV, 0.9 kV and 7.7 kV, 0.77 kV, respectively. The number of layers evaporated from Figures 16(e) and 16(f) were about equal, with the evaporation rate for Figure 16(f) being approximately twice that for Figure 16(e). The relative abundance of  $W^{3+}$  and  $W^{4+}$  at a given rate is shown qualitatively in the oscilloscopic trace of Figure 16(a). Here, the sweep rate was 100 ns per major division, and the gated images, 16(e) and 16(f), were obtained by synchronizing the detector "on-time" with the desired mass peak. This was done by positioning the negative fiducial mark which appears at the beginning of the trace in Figure 16(a).

Figures 16(e) and 16(f) indicate that protruding plane edge atoms are the primary source of  $W^{3+}$  ions, while the lower abundance  $W^{4+}$  ions originate with higher probability along the [100] and [111] zones and about the 011 plane during its collapse. This agrees with imaging atom-probe observations by J. A. Panitz<sup>7,9</sup> and A. R. Waugh et al.<sup>14</sup> and with those obtained by S. V. Krishnaswamy et al<sup>13</sup> with the energy corrected atom-probe. The increase in abundance of  $W^{4+}$  during a 011 plane collapse indicates that the last atoms, which evaporate at higher field and rate, evaporate predominantly as  $W^{4+}$ . The increase in

abundance of higher charged ions at increased fields and evaporation rates has been discussed in papers by E. W. Müller and S. V. Krishnaswamy<sup>69</sup> and S. V. Krishnaswamy and S. B. McLane.<sup>70</sup> Finally, at the lower evaporation rates accessible with magnetic sector atom-probes, no charge state higher than  $W^{3+}$  has been observed for tungsten<sup>71</sup>.

Resolving the isotopes of tungsten, as in the histogram shown in Figure 17, provides a practical demonstration of the instrument's resolution when apertured to an acceptance angle of 5.4 degrees. Here, a total of 210  $W^{3+}$  ions were collected at a rate of one ion every four pulses from a tungsten tip at 78K in vacuum,  $2 \times 10^{-9}$  Torr. After smoothing the data in this histogram, a spectrum was obtained which exhibited a mass resolution of 200 and 100 at about a 50% and 10% valley, respectively. The smoothing about each time interval was done by considering at a weight of 25% the interval, 1 ns, before and after and normalizing the results to the total number of ions collected. The approximate relative abundance of each isotopic species was obtained by considering the number of ions in each spectral line, leading edge to leading edge. This yields 21%  $^{182}W$ , 14%  $^{183}W$ , 26%  $^{184}W$ , and 38%  $^{186}W$ , whereas reference values<sup>68</sup> are 26.41, 14.4, 30.64, and 28.41 percent, respectively. Considering the low number of ions collected and the "tailing" of the spectral lines, the agreement is reasonable. Finally, the calculated mass-to-charge ratios, observed flight times, and the retarder fraction for this data are given in Table 1. In addition, tungsten data of comparable resolution obtained under free-flight conditions is summarized in Table 1 for comparison.

The following results for pure nickel were obtained to aid, by comparison, in the interpretation of the nickel electro- and electroless

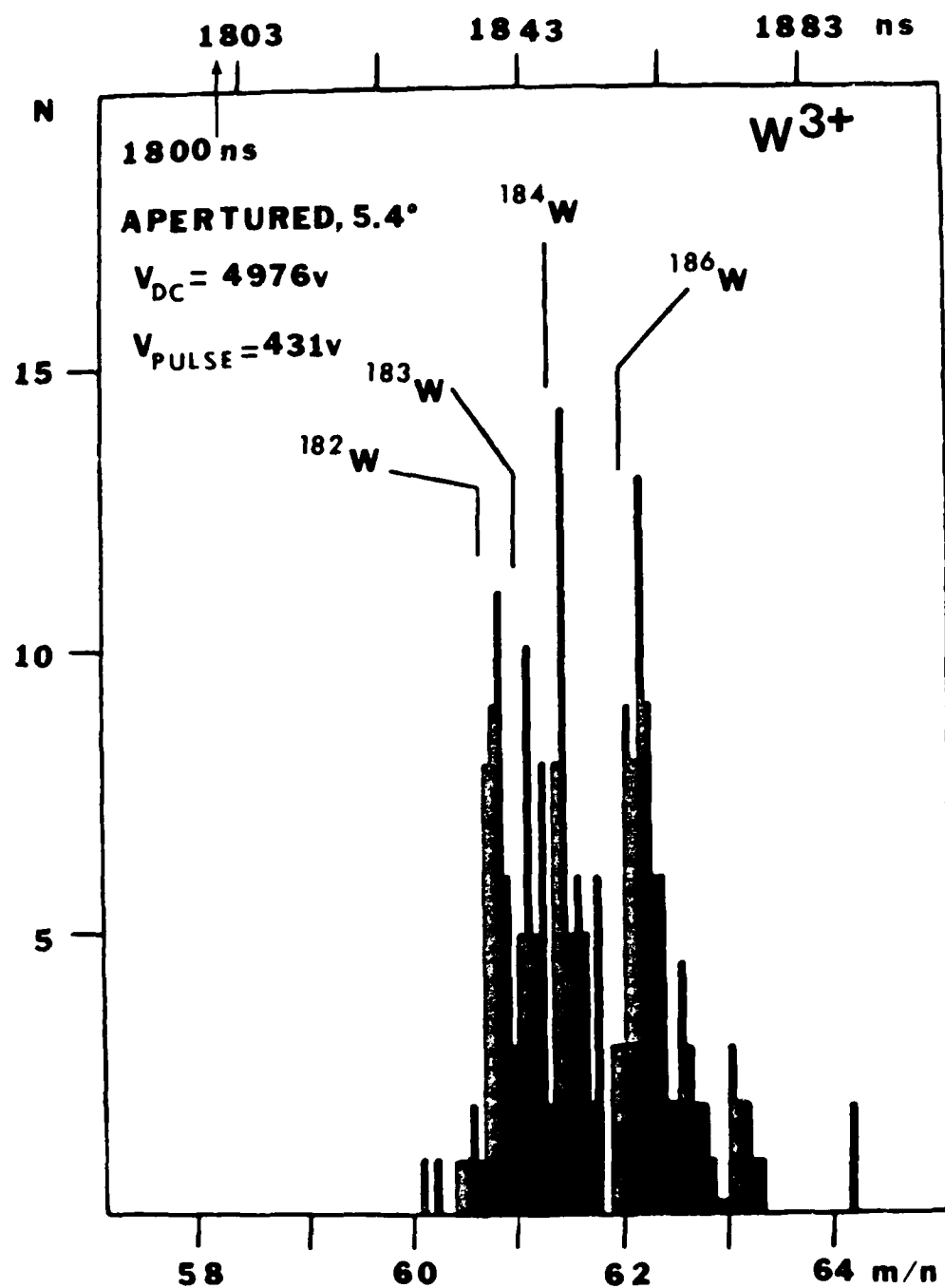


Figure 17. Histogram showing isotopic relative abundances of  $W^{3+}$  evaporated in vacuum.

plating results presented in Section 2 of Chapter IV. They further demonstrate the instrument's performance with regard to imaging and identification by time-of-flight mass spectrometry. In particular, the mass spectra indicate the prominent role of residual hydrogen and the accuracy and consistency with which species may be identified.

Figure 18(a) shows the surface of a 111 oriented pure nickel tip at 78K as imaged with neon at a pressure of  $5 \times 10^{-6}$  Torr. The best neon image potential was 8kV and DC evaporation in vacuum, background pressure was  $3 \times 10^{-9}$  Torr, began at a potential of 9 kV. A 20-layer DC evaporation pattern of this sample taken at an evaporation potential of 11 kV is shown in Figure 18(b) and is similar to those observed for fcc materials,<sup>31</sup> e.g., Pt and Ir. Prior to obtaining this multilayer pattern, a 200 evaporation pulse pattern gated for  $\text{Ni}^{++}$  (predominant charge state) was taken and showed features similar to those in Figure 18(b) but less distinctly.

Time-of-flight mass spectra at full and apertured acceptance angles were obtained from a pure nickel tip at a temperature of 78 K and at a background pressure of  $2 \times 10^{-9}$  Torr. The predominant residual gas adsorbed onto the sample surface from the background was hydrogen. Its presence is confirmed by the desorbed  $\text{H}^+$  ions which appear in the mass spectra during pulse evaporation. Nickel pulse field evaporates in vacuum predominantly as  $\text{Ni}^{++}$ , and Figures 19 (top) and 19 (bottom) show histograms of  $\text{Ni}^{++}$  ions obtained at full and apertured acceptance angles. The mass-to-charge ratio of each species calculated from the data presented in Figures 19 (top) and 19 (bottom), their respective observed flight time, and the retarding fraction employed are summarized in Table 1. Finally, in order to demonstrate the accuracy (both relative and

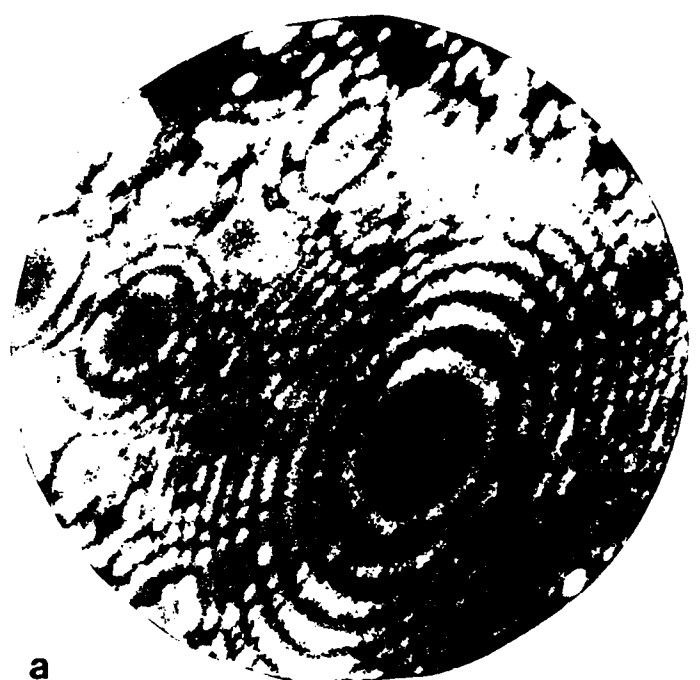
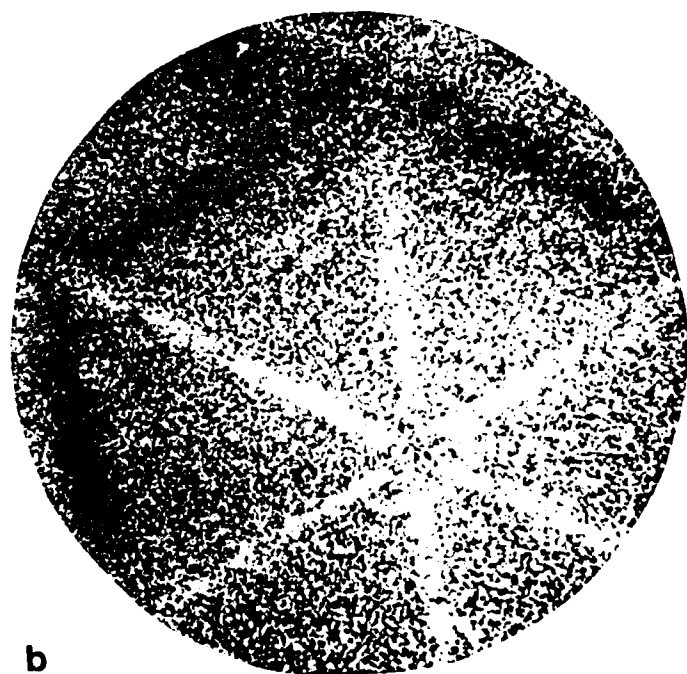
**a****b**

Figure 18. A 111 oriented nickel tip imaged (a) with Ne and (b) by multilayer DC evaporation in vacuum.

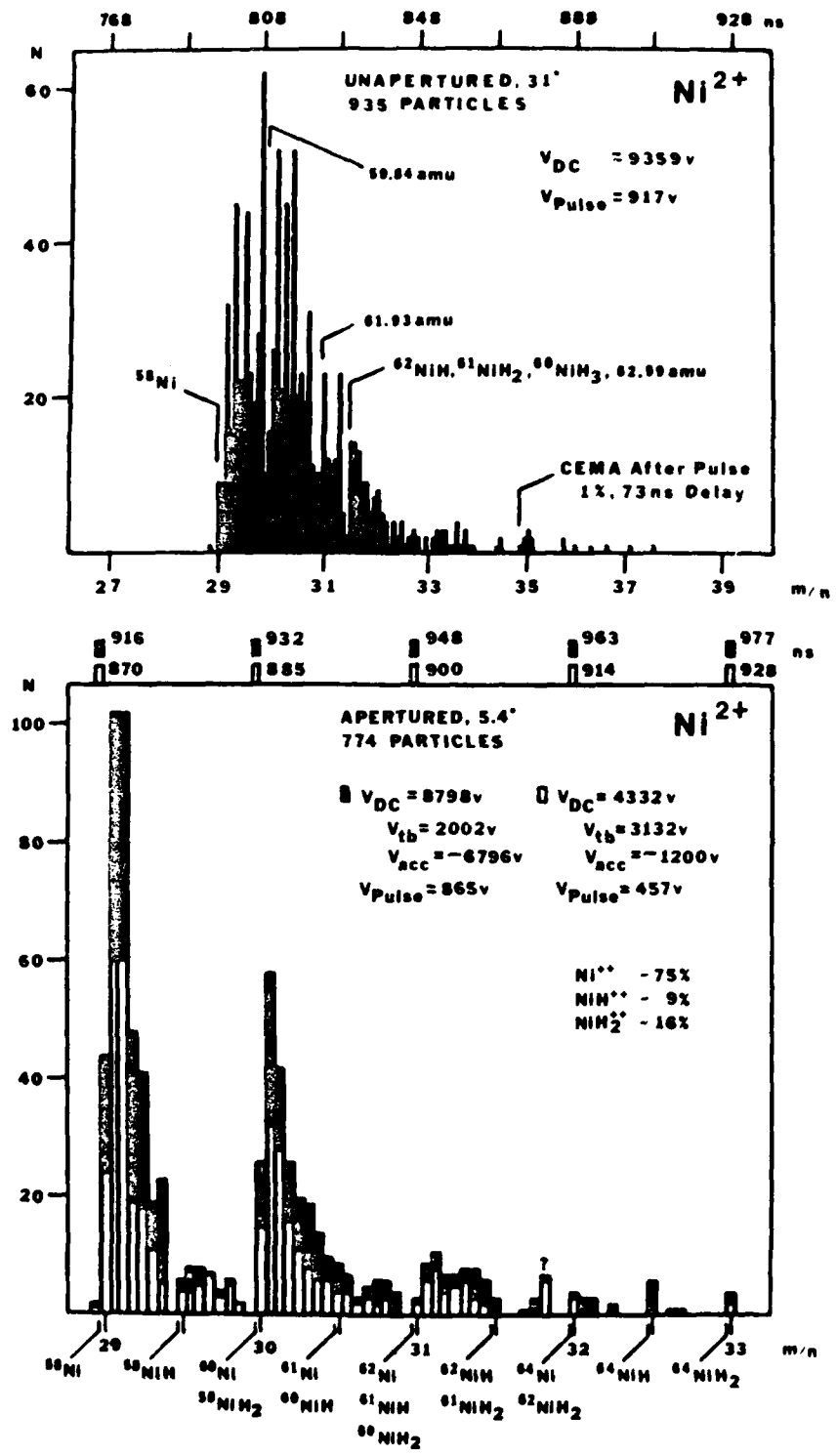


Figure 19. Histograms of  $Ni^{++}$  indicating the presence and relative abundances of nickel hydrides during evaporation in vacuum.

absolute given in Table 1) and consistency of the instrument, the data shown in Figure 19 (bottom) was obtained at both large (dark) and small (light) tip radii and retarding fractions.

The histogram in Figure 19 (bottom) shows the relative abundance of the nickel hydrides which results from the adsorption of residual hydrogen. The relative percentages, 75%  $\text{Ni}^{++}$ , 9%  $\text{NiH}^{++}$ , and 16%  $\text{NiH}_2^{++}$ , are calculated in the manner employed by S. Kapur and E. W. Müller.<sup>72</sup> That is, equations may be written for the percentage,  $I_n$ , of ions observed in each spectral line in terms of the percentages (x, y, and z) of  $\text{Ni}^{++}$ ,  $\text{NiH}^{++}$ , and  $\text{NiH}_2^{++}$ , respectively, and the known isotopic abundances of nickel. For example, with the known abundance<sup>68</sup> of 67.88% for  $^{58}\text{Ni}$  and  $I_1 = 49.3\%$  for the percentage of ions observed between 29 and 29.5 amu, an equation of the form

$$I_1 = 0.6788x \quad (3.95)$$

yields  $x = 73\%$  as the percent of  $\text{Ni}^{++}$ . Such equations in conjunction with the normalization condition,

$$x + y + z = 1 \quad (3.96)$$

yielded the approximate percentages of  $\text{Ni}^{++}$ ,  $\text{NiH}^{++}$ , and  $\text{NiH}_2^{++}$  given earlier. These results agree qualitatively with those (90%  $\text{Ni}^{++}$ , 1%  $\text{NiH}^{++}$ , and 9%  $\text{NiH}_2^{++}$ ) obtained with a highly apertured, energy corrected atom-probe by S. V. Krishnaswamy and E. W. Müller.<sup>73</sup>

Absorbed hydrogen appears to play a more prominent role in the histogram obtained from nickel at a full acceptance angle of 31 degrees, Figure 19 (top). Here, 30 times more surface area was sampled, but the field evaporation rate had to be reduced so that oscilloscopic photographs would remain decipherable. While species identification remained accurate, Table 1, the resolution was now insufficient for quantitative

estimates of hydride abundance. However, a qualitative shift in relative abundance is evident and indicates a larger percentage of nickel hydride. This probably results from two effects. First, at the lower evaporation field, a larger fraction of the detected ions will have originated from regions where hydrogen has weakened metal-metal bonds; and, second, the contributions from any preferred adsorption regions (as shown for rhodium in Chapter IV) would now be included in the spectra.

Finally, the histogram in Figure 19 (top) included detector after-pulses such as those discussed in Section 5 of Chapter II. After-pulses are common to secondary electron multipliers,<sup>74</sup> and their treatment in atom-probe mass spectrometry has been discussed by E. W. Müller, S. V. Krishnaswamy, and S. B. McLane.<sup>60</sup> Since such artifact signals require precursor mass signals and occur at a fixed time gap, they may be identified and discriminated against.

## IV. APPLICATIONS

1. Surface Distribution of Field Adsorbed Hydrogen

The adsorption of hydrogen onto a rhodium surface was investigated by using the imaging atom-probe as a purely surface sensitive tool. That is, this work was conducted in a manner which preserved the original surface (as observed at atomic resolution by field-ion microscopy) during the adsorption and subsequent desorption of hydrogen. This was verified frequently by observing the time-of-flight spectra which showed no rhodium species evaporating with the desorbing hydrogen. Such a situation prevailed except at the heaviest hydrogen coverage where slight evaporation of the rhodium substrate was unavoidable. Hydrogen was supplied to the rhodium surface from the gas phase at rates determined by its field ionization probability in the applied electric field, and, simultaneously, pulse desorbed at regular intervals so that only a small amount was present on the surface at any given time. The adsorbed hydrogen distributions over the undisturbed rhodium surface were obtained by gated pulse desorption for  $H^+$ , and displayed detailed correlation to both the crystallographic and atomic structure of the rhodium surface.

The rhodium surface was prepared by DC field evaporation in vacuum, background pressure was  $2 \times 10^{-9}$  Torr, and Figure 20(b) shows a 20-layer evaporation pattern of the 001 oriented sample. Subsequently, a field-ion micrograph of the surface was taken with neon at a pressure of  $5 \times 10^{-6}$  Torr, Figure 20(a). Evaporation in vacuum was observed at 7.8 kV, and the best neon image potential was 6.6 kV. With tip bias set sufficiently high to spatially ionize hydrogen,  $H_2$  gas was admitted

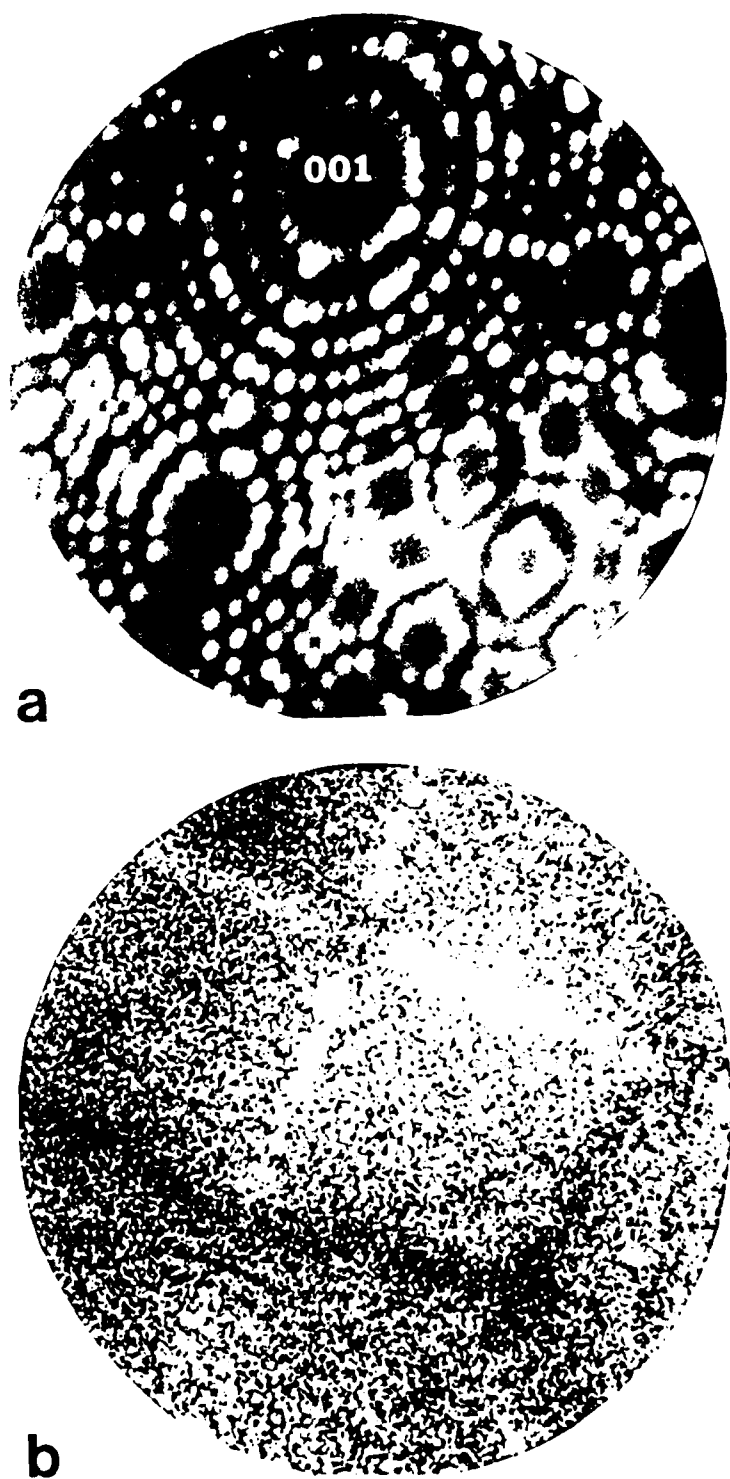


Figure 20. A 001 oriented rhodium tip imaged (a) with Ne and (b) by multilayer field evaporation in vacuum.

until a pressure of  $1 \times 10^{-8}$  Torr was maintained after saturation of the titanium getter. The tip bias was then reduced so as to require either a 10 or 20% pulse fraction, and the pulse potential was then increased until evaporation of hydrogen alone was observed. This pulse evaporation was then continued at regular intervals.

To further preclude the evaporation of the rhodium substrate, the "overshoot" (ringing) of the high voltage evaporation pulse was suppressed by a 47-ohm damping resistor. This reduced the pulse factor, which was used in the flight equations, to a value of one, and slightly increased the spread in the  $H^+$  mass signals to 4 ns. Unfortunately, the negatives of the representative mass traces obtained at a sweep rate of 20 ns per division were slightly underdeveloped, and did not have sufficient contrast for quality prints. However, comparable data was retaken at a later date from a similar 001 oriented rhodium sample in the presence of  $1 \times 10^{-8}$  Torr of hydrogen, and it is presented in Figure 21. Here, the sweep rate is 50 ns per division, and both the hydrogen mass signals and the time marks can be clearly seen. This data is similar to the prior traces, but exhibits a slightly narrower spread.

A mass-to-charge ratio of 1.06 was calculated ( $\alpha=1$ ) from the well defined leading edge of the spectral line obtained from the hydrogen signals in the original 20 ns/div. traces. This is 5.6% heavier than the reference value for  $H^+$  of 1.007825, and similar extended flight times also occurred in undamped ( $\alpha=1.15$ ) desorption of hydrogen from rhodium and nickel platings, Table 1. This may be the result of a dissociation at a well defined distance from the emitter surface. For

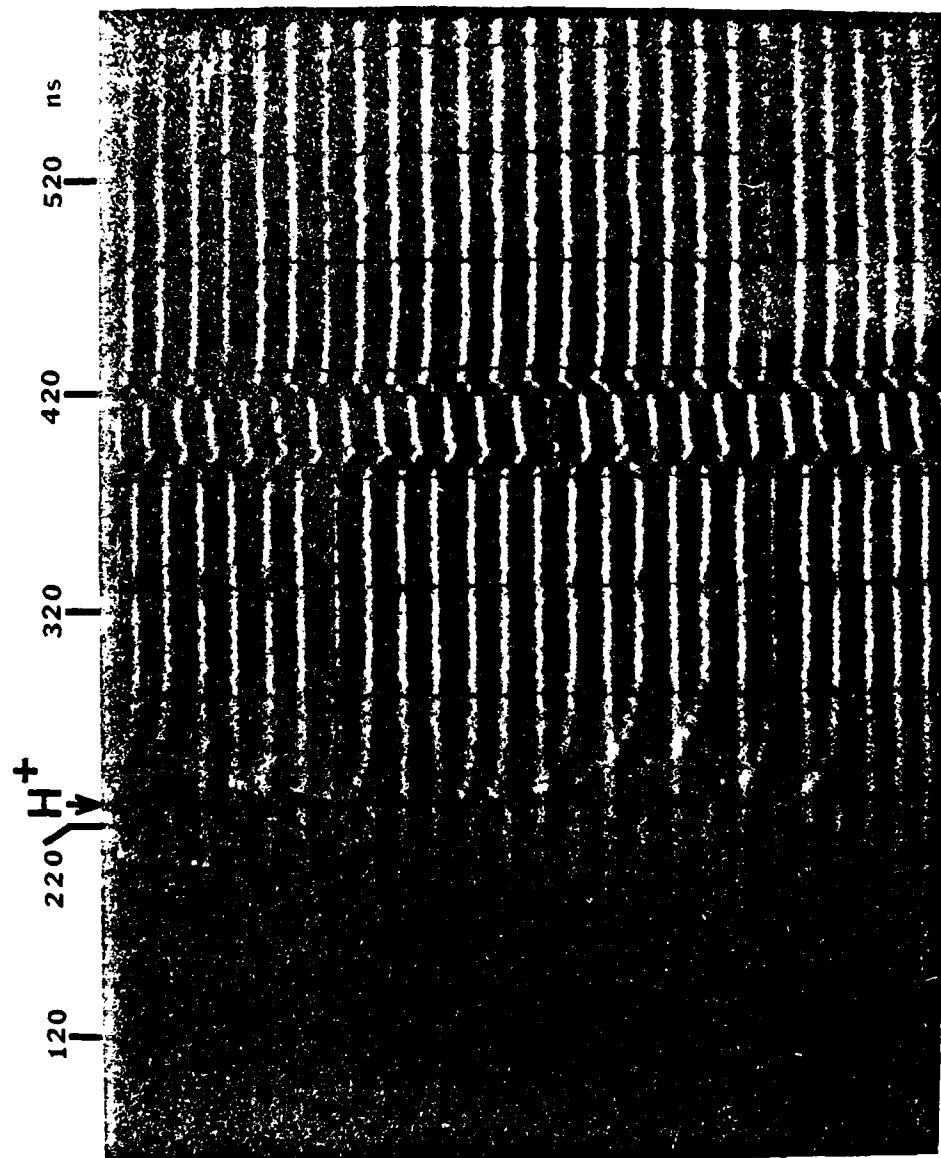


Figure 21. Oscilloscopic time signals showing the arrival of  $H^+$  desorbed from a rhodium tip.

example, the dissociation,



occurring at a distance of 3.2 tip radii from an 8 kV tip would yield an apparent mass of 1.1 amu as shown by J. A. Panitz.<sup>66</sup> In addition, only  $\text{H}^+$  ions were observed. This is in agreement with the predominant species observed during pulse evaporation by S. V. Krishnaswamy and E. W. Müller.<sup>73</sup> However, during slower DC evaporation rates in a magnetic sector atom-probe,  $\text{H}^+$ ,  $\text{H}_2^+$ , and  $\text{H}_3^+$  ions have been observed by S. Kapur and E. W. Müller.<sup>72</sup>

By gating the detector on during the arrival of the pulse desorbed  $\text{H}^+$  ions, distributions were obtained showing the selective adsorption of hydrogen over the rhodium surface. These desorption patterns are shown in Figures 22(a, b, and c) both separately and superimposed over a neon field-ion micrograph of the surface. Figures 22(a and b) are each the sum of 100 pulse desorptions taken at regular intervals for a period of 3 minutes at a pulse fraction of about 10%, and Figure 22 (c) is an integrated photograph (camera apertured down from f/1.4 to f/2) of 300 pulse desorptions taken at regular intervals for 10 minutes at a pulse fraction of 20%. The distribution taken at the lower holding field shown in Figure 22(c) indicates variations in a significantly heavier coverage than that in either Figure 22(a) or 22(b), and with this increase coverage some pulse evaporation of the rhodium substrate did occur. This evaporation of the substrate at the heavier coverage indicates that those areas in the light coverage patterns,

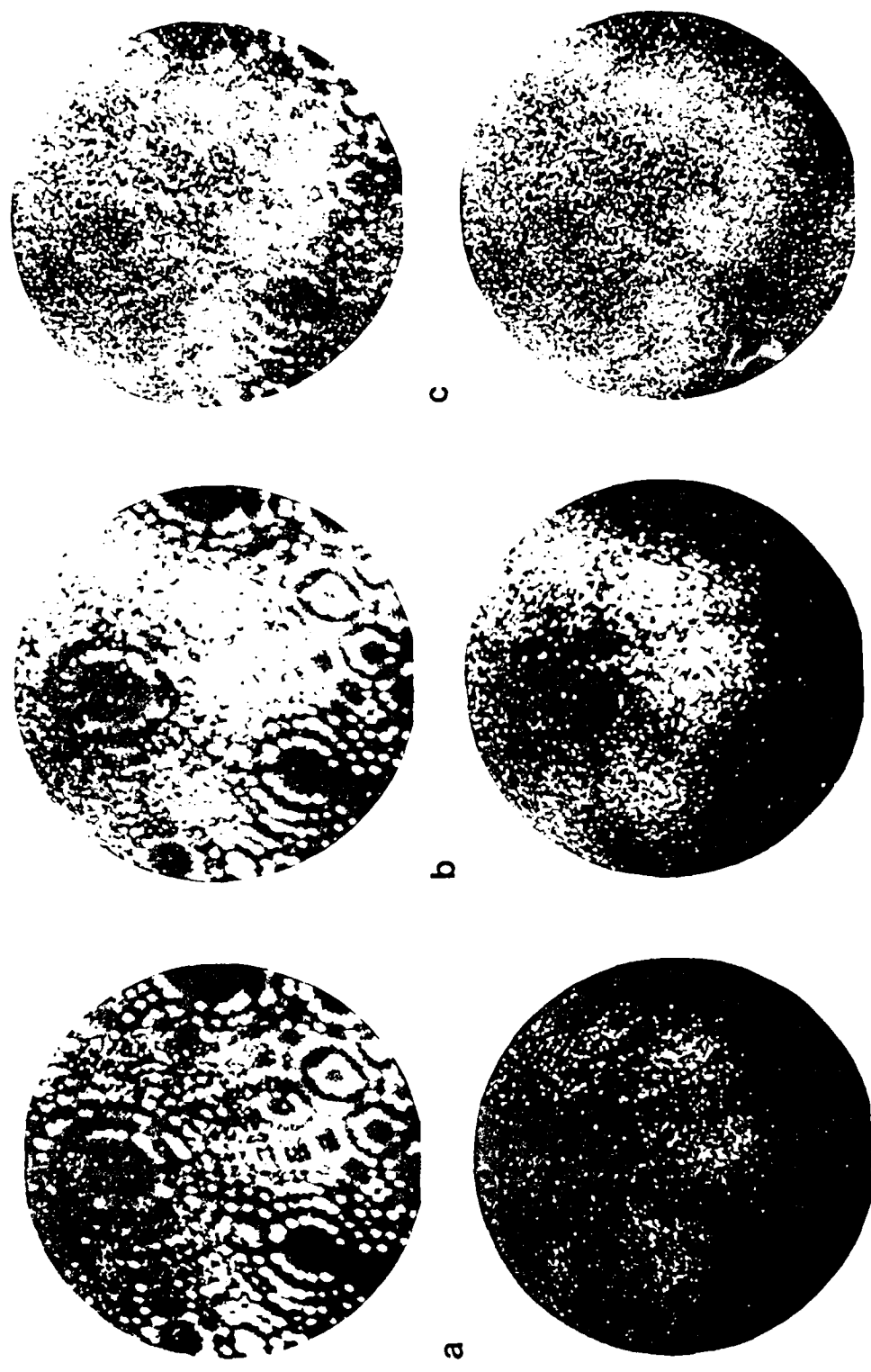


Figure 22. Desorption micrographs showing various degrees (a, b, and c) of selective field adsorption of hydrogen on the rhodium tip shown in Figure 20.

Figures 22(a and b), showing minimal desorbed  $H^+$  are, in fact, where little or no hydrogen adsorbed, since, if hydrogen were present, one would expect to observe evaporation of the substrate.

Figures 22(a and b) show very little adsorption on the 001 and 113 planes, and reduced adsorption along the [110] and [020] zones. However, significant hydrogen adsorption has occurred in the atomically rough regions between these zones. At heavier coverage, Figure 22(c), the adsorption has become more uniform. However, reduced hydrogen coverage about the 001 and 113 planes as well as along zone [110] is still evident. These variations in coverage were not previously recognized with either time-of-flight <sup>73</sup> or magnetic sector <sup>72</sup> atom-probes nor have they (prior to this) been clearly shown by imaging atom-probe. <sup>15,73</sup> In view of this, confirmation was obtained by energy corrected atom-probe with the cooperation of Yee S. Ng. This work was conducted by Ng at still heavier coverage, and it also showed a significantly higher abundance of  $H^+$  desorbing from about the 102 plane as compared with the 113. At this heavy coverage, normally trivalent rhodium <sup>75</sup> may form  $RhH_3$  on the surface, which would then evaporate as  $RhH_3^{++}$  or as fragments,  $RhH_2^{++}$  and  $RhH^{++}$ . In view of this work, it would be informative to re-examine the extremely low abundance reported <sup>72,73</sup> for rhodium hydrides by investigating those regions which show significant hydrogen adsorption. As part of this, a distribution of the detected, Figure 15,  $RhH_3^{++}$  species could be obtained with the less than 10 ns gate width now available with the imaging atom-probe.

The influence of the detailed atomic structure of the surface on the hydrogen adsorbate may be seen by careful examination of

Figures 22 (a and b). However, it is most easily seen in the color composite of Figure 22(b), Figure 23, which may be found in the cover pocket. There, the scalloped structure of the adsorbed hydrogen distribution about crystal planes along the [020] zone between the 102 and 001 plane is clearly seen.

It is reasonable to say that these results show that more densely packed planes provide the least binding, and that rough, more open regions and plane edges provide increased binding. The binding sites are those which offer more near neighbors to an adsorbate<sup>64</sup> as well as field-induced dipole-dipole binding.<sup>29</sup> These experiments show the selective adsorption of hydrogen in the spaces available on more open atomic planes as invoked by Müller,<sup>76, 49</sup> to explain hydrogen promoted imaging, and Gomer,<sup>64</sup> for the surface diffusion behavior of hydrogen at low coverage (0.8 to 1 monolayer).

These results indicate the possibility of obtaining atomically detailed distributions of reactants and products over the surface of a catalytic metal. An example which could be investigated is the hydrogenation of benzene,<sup>75</sup> C<sub>6</sub>H<sub>6</sub>, in the temperature range 25 to 225°C over a rhodium catalytic surface. Since it is known<sup>68</sup> from field ionization mass spectrometry that rings of aromatic and heterocyclic compounds do not field dissociate, ions of cyclohexadiene, C<sub>6</sub>H<sub>8</sub>, cyclohexene, C<sub>6</sub>H<sub>10</sub>, and cyclohexane, C<sub>6</sub>H<sub>12</sub>, may be expected during desorption. Desorption patterns of these products could be separated from benzene with a high resolution imaging atom-probe. These distributions may be taken within the reaction temperature range without reducing the resolution of the desorption patterns. However, observations during the

reaction would have to be conducted at low pressures suitable to the instrument's high vacuum requirements.

## 2. Atomic Analysis of Ni and Ni-P Deposits

This work is an atomically detailed characterization of pure nickel electroplate and nickel phosphorus electroless plate. The morphological features of these deposits are presented at atomic resolution in field-ion and field-evaporation micrographs of the plating taken at various depths within the deposit sample. Access to known depths of the sample is acquired by controlled, layer-by-atomic-layer, low temperature field evaporation. In conjunction with their morphological features, the chemical composition of each deposit is obtained by time-of-flight, atom-probe mass spectrometry, and selected constituent mass species' surface distributions are displayed by imaging atom-probe.

The samples used in this work were obtained from macroscopic nickel and nickel phosphorus plates chemically stripped from their substrates. Chips of these materials and mounted specimens are shown in Figure 24. Such specimens are prepared by macroscopic shaping and polishing with zone etching<sup>77</sup> and subsequent atomic smoothing by field evaporation. These specimen materials are representative of practical electro- and electroless plating processes, and nickel and nickel phosphorus represent both the most important and the majority of material plated by each process.<sup>78, 79</sup> Results obtained from these samples of bulk platings may be compared with studies using other techniques, X-ray and electron diffraction and electron microscopy, etc.<sup>43</sup> This is in contrast with earlier field-ion imaging of platinum deposited directly on tungsten emitters,<sup>80</sup> preliminary work (Pt on W emitters and wires)

**Ni ELECTROPLATE  
AND  
Ni-P ELECTROLESS PLATE**



Figure 24. Nickel and nickel-phosphorus chemically stripped plate material and mounted specimens.

by this author,<sup>37</sup> and similar work (Ni on 303 stainless steel emitters and black chrome on Ni emitters) by others.<sup>81</sup>

The pure nickel electroplate material was obtained by electro-deposition at room temperature in a watts-type<sup>79</sup> bath whose composition and assay was as follows:

$\text{NiSO}_4 \cdot 7\text{H}_2\text{O}$  210 g/l (Cu/Fe/Co/Mn < 0.005%, 0.1% other)

$\text{NiCl}_2 \cdot 6\text{H}_2\text{O}$  60 g/l (Cu/Fe/Pb < 0.005%, 0.2% Co, 0.2% other)

$\text{H}_3\text{BO}_3$  30 g/l (Fe/Pb/Ca/PO<sub>4</sub> < 0.005%)

Efficient dissolution of the 99.99% pure nickel-270 anodes was insured by a chloride content slightly higher than usual for this bath,<sup>79</sup> while the pH was held at 5.3 by buffering with  $\text{H}_3\text{BO}_3$ . The plating current density and cell voltage were 0.02 amp/cm<sup>2</sup> and 2.2 volts, respectively. The pure nickel electroplate which deposited on the Ag paint-on-Ta foil cathodes was then removed by stripping off the Ag paint with acetone. This nickel electroplate was produced at the University of Florida, Department of Materials Science and Engineering, and obtained from M. Kersker via A. J. Melmed, National Bureau of Standards.

Figure 25 shows a neon image of one of three orientations observed at various depths of a single pure nickel electroplate specimen. Here, the neon pressure was  $5 \times 10^{-6}$  Torr with a background pressure of  $2 \times 10^{-9}$  Torr, and the best neon image potential was 8.5 kV with the sample at 78 K. This imperfect nickel surface appears to be 111 oriented with this plane at the bottom of the image. It exhibits many defects such as vacancies, small voids, and both large and small amorphous regions. In addition, numerous mismatches of the lattice appear in these images as a network of atomic-width boundaries whose configuration varies with depth, as observed during field evaporation. The structure

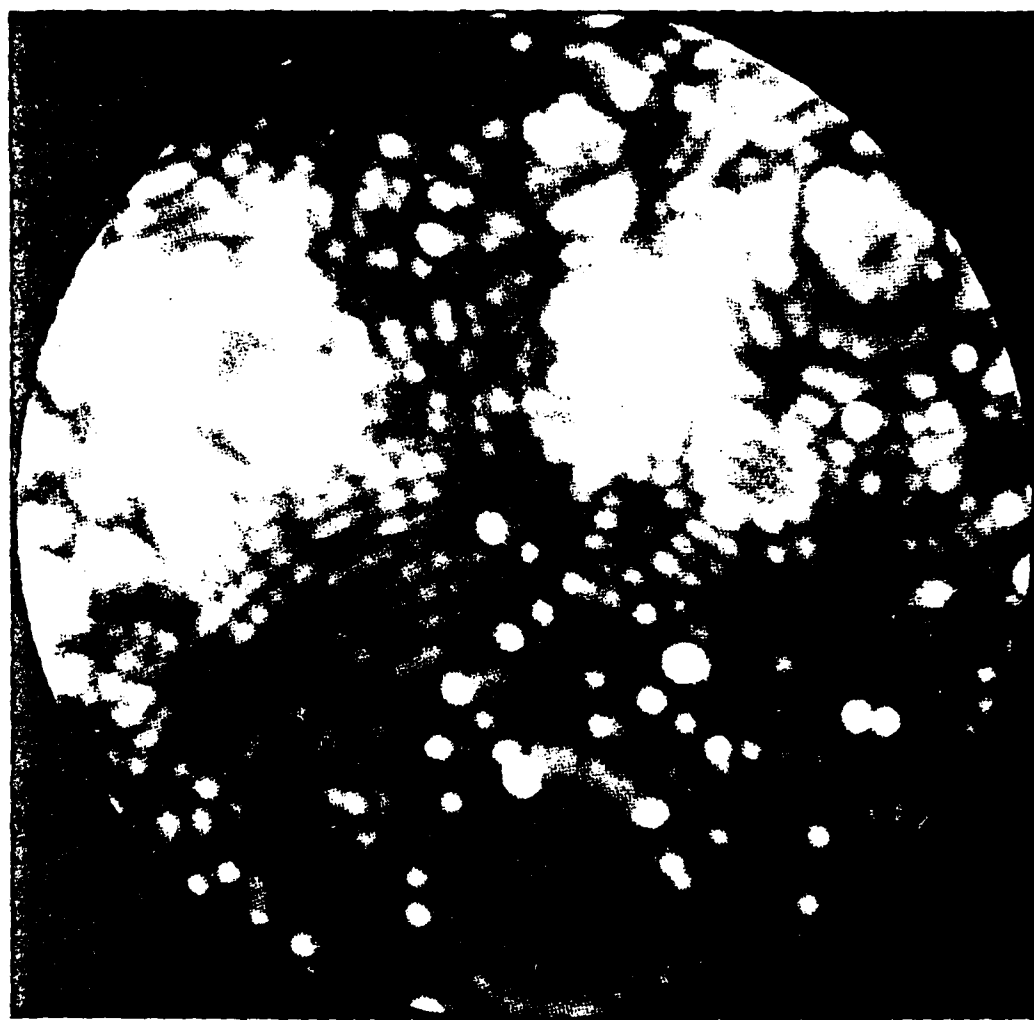


Figure 25. Pure nickel electroplate as imaged with Ne.

in the upper left of Figure 25 shows adjacent crystal nuclei which have impinged on one another during growth. Such a mechanism of lattice misalignment was proposed by R. T. Allsop<sup>82</sup> to account for the internal stress of electrodeposits. The random elastic displacement of atoms caused by such extensive defects can account for the microstrain observed in electrodeposits as order dependent broadening of X-ray and Pseudo-Kossel X-ray diffraction lines.<sup>43</sup>

Further field evaporation of this pure nickel electroplate revealed two different, apparently 001 oriented, surfaces. The first, major plane was at the top of the image, appeared after the field evaporation of some 65 layers or about 130 Å, and the second, major plane at the right, was observed with the further field evaporation of some 200 layers or about 350 Å. Although not presented in this work neon field-ion micrographs of these two surfaces were taken at the same temperature and pressure conditions as those used while obtaining Figure 25, and the best neon image potentials were 9.1 kV and 11.2 kV, respectively. The change from one orientation to another during evaporation showed the surface displaying increasing amorphous regions until a new orientation was initiated by a slight "flash", the clumped evaporation of several atomic layers. While evaporating through the 350 Å depth, a 15-layer DC evaporation pattern and two-multiple-pulse patterns were taken. Neither variety of pattern exhibited the geometric symmetry of similar patterns<sup>31</sup> obtained from single crystal samples, as shown for 111 oriented nickel in Figure 18. Although some variation in ion yield over the

surface was apparent, these patterns did not exhibit the regular variations observed with single crystal samples, and the patterns obtained from the nickel electroplate were generally more uniform in appearance.

The polycrystalline grain structure of thick nickel electroplate observed at atomic resolution in this work agrees with that observed for deposits in excess of 5 microns thickness by J. Gündiler and L. E. Murr.<sup>83</sup> Their observations were conducted by scanning and transmission electron microscopy and electron diffraction. Further, the grain size of 350 Å, observed during field evaporation, is in reasonable agreement with the "particle" size used to account for order independent broadening of Pseudo-Kossel, X-ray diffraction lines obtained from a 12 micron thick nickel electroplate.<sup>43</sup> Finally, lattice defects which will contribute integrally with "particle" size to such broadening of X-ray diffraction lines are shown in Figure 25 with atomic detail.

The composition of this pure nickel electroplate was determined by the imaging atomic-probe's time-of-flight mass spectrometry capability, and Figure 26 shows a histogram of the relative abundance of species detected at the outset of the 350 Å deep field evaporation. A total of 1451 ions were collected in four sequential groups of about 360 ions each with the sample in vacuum at a background pressure of  $2 \times 10^{-9}$  Torr. The various ionic species identified are given in Figure 26, and a more detailed summary appears in Table 1. This histogram shows the presence of residual neon imaging gas, background hydrogen, and possibly some constituent boron,  $^{58}\text{Ni}^{11}\text{B}^{++}$ , and hydrogen,  $\text{H}^+$  and nickel hydrides. However, the  $^{58}\text{Ni}^{11}\text{B}^{++}$  signals

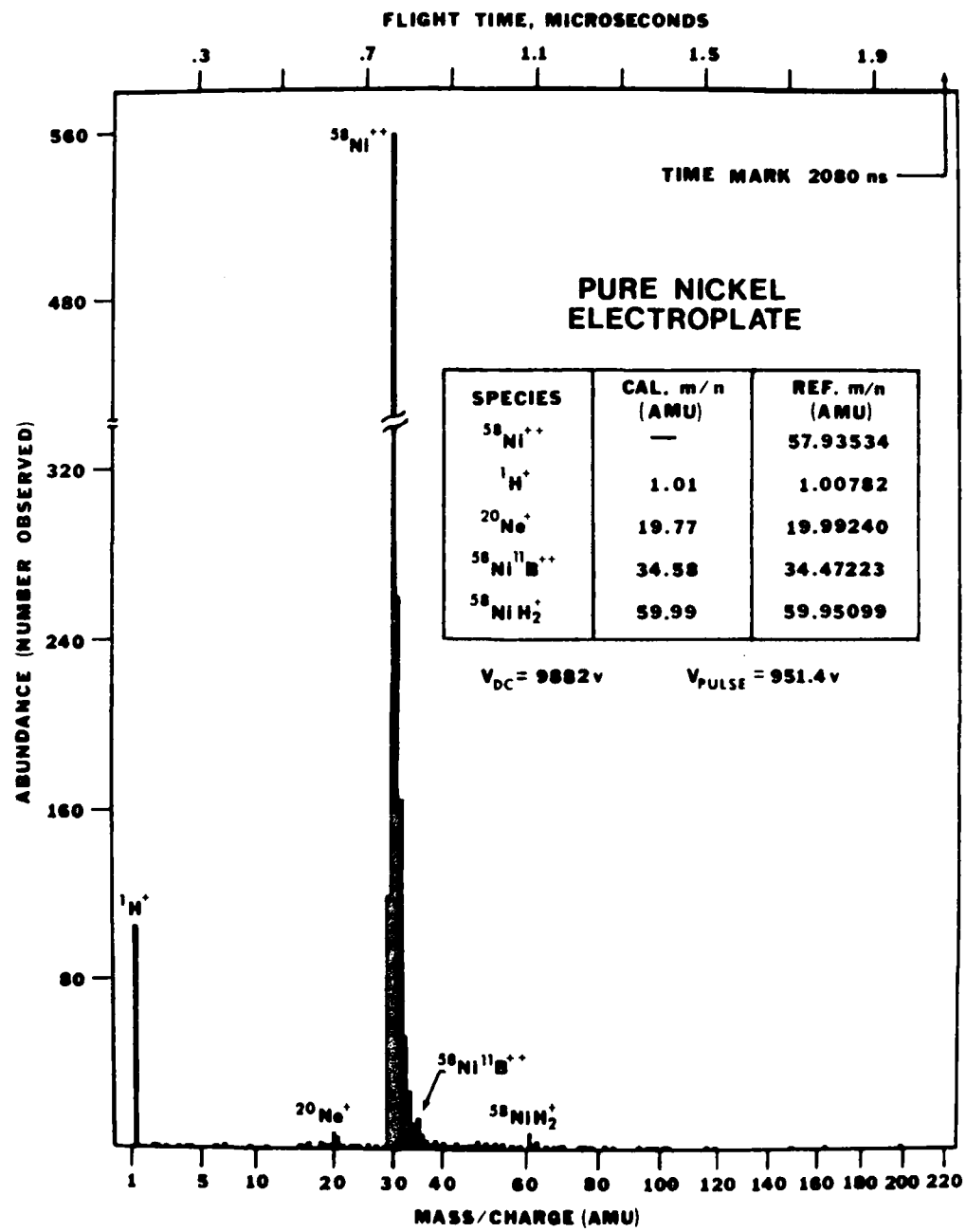


Figure 26. Relative abundance histogram for pure nickel electroplate evaporated in vacuum.

were most likely artifact detector after-pulses due to residual neon adsorbed on the detector, while the large majority of observed  $H^+$  and nickel hydrodes originate from field adsorbed background hydrogen. That is, the  $^{58}Ni$   $^{11}B^{++}$ ,  $^{20}Ne^+$ , and  $^{58}NiH_2^+$  peaks were obtained primarily from the first 350 ions collected; after which, no statistically significant yield of these ions was observed during the repetitive pulse evaporation, an average of about one to two pulses per second. Such a decline in the number of after-pulse signs as the amount of gas adsorbed on the detector diminishes would be expected; and, further, the  $^{58}Ni$   $^{11}B^{++}$  signals were detected at a characteristic after-pulse interval of 70 ns after the main  $^{58}Ni^{++}$  peak. Also, no simple ionic boron was detected. Along with the decline in  $^{58}NiH_2^+$  signals, the number of detected  $H^+$  ions diminished by 25% relative to the nickel yield indicating the expected reduction in field adsorbed hydrogen during repetitive pulsing. However, the majority of remaining  $H^+$  signals are still due to adsorbed background hydrogen, rather than hydrogen codeposited during electroplating, since the relative abundance of  $H^+$  is similar to that observed from pure nickel at the same background pressure.

The possible codeposition of a small percentage of hydrogen was inferred by a shift in abundances (relative to pure nickel at the same pressure) in an expanded spectra of 1728 ions collected about the  $^{58}Ni^{++}$  line. The range of this expanded spectra was from 27 to 37 amu, and, although not presented here, was similar to the unapertured data from pure nickel shown in Figure 19 (top). However, this spectra showed a less delineated isotopic structure and a shift in abundances, e.g.,

relative depletion of the leading  $^{58}\text{Ni}^{++}$  line, toward more nickel hydride species. Further, none of the impurities (sulfur, chloride, and boron) likely to be codeposited from the constituents of the plating bath were detected in significant numbers. That is, the total amount of S, Cl, and B is less than 0.6%. In addition, it is likely that a small percentage, ~0.2%, of the electroplate was cobalt,  $^{59}\text{Co}^{++}$ , but such a low abundance could not be distinguished from  $^{58}\text{NiH}^{++}$  with a mass resolution of less than 6000.

The above indicates that this nickel electroplate is better than 99.4% pure, excluding cobalt and hydrogen whose abundances are less than 1%, but uncertain. This and gated images showing only a slight random hydrogen coverage over the surface indicate that the amorphous and crystalline regions shown in Figure 25 are both composed mostly of nickel. Hence, the defects in the structure are most likely due to the growth mechanism and low concentrations of both included impurities, e.g., sulfur in nickel electroplate,  $^{84}$  and codeposited hydrogen. Such impurity levels, as low as several parts per million, may be easily determined in the future by computerizing the imaging atom-probe's data acquisition. If, in conjunction with rapid data acquisition, a known percentage of the plating bath constituents are deuterated as an identifying counting aid, the concentration of codeposited hydrogen could also be definitively determined.

The most fruitful application of the imaging atom-probe within this work is the investigation of nickel-phosphorus electroless plate. This plate is an amorphous high nickel-low phosphorus alloy deposited without an external electric current by the controlled autocatalytic reduction

of  $\text{Ni}^{++}$  with hypophosphite anions,  $[\text{H}_2\text{PO}_2]^-$ , at the surface of the body being plated. The process was originally developed <sup>85</sup> and patented by A. Brenner and G. Riddell at the National Bureau of Standards, and many subsequent improvements, enumerated by G. Gutzeit in the "Electroplating Engineering Handbook," <sup>44</sup> have made this process industrially useful. <sup>43, 44, 78, 87</sup> The probable chemical reactions and various bath compositions have been given by A. Brenner and G. Riddell <sup>85</sup> and by G. Gutzeit. <sup>44</sup>

The Ni-P (2.7% by weight) electroless plate used in this work was obtained by deposition at 95°C for 5 hours at a rate of 0.2 mil per hour. The bath composition was as follows:

$\text{NiCl}_2 \cdot 6\text{H}_2\text{O}$	60 g/l
$\text{NaH}_2\text{PO}_2 \cdot \text{H}_2\text{O}$	1 g/l
Na Hydroxyacetate	75 g/l

Nickel and hypophosphite were continuously added along with 1% NaOH in order to replace consumed chemicals and to maintain the pH between 6 and 6.5. Here, sodium hydroxyacetate was used as a buffer and chelating agent. As a chelate, it "binds up" nickel ions preventing the early precipitation of nickel orthophosphite which would cause the catalytic decomposition of the bath. The nickel-phosphorus deposit resulting from this bath was then stripped from its brass substrate to provide the needed sample material. This plate and the required specimens were prepared at the National Bureau of Standards through the co-operation of A. J. Melmed.

Figure 27 shows four imaging atom-probe displays of as-deposited nickel-phosphorus electroless plate. Figure 27(a) shows a neon image

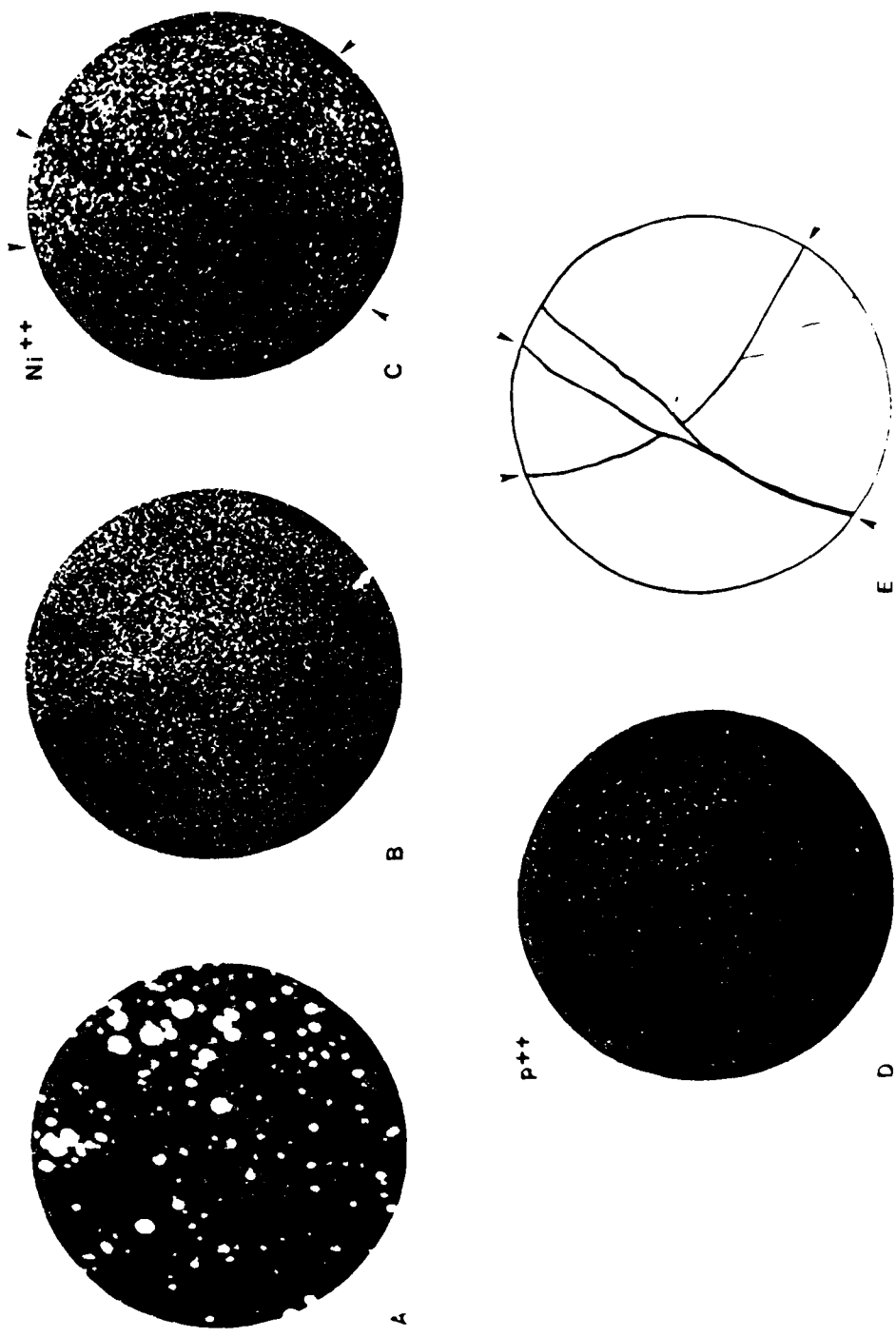


Figure 27. Nickel-phosphorus electroless plate (as-deposited) imaged (a) with  $\text{Ne}^+$ , (b) by multilayer DC evaporation, and by multiple-pulse evaporation (c) gated for  $\text{Ni}^{++}$  and (d) gated for  $\text{p}^{++}$ . (e) Diagram of discernible atomic width boundaries.

obtained at the best neon image voltage, BIV, of 7.8 kV with the sample at 78 K. This image was obtained at the conclusion of the characterization depicted in Figure 27 and just prior to annealing of the sample. It is representative of several neon images obtained from surfaces at various depths (BIV = 6.2, 7, and 7.8 kV) within the as-deposited sample. The neon pressure during imagining was  $5 \times 10^{-6}$  Torr with a background at  $2 \times 10^{-9}$  Torr. These neon field-ion micrographs were all similar in character and displayed the random structure of an amorphous material with only some small, ~20 atoms, ordered regions, microcrystallites. The excessively bright spots in these neon micrographs are due to the presence of phosphorus. This is clearly demonstrated with neon micrographs taken after annealing the sample, and which are presented later in this work.

After the initial neon micrograph at 6.2 kV, two DC multilayer evaporation patterns were taken in vacuum,  $2 \times 10^{-9}$  Torr background. Figure 27(b) shows the second of these integrated photographs (camera stopped down to f/4) consisting of some 15 to 20 atomic layers evaporated at about 8 kV. This pattern contains self-image points of nickel, phosphorus, and all other evaporated ions. The generally uniform ion yield displayed in this pattern suggests that extended crystals were not present, but those variations which are discernible in Figure 27(b) persisted with depth indicating some type of extended structure. The nature of this structure is clearly exhibited in Figure 27(c) which shows a gated image displaying only evaporated  $\text{Ni}^{++}$  ions. Here, a fine network of atomic width, several angstroms, boundaries are visible and marked with the prominent boundaries graphically shown in

Figure 27(e). This network extended through the 200 - 300 Å depth examined prior to annealing, and, as shown later, was recovered intact after the annealing process.

In an investigation <sup>45</sup> of as-deposited Ni-P by A. Goldstein et al. and G. Gutzeit, extended boundaries were observed with optical metallography at a magnification of 1000 times. These matching interfaces were generated where macroscopic growth regions met, and their width was not optically discernible (less than the wave length of the incident light). These authors proposed as "reasonable conjecture" that the atomic disregistry at such interfaces is the same as that at a grain boundary, and that the deposits laminated growth results from a common "wave" front generated by the collision of spherical growth fronts from many adjacent nuclei. Such a growth mechanism could yield the microscopic network of boundaries observed with the imaging atom-probe. Also, the atomic width of these boundaries indicates the match at such interfaces is indeed equal or near equal to that of a grain boundary (interface between adjacent crystalline orientations). However, as noted by A. Goldstein et al. and G. Gutzeit, such boundaries are not properly designated as grain boundaries, since as-deposited Ni-P is amorphous (as indicated by X-ray <sup>45</sup> and imaging atom-probe). This may be a matter of semantics, since these boundaries may become or are in some sense grain boundaries. For example, as indicated earlier, such boundaries persisted as the interface between the ordered crystalline phases observed after annealing as-deposited Ni-P.

The distribution of phosphorus over the as-deposited Ni-P sample appeared random as shown in the image gated for P<sup>++</sup> presented in

Figure 27(d). Both the  $\text{Ni}^{++}$  and  $\text{P}^{++}$  gated images are the result of some 400 pulse evaporation with about the same total yield of ions per pulse (as observed in non-gated pulse evaporation of the sample). Hence, these gated images also qualitatively reflect the abundance of  $\text{P}^{++}$  relative to  $\text{Ni}^{++}$ .

This selective imaging of  $\text{Ni}^{++}$  and  $\text{P}^{++}$  was performed by synchronously activating the chevron, channel plate detector for 10 ns at the repeatedly observed earliest arrival times for  $\text{Ni}^{++}$  and  $\text{P}^{++}$  ions.

Figure 28 (top and bottom) shows repeated oscilloscopic traces displaying signals from arriving  $\text{Ni}^{++}$  and  $\text{P}^{++}$  ions. The fiducial mark present on each trace may be deployed to any observed ionic species for subsequent imaging by synchronous triggering of the detector. For example, the fiducial mark is properly deployed to image  $\text{Ni}^{++}$  ions by precisely, 1 ns increments, setting a digital time delay while observing the expanded sweep, Figure 28 (bottom), of the appropriate region, intensified, of the full time-of-flight trace, Figure 28 (top). The sweep rates in Figure 28 (top and bottom) are 200 and 20 ns, respectively.

By totalizing the signals from many traces like those in Figure 28, both full and isotopic relative abundance histograms were obtained for as-deposited Ni-P. These are shown in Figure 29, and they were obtained with the sample in vacuum at a background pressure of  $2 \times 10^{-9}$  Torr. The full histogram contains 1475 ions, while 421 additional ions were collected about the arrival of  $^{58}\text{Ni}^{++}$  for the isotopic sweep. The retarding fraction, observed flight time, and calculated mass-to-charge ratios for species identified in Figure 29 are given in Table 1. These

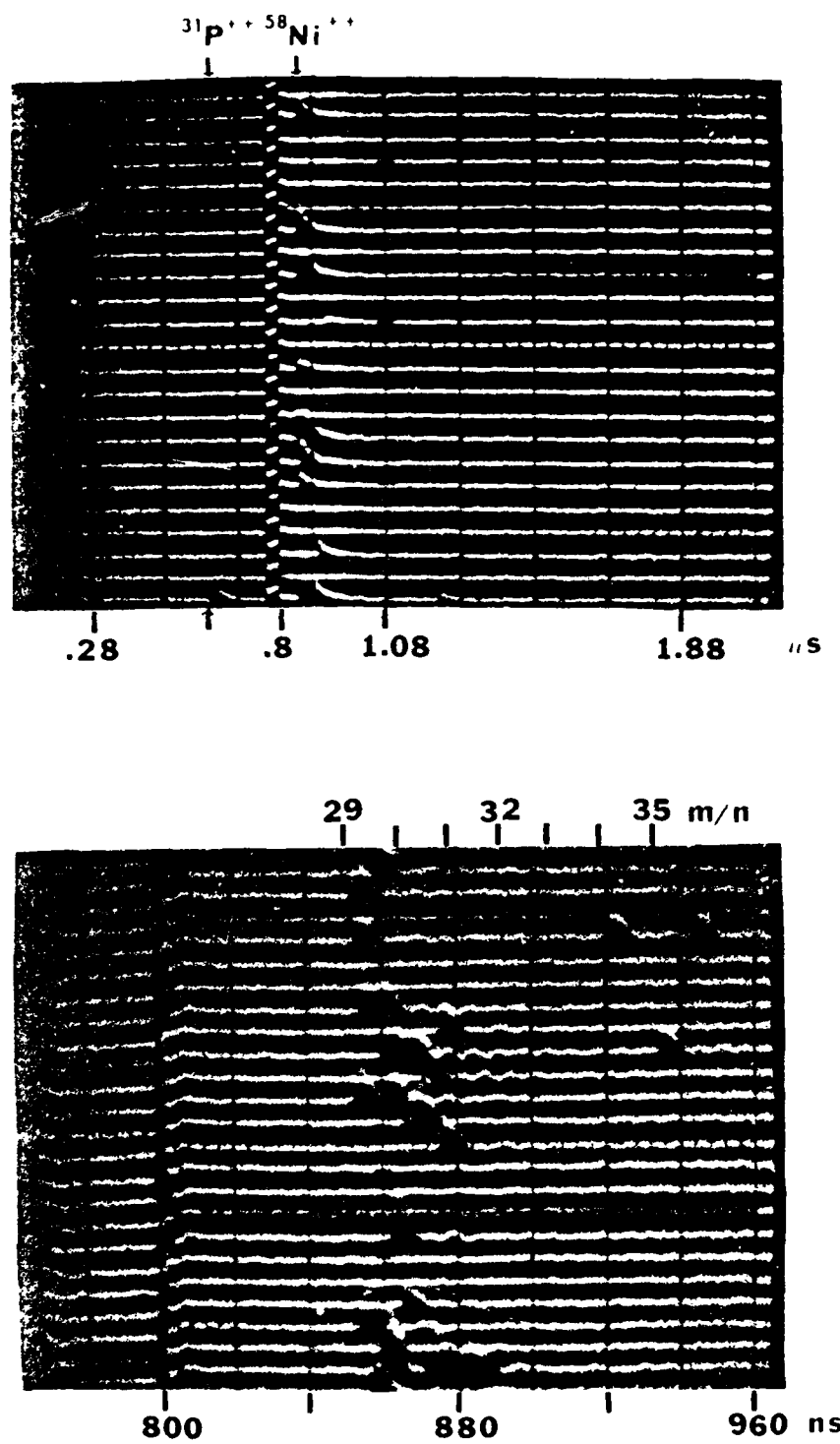


Figure 28. Oscilloscopic traces of nickel-phosphorus electroless plate (as-deposited): (top) full mass sweeps with region intended for expansion intensified, (bottom) expanded mass sweeps of intensified region.

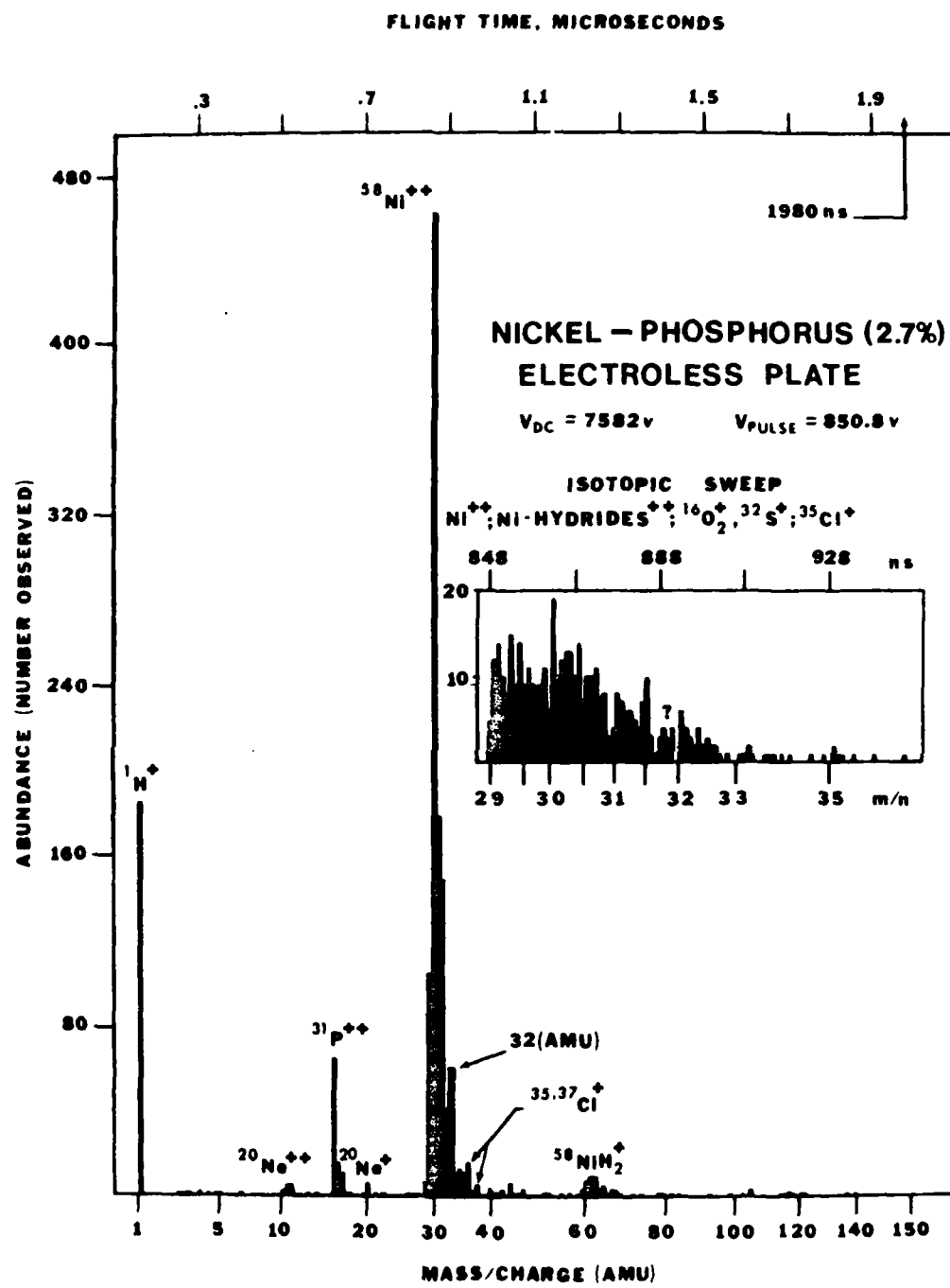


Figure 29. Relative abundance histograms for full and isotopic mass sweeps of as-deposited nickel-phosphorus.

histograms show the expected phosphorus constituent and possibly some included oxygen, chlorine, and hydrogen. In addition, they show the presence of 1.3% adsorbed residual neon imaging gas and background hydrogen. Here again, the majority of the observed 12.5%  $H^+$  ions and nickel hydrides are due to field-adsorbed hydrogen. For example, the abundance of  $H^+$  ions is greater than the 7.3% formerly observed for pure nickel electroplate, Figure 26, but this is likely due to the larger 11.2% (9.6% for the data in Figure 26) pulse fraction employed rather than an increase in constituent hydrogen. That is, the combination of lower bias potential and larger pulse potential permitted more hydrogen to adsorb onto the Ni-P sample between pulse evaporation events.

If the adsorbed residual neon and hydrogen are discounted, the composition of as-deposited Ni-P is probably better than 98% pure. That is, slightly less than 1% of the collected ions were attributed to included chlorine, and all but about 1% of the ions collected at 32 amu can be accounted for by nickel, its hydrides, and "tailing" of spectral lines. For example, the expected natural abundance of  $^{58}Ni$  and that shown in Figure 29 indicate <sup>72</sup> that roughly 70% of the nickel present was observed as hydride. Therefore, about half the 6% of ions collected at 32 amu can be counted as  $^{64}Ni$ ,  $^{62}NiH_2$ , and  $^{62}NiH_3$ . An additional 1 to 2% of the remaining 3% are attributable to "tailing" through comparisons with pure nickel and nickel electroplate mass spectra. However, the remaining 1% may be oxygen included within Ni-P during deposition. Since this is considerably larger than the 0.0023% observed spectrographically by A. Goldenstein et al. and G. Gutzeit, <sup>45</sup> further higher resolution atom-probe mass spectra are needed for a more credible estimate of the oxygen concentration.

Phosphorus ions comprised 6.3% of the total number of ions collected for the full histogram, and, if adsorbed neon and hydrogen are not counted, this represents a concentration of 7.6 atomic percent phosphorus within as-deposited Ni-P plate. That is, the observed phosphorus content was 4% by weight rather than the 2.7% expected. However, this difference is well within the bounds for variation in phosphorus content displayed by optical metallography<sup>45</sup> of macroscopic Ni-P samples partly crystallized by annealing.

Upon annealing at 400°C or above, the metastable amorphous-like Ni-P electroless alloy plate rapidly transforms<sup>45</sup> to an equilibrium dispersion of the tetragonal<sup>88</sup> Ni<sub>3</sub>P intermetallic phase within a matrix of crystalline Ni. The size of the dispersed crystalline Ni<sub>3</sub>P particles increased with both the temperature and duration of the heat treatment. This has been used to controllably vary the hardness,<sup>45</sup> wear resistance,<sup>43</sup> electrical resistance,<sup>44, 87</sup> and magnetic properties<sup>43</sup> of Ni-P and similar electroless deposits.

In the field-ion micrographs of Figure 30, the nature of this transformation is depicted in atomic detail which reveals features unobserved with transmission electron microscopy.<sup>43</sup> Here, the as-deposited Ni-P, Figure 30(a), was heated in vacuum ( $2 \times 10^{-9}$  Torr background) at about 600°C for 20 seconds, and then re-imaged with neon at a pressure of  $5 \times 10^{-6}$  Torr. The sample temperature was 78 K during imaging, and the neon BIV was 10 kV at the end of the image sequence.

Figure 30(b) shows the ordered surface of the heat treated Ni-P sample after field evaporating several layers, and Figure 30(c) shows the observed surface of the same ordered overlayer after evaporating 20

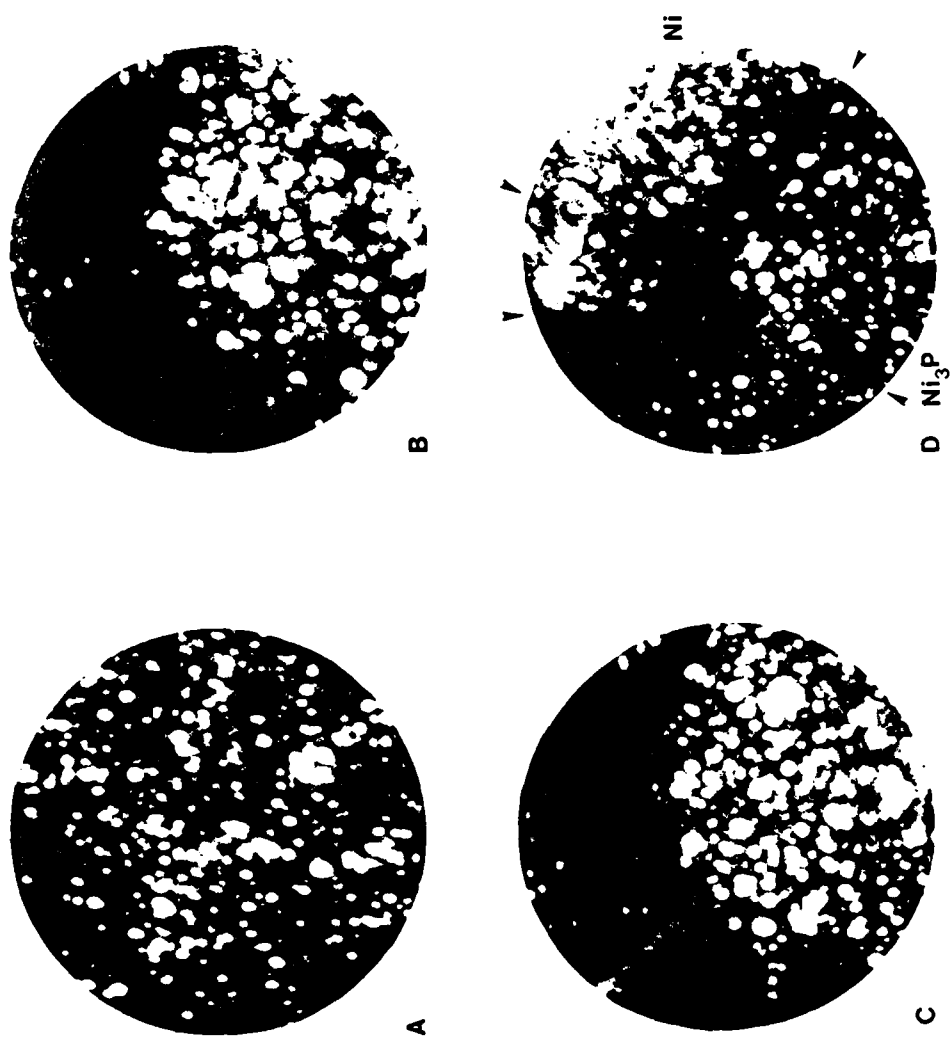


Figure 30. The transition of Ni-P to ordered Ni-Ni<sub>3</sub>P as imaged with Ne-  
less plate, (b) an ordered Ni-P overlayer after annealing at ~600°C for 20 s, and after field  
evaporation of (c) ~50 layers and (d) ~20 layers to show the underlying phase mixture of Ni  
and Ni<sub>3</sub>P with the retained atomic width boundaries.

atomic layers. This crystalline overlayer is rich in phosphorus indicating the possible segregation of phosphorus to the surface during the heating process. Such a supersaturated crystalline solution was proposed by A. Goldenstein et al. and G. Gutzeit <sup>45</sup> as an intermediate step in the formation of the equilibrium dispersion of  $\text{Ni}_3\text{P}$  in Ni. Figures 30(b and c) show that such a phase occurred as a result of heat treatment, but whether this observed structure is the remnant of a bulk phase or a purely surface structure is somewhat uncertain. Experimentally, all heat treated samples exhibited this structure only as an overlayer of varying thickness which had to be field evaporated in order to expose the underlying equilibrium dispersion of  $\text{Ni}_3\text{P}$  in Ni.

The phase mixture of  $\text{Ni}_3\text{P}$  in Ni shown in Figure 30(d) was uncovered after the field evaporation of about 50 atomic layers, and it has retained the original boundary structure of the as-deposited Ni-P. The prominent boundaries in the equilibrium dispersion which are coincident with those of the as-deposited material are marked in Figure 30(d) as they are in Figure 27(c). These boundaries could now be selectively designated as either grain or phase boundaries, and they simply reflect the original structure inherent in the as-deposited Ni-P. This indicates that it is prudent to classify materials such as electroless Ni-P and perhaps metallic glasses as amorphous-like rather than amorphous (indicating "liquid-like" disorders).

The highly contrasted bright image spots in Figures 30(a, b, and c) result from the presence of phosphorus. This is clearly demonstrated in Figure 30(d). There, the Ni portion shows few such image spots, while the  $\text{Ni}_3\text{P}$  has many as does a small vestige (just below and left of center) of the ordered overlayer.

After removing the last remnant of the overlayer, a mass analysis of the equilibrium  $\text{Ni}_3\text{P}$  in Ni dispersion was conducted, and the resulting histogram is shown in Figure 31. The calculated mass-to-charge ratios and associated flight times for species identified in Figure 31 are given in Table 1. Because of the crystallized sample's slight instability while under field stress, the 769 ions counted in this histogram were collected immediately after the neon imaging sequence, Figure 30. Therefore, the histogram shows 5% adsorbed neon and 18% "grass" signals from field ionized residual neon and hydrogen, even though the background pressure was always better than  $2 \times 10^{-9}$  Torr.

The decrease to 5% in the abundance of  $\text{H}^+$  after annealing may, in part, be due to the presence of neon<sup>76</sup> and the reduction to 10.6% in the pulse fraction. However, the absence of  $\text{NiH}_2^+$  signals and the magnitude, greater than 50%, of the decrease in  $\text{H}^+$  ions after heating suggest the codeposition of hydrogen. Nevertheless, this cannot be conclusively established until deuterium is used, in the manner discussed earlier, to distinguish between codeposition and adsorption. Further, this decrease in the abundance of hydrogen and possibly oxygen after heating has reduced the 32 amu peak observed in the as-deposited Ni-P to the point where it is indistinguishable from the "tailing" of the main  $\text{Ni}^{++}$  peak. In addition, even if the low abundance of chlorine detected in the as-deposited Ni-P (Figure 29) were still present after heating, it would, unfortunately, be within the "grass" signals. Lastly, the observed abundance of phosphorus after annealing increased to 8% by weight. This is in reasonable agreement with the approximate 6%

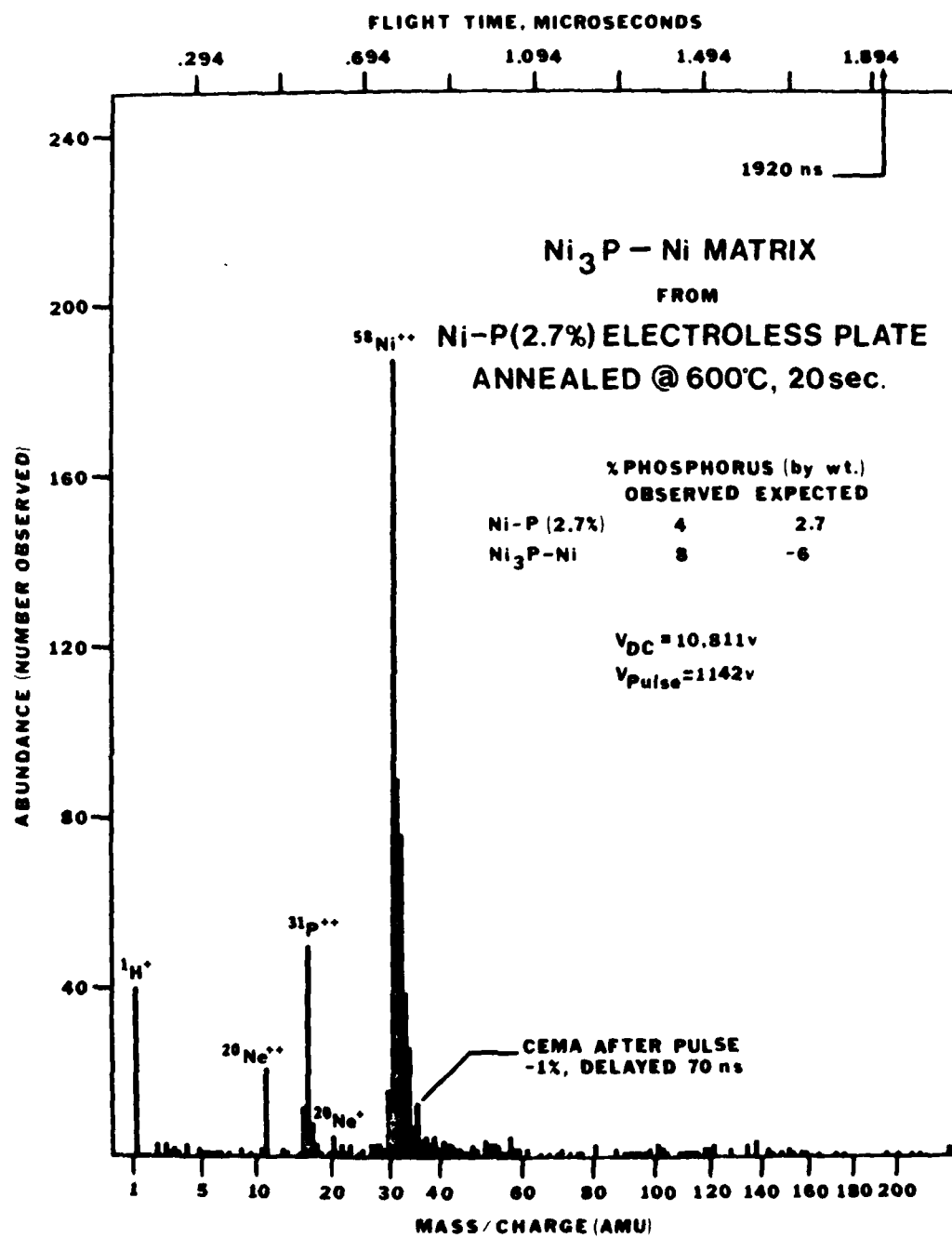


Figure 31. Relative abundance histogram of ordered Ni-Ni<sub>3</sub>P showing the increase in phosphorus expected from the area occupied by Ni<sub>3</sub>P in Figure 30(d).

abundance expected from occupation by  $\text{Ni}_3\text{P}$  of about one-half the image area sampled, Figure 30(d).

## V. SUMMARY AND CONCLUSIONS

An imaging atom-probe capable of high mass resolution time-of-flight species identification ( $m/\Delta m$  of 150 at 20% above the base line) and improved time resolution single species gated imaging ( $t/\Delta t$  of 100 at 1000 ns) has been achieved by both minimizing the initial energy dispersion of evaporated ions and reducing the capacitive load of the Chevron CEMA detector. Further, the accuracy of species identification and subsequent synchronized imaging has been significantly improved by employing a digital time-delay with an absolute accuracy of  $\pm 0.5$  ns. The instrument's only significant limitation is its present lack of a hemispherically curved Chevron detector.

This 13.5 cm instrument has demonstrated an apertured atom-probe performance fully that attributed to any one- to two-meter long, straight atom-probe, and this performance, sufficient to discriminate one out of 200 amu, is adequate for most metallurgy and surface physics applications. As such, it demonstrates a partial combination of the attributes of both the imaging and the long, straight atom-probes. Further, it is evident that these two varieties of atom-probes could be fully integrated into one general purpose instrument. The proposed instrument would consist of an externally gimbaled tip manipulator with axes crossed at the tip apex. The tip apex should simultaneously be located at the 15 cm radius of a 5-inch diameter hemispherically curved Chevron detector with an effectively apertured conductive collector-phosphor screen. Such a collector would be comprised of a small

central disc-shaped conductive area electrically insulated from the larger annular collector. Alternatively, an undivided collector screen may be used with a variable, physical aperture. This physical aperture should be in the free-flight region near the tip, but far enough away so as not to affect the termination of the acceleration region.

The application of this imaging atom-probe to both the field-adsorption of hydrogen onto a rhodium surface and the atomic micro-analysis of nickel, nickel-phosphorus electro- and electroless plate has clearly shown the wide range of problems which may be successfully studied by this technique.

In particular, it has been shown for the first time that a light coverage of field-adsorbed hydrogen displays a detailed correlation to the atomic crystal structure of a rhodium substrate, and that the hydrogen is most probably supplied directly from the gas phase. The presented hydrogen distributions clearly support the explanation of hydrogen promoted imaging advanced by Müller. That is, a mechanism based on the adsorption of hydrogen atoms in the recessed spaces available between metal atoms on planes that are not too closely packed. Since these distributions display, in atomic detail, the variations in sticking coefficient across the surface of a substrate, it may now be possible to obtain crystallographically specific distributions of reactants and products over a catalytic surface.

In conclusion, the intended purpose of this instrument was to show that the techniques of imaging and time-of-flight atom-probe analysis

could be applied to electro- or electroless deposited metals and yield new information on their nature which could not be obtained by other means. This has been successfully accomplished by the identification of atomic width boundaries in nickel-phosphorus electroless plate which was previously believed to be totally amorphous. These boundaries coincide with those observed after an annealing transformation to a mixture of  $\text{Ni}_3\text{P}$  and Ni ordered phases. Except for the observed boundaries, no other extended order or structures were detected in the as-deposited Ni-P. However, some ordered regions of  $\sim 20$  atoms, micro-crystallites, were present in the otherwise amorphous-like Ni-P electroless plate. In addition, the equilibrium  $\text{Ni}_3\text{P}$  in Ni dispersion obtained by heating as-deposited Ni-P exhibited an ordered overlayer rich in phosphorus. Hence, the occurrence of such a supersaturated crystalline solution as a result of heat treatment (proposed by A. Goldenstein et al. and G. Gutzeit<sup>45</sup>) was established, and its presence as an overlayer indicates the possible segregation of phosphorus to the surface during heating.

Collectively, these observations show as-deposited Ni-P to be a fine-grained amorphous-like solid whose boundaries are as those designated grain and phase boundaries, and whose structure is not solely liquid-like.

This work was presented at the 26th International Field Emission Symposium in Berlin,<sup>28</sup> and an extension of this study will be pursued by this author and A. J. Melmed at the National Bureau of Standards. This proposed work will include the construction of both imaging and energy corrected atom-probes whose features will include improvements

set forth in this work, and which will be used to investigate the interdiffusion of evaporated and deposited polycrystalline films. Various metallic and metallic-semiconductor couples may be employed to study volume and grain boundary diffusion by depth profiling with single atomic layer resolution. The constituent distributions and concentration profiles which would be obtained are of interest in the electronics industry. Knowledge of metal-metal <sup>43, 89</sup> and metal-semiconductor <sup>87, 90</sup> interdiffusion characteristics has become increasingly important as the metal films in solid state electronics devices have progressively become thinner, and practical measures of time-to-fail due to interdiffusion by atomic studies are now pertinent.

## APPENDIX

Detailed Electronics

The High Resolution Imaging Atom-Probe utilizes pulsed high voltage and timing circuits which are not adequately described by general principle arguments and simplified schematic diagrams. A description of these circuits, with subnanosecond rise-times and stabilities, should include design and construction information. Presented here are the drawings and specifications for the high-speed electronics which are not commercially available or which could not be fully treated in the text. Also included are the electronics for ripple reduction (0.1 PPM), accurate potential measurements, etc., which are generally needed to obtain high mass resolution spectra from time-of-flight data.

Figure 32 is a cutaway view of the discharge line pulser which generates the high voltage, 0-3 kV, evaporation pulse. This pulser, constructed by the author, is a modified version of the Huggins Laboratory, Inc. Model 961E.<sup>53</sup> The upper enclosures, charging resistor and afterpulse suppressor, are machined from  $1 \frac{1}{4}$  - inch square aluminum bar and held together by four countersunk screws. The bottom enclosures, output pulse line and FET trigger pickoff, are machined from 1-inch square aluminum bar and held in the same manner. The central high pressure, 10 atms of hydrogen, reed switch enclosure is a brass tube which also is the core for the 200 ampere-turn input trigger coil. The unit is assembled by soldering connections A, B, and C while the upper enclosures are unfolded and the trigger circuit is removed to allow access. An electronic component list for the cable discharge pulser is given in Table 2.

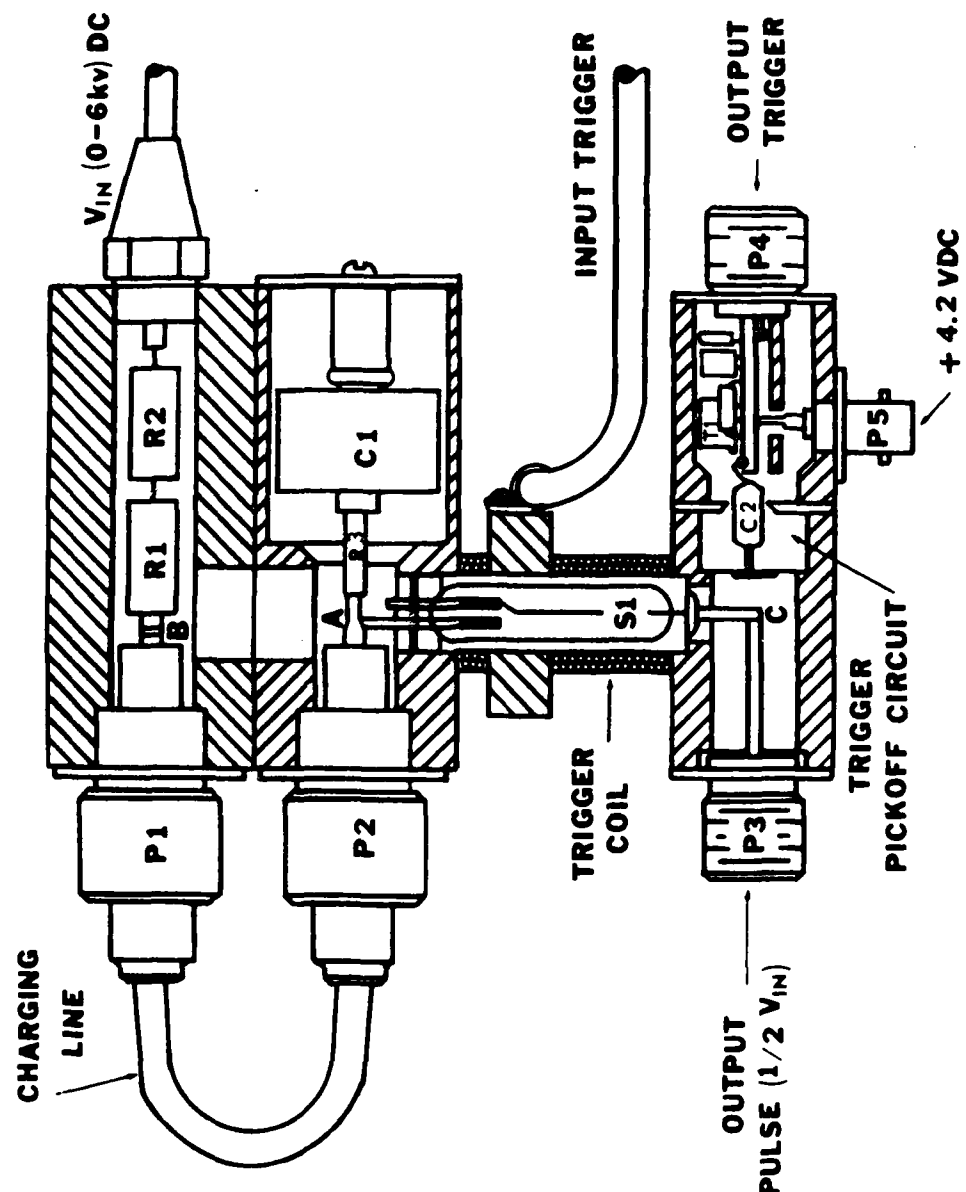


Figure 32. Cut-away view of the discharge line pulser.

Table 2. List of parts for the evaporation pulser

Circuit Reference	Description		Manufacturer	Part No.
S-1	Hg-wetted reed switch	50 ohm impedance	Clare	RP-18105
T-1	MOS-FET	DC to 500 MHz	RCA	40841
C-1	capacitor	75pf, 7.5 kV	Centralab	850S-75N
C-2		100pf, polystyrene		
C-3		50mf, flat pack		
C-4		0.05mf, disc		
R-1,2	resistor	10 megohm, 2 watt carbon composition		
R-3		1 k ohm, 1/2 watt carbon composition		
R-4		10 megohm, 1/4 watt carbon composition		
P-1,2	connector		Amphenol	UG560/u (82-8051)
P-3	connector		Amphenol	UG58A/u (82-97)
P-4	connector		Amphenol	83-798
P-5	connector, BNC		Amphenol	
	charging cable	58 ohm impedance low attenuation	Times	RG-54A
	pulse output cable	52 ohm impedance	Belden	RG-8

The first electronic concern is the DC charging voltage for the evaporation pulser. This voltage, 0 to 6 kV, is obtained from a CPS Inc. precision power supply with 0.01% ripple at 25 kHz, 0.01% per eight-hours stability, 0.001% load and line regulation, and a temperature coefficient of 25 PPM/°C. The ripple component in this potential and the other potentials which determine the ions' energy and detection must be reduced as a change of 2 volts in  $10^4$  volts will cause a variation of 0.1 ns in  $10^3$  ns in ion arrival times. In addition, a ripple voltage coupled into the oscilloscope will cause bending of the trace, vertical sensitivity is 50 mV/cm, displaying the mass signal at its time of arrival.

The ripple voltage is reduced by a low-pass filter in each voltage input to the spectrometer. The power requirements of filter components are minimal, 0.05 watts, because the instrument loads are nearly electrostatic requiring only a few microamperes of current. The low-pass filter within the pulser is composed of the 20-megohm series resistor, R-1 plus R-2, shunted to ground by R-3 plus C-1. The filtered output is available at the switch, point A in Figure 32. The remaining filters are similar in construction with a 20-megohm, 2 watt, varnished, high-voltage, Victoreen series resistor shunted by a 500 pf, high-voltage, Sprague, "door knob" capacitor. The low-pass network is an AC potential divider whose attenuation coefficient for the ripple voltage,  $r$ , is written as

$$\beta = \frac{r_{out}}{r_{in}} = \frac{x_c @ 25 \text{ kHz}}{\left[ R^2 + x_c^2 @ 25 \text{ kHz} \right]^{1/2}} , \quad (\text{A.1})$$

where  $X_C$  is the magnitude,  $1/\omega_C$ , of the capacitive reactance, where phase is not a concern. The  $\beta$  of 0.005 for the filter within the pulser reduces a charging voltage ripple of 0.6 volts @6kV to 0.3 mV @6kv, 0.5 PPM. The remaining filters with  $\beta$ 's of 0.001 yield output potentials which are ripple free to 0.1 PPM.

Secondly, the evaporation pulser must be triggered, and provide an output trigger to begin the timing sequence. The input pulse to the pulser's trigger coil is obtained from the circuit shown in Figure 33(a). This circuit is a version of a design by S. B. McLane. Certain time constants and components were changed to reduce pulse droop, 0.1 volt with the coil attached, and to insure that the mercury switch closure occurs during the coil input pulse. The coil input trigger is a 4.2-volt square wave with a duration of 6 ms. Closure of the mercury switch is in phase with the trigger and occurs 4 ms after its leading edge. Closure during the driving impulse prevents bouncing of the switch contacts and, in combination with the pulser's suppression circuit, prevents afterpulsing.

The circuit in Figure 33(a) produces a 50 Hz series of trigger pulses or a single-shot trigger pulse, and its operation is straightforward. In the 50 Hz mode, switch S-1 is closed. This activates the 555 Signetics oscillator by bringing pins 4 and 8 of the 555 high, + 5 volts, yielding a 50 Hz positive square wave at pin 3-555 and pin 9-7400N. Pin 9-7400N is one terminal of a dual input NAND gate and the other, which is held high through pin 8-555, is pin 10-7400N. This arrangement functions as an inverter and produces a series of negative pulses at the NAND gate output, pin 8-7400N, and at pin 4 of

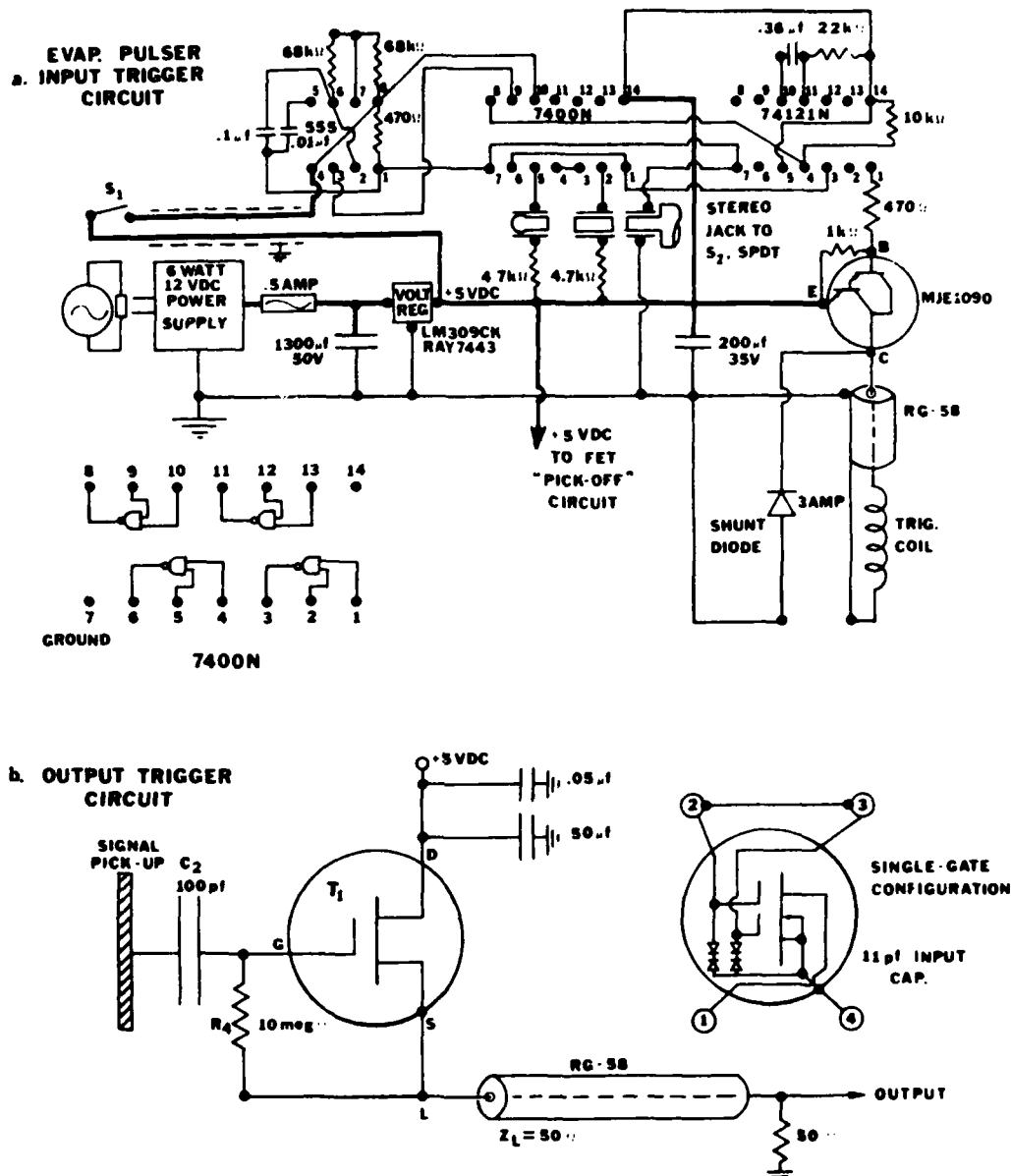


Figure 33. Input and output trigger circuits for the evaporation pulser: (a) no-bounce, input trigger circuit, (b) output trigger circuit.

the 74121N, Schmitt-trigger input monostable. Pin 4-74121N is one of the two negative transition inputs to the 74121N. If the other input, pin 3-74124N, is held high, which is the case as S-2 (not shown) is open, the monostable will yield a series of negative pulses at its output, pin 1-74121N, and at the base of the Darlington coil driving transistor. This drives the base negative, normally held high through the 1 k ohm emitter-base resistor, allowing the Darlington to conduct and energize the trigger coil. The trigger coil is 510 turns of 20-mil diameter enameled wire. When the coil's magnetic field collapses, it induces a back emf into the circuit output, which is shunted to ground through the 3-amp diode.

The single-shot mode is activated by a momentary closure of a remote microswitch, S-2, while S-1 is open. Normally, S-2 is open and the tip of the stereo jack and pin 5-7400N are low, 0 volts, while the jack's center sleeve and pin 2-7400N are high. Pins 2 and 5 of the 7400N are the inputs to a toggle or flip-flop composed of two NAND gates by connecting the output, 6-7400N, of the final gate to one input, pin 1-7400N, of the initial gate. While S-2 is open, the output, pin 6-7400N, is high; but when S-2 is closed, the input conditions are reversed, pin 5-7400N goes high and pin 2-7400N goes low, and the output of the toggle goes low. This negative transition at pin 6-7400N also appears at one of the negative transition inputs, pin 3-74121N, of the 74121N. The remainder of the sequence is the same as in the 50 Hz mode of operation. The Schmitt-trigger input monostable, 74121N, forms the operative portion of this "no-bounce" switch. Once fired, by a negative transition at either

input, pin 3 or 4, with the opposite input high, the negative output at pin 1-74121N is independent of further transitions of the inputs for a time constant which is selected by the choice of an external capacitor and resistor.

The evaporation pulser "pick-off" circuit provides a jitter-free output trigger with a rise time of less than one nanosecond and a duration equal to the evaporation pulse width, 18 ns. The trigger amplitude varies from 0.2 to 2.0 volts as the high voltage pulse changes from 150 to 2500 volts. This trigger pulse traverses an 8 ns delay line and then enters the BNC time delay through an adjustable threshold trigger input. The timing error caused by the increasing trigger amplitude is held to a fraction of a nanosecond by setting the time delay's trigger threshold to approximately 0.2 volts.

The "pick-off" circuit's location within the evaporation pulser is shown in Figure 32 and its schematic diagram is presented in Figure 33(b). The circuit's signal "pick-up" plate is within reasonable proximity to the evaporation pulse line; and, thereby, a small portion, 0.4%, of the high voltage pulse is capacitively coupled into the circuit. The circuit is a high input impedance, 10 megohm, source follower utilizing a DC to 500 megahertz field effect transistor, FET. The high input impedance insures that the circuit input will function as a simple capacitive potential divider with regard to the entering high frequency transient. The divider is composed of the 100 pf high frequency input capacitor,  $C_2$ , and the 11 pf input shunt capacitance of the FET. Therefore, 90% of the incoming signal voltage is developed between the FET gate and ground. This drives the FET into conduction and produces

the trigger signal which propagates through the transmission line and is developed across the 50-ohm internal impedance of the BNC time delay.

Certain advantages and circuit functions may not be apparent because of the circuit's simple appearance and operation. First, the position of the signal "pick-up" plate is not critical as the FET input has internal diode protection which limits transient voltage amplitudes to 10 volts. The FET, also, operates on a load line, +5 volt supply and a 50-ohm load, which limits maximum saturated output current to 40 ma despite a further increase in gate signal voltage. This prevents the output current from exceeding the 50-ma current rating of the FET. Second, the gate is not brought to ground; but, rather, it is biased at zero volts by connection to the source. This allows transmission lines and loads to be connected or disconnected, while the circuit is active without exceeding the gate to source voltage rating. Third, this source follower with a gain of 0.3 retains the low input capacitance of the FET, and, thereby, its excellent wide-band frequency response. The high frequency corner, 500 megahertz, is given by

$$f \approx \frac{1}{2\pi r_s c_s}$$

where the 142-ohm internal impedance,  $r_s$ , of the FET is approximately equal to  $1/gm$ , the reciprocal of the forward transconductance, and  $c_s$  is the small signal short circuit output capacitance. In addition, the output voltage is in phase with the input signal. Fourth, this source follower with a ground plain matches the high impedance signal source to the low impedance transmission line. The impedance match

is not perfect,  $r_s = 142$  ohms while  $Z_L = 50$  ohms, but this is not a problem provided the transmission line and output termination are matched and produce only minimal reflection. Finally, an FET with a larger  $gm$  will yield higher gain, better frequency response, and a closer impedance match to the 50-ohm transmission line. The circuit may be biased to accommodate another FET by adding a resistor between points S and L in Figure 33(b). Note, the use of a matching resistor,  $77\Omega$ , from point 2 to ground will provide an exact impedance match, but it will also reduce the circuit gain to 0.2.

The preceding discussion deals with the operational aspects of accurately initiating the evaporation event and the initial timing trigger. The first begins the ion's flight, while the second begins the timing sequence which measures the ion's flight time. Each process introduces a parameter,  $\alpha$  and  $\delta$  respectively, into the flight equation. The pulse factor,  $\alpha$ , and the instrumentation delay,  $\delta$ , must be accurately determined in order to calibrate the mass spectrometer. The accuracy of  $\alpha$  depends on a description of the evaporation pulse which is more rigorous than the treatment presented in the text, while  $\delta$  relies only on the accurate determination of the various instrument and cable delays. Therefore, the measurement of the instrumentation delay is discussed first.

The instrumentation delay is the net sum of the delays encountered by a timing trigger and its corresponding mass signal. The zero of time is the instant at which the evaporation pulse and the initial trigger

simultaneously, within 0.1 ns, leave the evaporation pulser. The sequence of delays in the trigger branch and the mass signal branch of the circuit are listed below, and may be followed by referring to the schematic diagram of the spectrometer given in Figure 1.

<u>Trigger Branch</u>	<u>Mass Signal Branch</u>
8.0 ns, cable delay - pulser to BNC time delay	2.0 ns, cable delay - pulser to tip
84.5 ns, thru-put delay - BNC time delay	1-2 ns, thru-put delay - Chevron CEMA
39.0 ns, pulse width - BNC time delay output trigger	0.5 ns, cable delay - screen to exterior of vacuum system
1.7 ns, cable delay - BNC time delay to B-sweep input of 485 oscilloscope	11.2 ns, thru-put delay - P6201 FET Probe, signal pick-up to channel two
1.7 ns, cable delay - B-sweep to channel one	
134.9 ns, total trigger branch delay	~15.2 ns(14.7 to 15.7 ns), total mass signal branch delay

The instrumentation delay is equal to the difference between the trigger branch delay and the mass signal branch delay,

$$\delta = 119.7 \pm 2 \text{ ns}, \quad (\text{A.2})$$

where the uncertainty is chiefly associated with the measured value of the BNC pulse width and the thru-put delay of the Chevron CEMA. The transit time through the Chevron CEMA is given as 2 ns by the manufacturer, Galileo Electro-Optics Corp. Certain items in the two branches require further explanation. First, the flight time, less than 0.1 ns,

of 3 kV electrons across the 1-mm gap between the Chevron and the screen is neglected in the mass signal branch. Second, the pulse width, 39 ns, of the BNC output trigger is included in the trigger branch as time is normally measured from its trailing edge. In addition, the BNC output pulse is used to trigger the oscilloscope's delayed sweep, B-sweep, prior to entering channel one. Finally, the timing trigger, fiducial mark, and the mass signal incur equal, within 0.1 ns, delays in channel one and two prior to their display on the oscilloscope screen.

The above cable and thru-put delays are measured to an accuracy of  $\pm 0.1$  ns by simultaneously displaying on the 485 Tek. scope the fiducial and delayed signals at a sweep rate of 1 ns/cm. The BNC time delay is used to extend the accurate measurement range of the oscilloscope by matching an unknown time delay to the nearest nanosecond,  $\pm 0.1$  ns, via a shift in the fiducial signal. The total unknown delay is then equal to the sum of the integer time delay setting and the remaining time interval between the fiducial and delayed signal. The remaining time interval is measured from the 1 ns/cm oscilloscope trace. This procedure as it is described in the text is also used to measure the ion's total flight time, and, as such, this flight time can be no more certain than several tenths of a nanosecond.

An accurate value of the pulse factor,  $\alpha$ , can be established by a more rigorous treatment of the cable discharge pulser. The value of 1.15 for  $\alpha$  given in the text is based on the voltage amplitude of the evaporation pulse observed on the 485 Tek. oscilloscope. This amplitude is 11% below the  $V_{\text{charging}}/2$  value predicted by the rudimentary argument

presented there. In addition, the pulse shape, Figure 6a, is not the square wave which is implied in this approach. The following analysis<sup>52</sup> correctly predicts both the observed wave shape and the reduction in pulse amplitude.

For the purpose of analysis, the cable discharge pulser can be schematically represented as shown in Figure 34(a). If the interval of actual switch closure is neglected, the circuit can be considered as having two stable states, before and after closure. During these stable states, the circuit is assumed to possess only circuit elements, transmission line and impedance, whose values are independent of time. The transmission line is treated as a distributed circuit, where L and C are its series inductance per unit length and shunt capacitance per unit length, respectively. The time delay per unit length, T, and the characteristic impedance,  $Z_0$ , of the transmission line are given by

$$T = \sqrt{LC} \quad \text{and} \quad Z_0 = \sqrt{L/C} \quad , \quad (A.3)$$

respectively. The above conditions result in a network linear differential equation with constant coefficients which can be treated by the method of Laplace transforms.<sup>52,54</sup>

Let the Laplace transform of the time-dependent potential,  $V_x(t)$  at point x on the transmission line be defined as  $L\{V_x(t)\} \equiv \bar{V}_x$ . The transform,  $\bar{V}_x$ , is the sum of the positive and negative traveling wave components,  $\overset{\rightarrow}{V}_x$  and  $\overset{\leftarrow}{V}_x$ ,

$$\bar{V}_x = \overset{\rightarrow}{V}_x + \overset{\leftarrow}{V}_x, \quad \overset{\rightarrow}{V}_x = \overset{\rightarrow}{V}_0 e^{-2pTx}, \quad \overset{\leftarrow}{V}_x = \overset{\leftarrow}{V}_0 e^{2pTx},$$

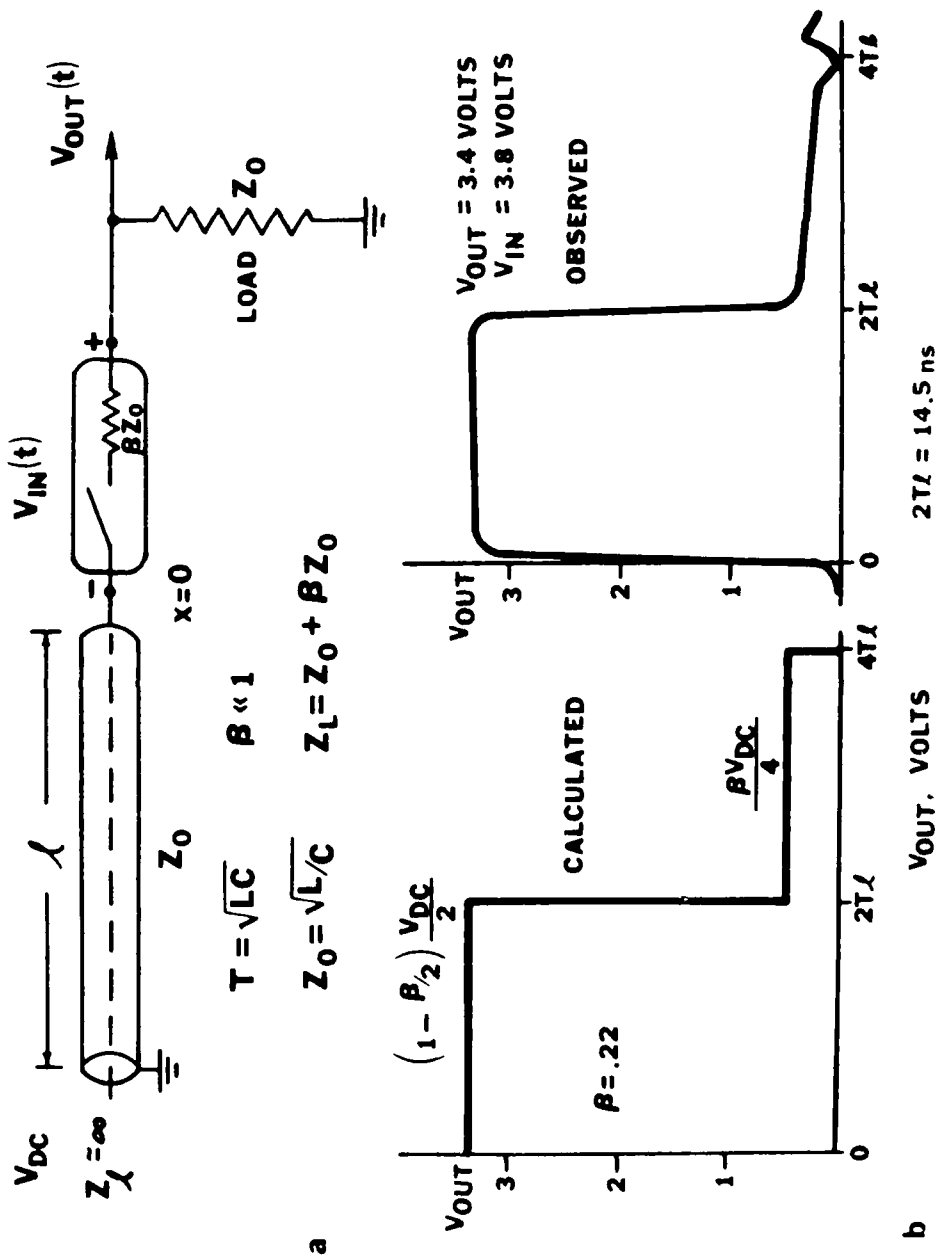


Figure 34. (a) A schematic representation of the discharge line pulser with (b) examples of its calculated and observed output pulses.

where  $p$  is the Laplace operator for  $j\omega$ . The above potential solution and corresponding current solution can be used with their respective differential equations to obtain general expressions for the reflection coefficient,  $\rho_\ell$ , and the input impedance,  $Z_{IN'}$  for a transmission line terminated at  $x = \ell$ <sup>52</sup>. The reflection coefficient is given by

$$\rho_\ell \equiv \frac{\frac{\dot{V}_\ell}{V_\ell}}{\frac{\dot{I}_\ell}{I_\ell}} = \frac{Z_\ell - Z_0}{Z_\ell + Z_0} \quad , \quad (A.4)$$

where  $Z_\ell$  is the impedance of the termination at  $x = \ell$ . The input impedance for the transmission line is given as

$$Z_{IN} = Z_0 \frac{1 + \rho_\ell e^{-2pT\ell}}{1 - \rho_\ell e^{-2pT\ell}} \quad . \quad (A.5)$$

The DC charging-leak terminal impedance,  $Z_\ell$ , at  $x = \ell$  in Figure 34(a) is nearly infinite relative to  $Z_0$ . Therefore, by equation (A.4),  $\rho_\ell = 1$ , and the input impedance from  $x = 0$  toward  $x = \ell$  is given by equation (A.5) as

$$Z_{IN} = Z_0 \frac{1 + e^{-2pT\ell}}{1 - e^{-2pT\ell}} \quad . \quad (A.6)$$

The total load impedance,  $Z_L$ , from  $x = 0$  toward the output is the sum of the load resistor,  $Z_0$ , and the internal resistance of the mercury switch,  $\beta Z_0$ . Consequently,

$$Z_L = (1 + \beta) Z_0 \quad , \quad (A.7)$$

where  $\beta \ll 1$ . If the ground loop indicated in Figure 34(a) is completed, the circuit appears as an ideal generator,  $\bar{V}_{IN}(t)$ , in series with  $Z_L$  and  $Z_{IN}$ . This is a potential divider which develops a voltage across  $Z_L$  given by

$$\bar{V}_L = \frac{Z_L}{Z_L + Z_{IN}} \bar{V}_{IN} . \quad (A.8)$$

Substituting relations (A.6) and (A.7) for  $Z_{IN}$  and  $Z_L$ , respectively, in equation (A.8) and then rearranging yields

$$\bar{V}_L = \left( \frac{1 + \beta}{2 + \beta} \right) \left( 1 - e^{-2pT\ell} \right) \left[ 1 - \left( \frac{\beta}{2 + \beta} \right) e^{-2pT\ell} \right]^{-1} \bar{V}_{IN} . \quad (A.9)$$

The term within the square brackets in equation (A.9) may be expanded as  $\beta \ll 1$  and  $pT\ell$  is positive. Retaining only first-order terms and performing the indicated multiplication yields

$$\bar{V}_L \approx \frac{(1 + \beta)}{2(1 + \beta) + \beta^2/2} \left[ \left( 1 + \beta/2 \right) - e^{-2pT\ell} - \beta/2 e^{-4pT\ell} \right] \bar{V}_{IN} .$$

The  $\beta^2$  term is neglected as  $\beta \ll 1$ , and, therefore,  $\bar{V}_L$  may be written as

$$\bar{V}_L \approx \frac{1}{2} \left[ \left( 1 + \beta/2 \right) - e^{-2pT\ell} - \beta/2 e^{-4pT\ell} \right] \bar{V}_{IN} . \quad (A.10)$$

$V_L(t)$  is obtained by completing the multiplication, and then taking the inverse Laplace transform of equation (A.10),

$$v_L(t) \approx \frac{1}{2} \left(1 + \beta/2\right) v_{IN}(t) - \frac{1}{2} v_{IN}(t-2T\ell) - \frac{\beta}{4} v_{IN}(t-4T\ell) . \quad (A.11)$$

The voltage,  $v_L(t)$ , is developed across the entire load,  $Z_0 + \beta Z_0$ . The internal switch resistance  $\beta Z_0$  and the load resistor,  $Z_0$ , form a potential divider where the output,  $\bar{v}_{OUT}$  across the load,  $Z_0$ , is given as  $[Z_0/(Z_0 + \beta Z_0)] \bar{v}_L$ . Consequently, the inverse transform,  $v_{OUT}(t)$  is given by  $[1/(1+\beta)] v_L(t)$ . Expanding the denominator,  $[1 + \beta]^{-1}$ , in the same manner as in equation (A.9) yields

$$v_{OUT}(t) \approx [1 - \beta] v_L(t) . \quad (A.12)$$

The general expression for the time dependent output voltage,  $v_{OUT}(t)$ , is obtained by substituting relation (A.11) for  $v_L(t)$  in equation (A.12), and performing the indicated multiplication:

$$v_{OUT}(t) \approx \frac{1}{2} \left(1 - \beta/2\right) v_{IN}(t) - \left(\frac{1-\beta}{2}\right) v_{IN}(t-2T\ell) - \frac{\beta}{4} v_{IN}(t-4T\ell) , \quad (A.13)$$

where terms in  $\beta^2$  have been neglected. This expression is valid for any input voltage,  $v_{IN}(t)$ , which possesses a transform provided  $v_{IN}(t) = 0$  for  $t < 0$ .

The input voltage generated by the mercury switch closure at  $t = 0$  is ideally a step function which is given as

$$v_{IN}(t) = \begin{cases} 0 & t < 0 \\ V_{DC} & t > 0 \end{cases} , v_{IN}(t-2T\ell) = \begin{cases} 0 & t < 2T \\ V_{DC} & t > 2T \end{cases} , v_{IN}(t-4T\ell) = \begin{cases} 0 & t < 4T \\ V_{DC} & t > 4T \end{cases} . \quad (A.14)$$

Substituting the step function (A.14) into equation (A.13) yields the desired expression for the evaporation pulser output voltage:

$$v_{\text{OUT}}(t) = \begin{cases} \left(1 - \beta/2\right) \frac{v_{\text{DC}}}{2} & 0 < t < 2T\ell \\ \frac{\beta v_{\text{DC}}}{4} & 2T\ell < t < 4T\ell \\ 0 & t > 4T\ell \end{cases} \quad (A.15)$$

The pulse predicted by equation (A.15) is compared in Figure 34(b) to the output pulse, Figure 6(a), observed with the 485 Tek. oscilloscope. The observed pulse amplitude from time zero to  $2T\ell$  is 11% below  $v_{\text{DC}}/2$  for an 8 to 80 volt range in  $v_{\text{DC}}$ , the charging voltage,  $v_{\text{DC}}$ , being measured to  $\pm 0.1$  volt via a digital volt meter. A predicted output based on an internal switch or arc resistance of 11 ohms,  $\beta = 0.22$ , matches the observed 11% reduction in output pulse amplitude. In addition, the calculated ratio of "shoulder" to pulse amplitude,  $v_{\text{OUT}}(2T\ell < t < 4T\ell)/v_{\text{OUT}}(0 < t < 2T\ell)$ , is 0.12 for a  $\beta$  of 0.22, while the observed value declines nearly linearly from 0.12 to 0.06. The relative ratio of the initial "shoulder" amplitude to the pulse height may be determined for a high voltage pulse whose absolute amplitude can no longer be measured with available equipment. From this ratio, a value of  $\beta$  may be obtained while operating at high voltage. Such observations indicate that the 11% reduction in the pedestal value of the pulse at low voltage also occurs at high voltage.

Refinements in the calculated output,  $v_{\text{OUT}}(t)$ , may be obtained by using a smooth switching input,  $v_{\text{IN}}(t)$ . The input function should rise

from zero, incur an inflection, and approach a limiting value of  $V_{DC}$ .

For example, the input

$$V_{IN}(t) = V_{DC} \left( 1 - e^{-t/RC} \right), \quad RC = 0.3 \text{ ns} \quad (A.16)$$

partially meets these requirements. It is also a reasonable attempt at simulating the effect of the arc build-up. The resulting output

$$V_{OUT}(t) \approx \begin{cases} \frac{1}{2}(1-\beta/2)V_{DC} \left( 1 - e^{-t/RC} \right) & 0 < t < 2T\ell \\ \frac{1}{2}V_{DC} \left[ \beta/2 + (1-\beta)e^{-(t-2T\ell)/RC} \right] & 2T\ell < t < 4T\ell \\ \frac{1}{2}V_{DC} \left[ \beta/2 e^{-(t-4T\ell)/RC} \right] & t > 4T\ell \end{cases} \quad (A.17)$$

is a closer match to the observed pulse shape.

The above analysis determines the evaporation pulse amplitude from zero to a time  $2T\ell$ . This pedestal height,  $V_{PED}$ , is given by

$$V_{PED} = (1 - \beta/2) \frac{V_{DC}}{2},$$

where  $\beta$  is 0.22, and  $V_{DC}$  is the experimental charging voltage. The field enhancement,  $f$ , and the pulse factor,  $\alpha$ , given in the text are determined with respect to this pedestal height. The field enhancement is a measure of the evaporation pulse overshoot,  $V_{OS}$ , and, as in the text,  $V_{OS}$  is equal to  $(f - 1)V_{PED}$ . During the pulse overshoot period, an ion acquires energy in excess of the electrostatic approximation,  $qV_{PED}$ . The pulse factor is a measure of this excess. The

values obtained for  $\alpha$  and  $f$  in the text are

$$f = 1.61 \pm 0.02$$

and

$$\alpha = 1.15 \pm 0.06$$

If the pedestal height is not well known,  $\alpha$  and  $f$  are relegated to parameters by which experimental results from a particular apparatus are matched to calculated values.

This section considers the measurement of the potentials that determine an ion's energy during flight. The inaccuracy and instability in the voltage measurement electronics should remain below the approximate  $\pm(0.2 - 0.4)\%$  uncertainty in the tip position. This insures that the  $\pm(0.25 - 0.5)\text{mm}$  uncertainty in the flight path will not be compounded by the uncertainty in the measurement of applied potentials. The applied potentials are measured by MOX-5RD Victoreen potential dividers in conjunction with a high input impedance,  $10^9$  ohms, 4 3/4 digit, Newport digital voltmeter. The digital voltmeter has a zero to 4-volt range with a maximum error per 8-hour period of 0.005% of reading  $\pm 0.005\%$  of full scale. The dividers are  $10^4:1$  @ 1000 megohms for  $V_a$  and  $V_{CH1}$ ,  $10^3:1$  @ 200 megohms for  $V_{TB}$ , and  $2 \times 10^3:1$  @ 400 megohms for the pulse charging voltage,  $V_{DC}$ . The dividers are 6-watt, metal oxide glaze on alumina tapped resistors approximately 5 inches in length and 1/4-inch in diameter. Their compact size permits in line use, and for pulsed electrodes they are built into coaxial housings directly at the electrodes' vacuum feed-thrus. Their ratio tolerance, 1%, and stability of 0.1% require that they be calibrated against a precision standard, CPS high voltage divider probe. The CPS probe has a ratio

accuracy of 0.01% and a temperature coefficient of 10 PPM/ $^{\circ}$ C with respect to National Bureau of Standards reference. The calibration curves for the in line dividers are shown in Figure 35. The bars indicate the  $\pm 1$  volt uncertainty of the digital voltmeter, and all data points are contained within the indicated spread. This reduces the error in potential measurement to  $\pm (0.05 - 0.1)\%$  which is approximately the error due to the uncertain last digit of the meter.

The final item is the DC "stepping" power supply shown in Figure 36. This supply was designed and constructed by John Sweeney, and it provides the stepped DC voltage to channel one of the oscilloscope.

The stepping circuit operates from regulated supply voltages of positive and negative 5 volts. It can be triggered either manually by a switch through the dual nand gate toggle or automatically by the +A gate pulse output of the oscilloscope. The circuit consists of two counters, a by 15 (7493A) and a by 10 (7490), whose outputs provide a 6-bit digital word for the MC1408 (M3408) digital-to-analog converter. An operational amplifier, MC1741C, converts the resulting stepped analog output current to a voltage output which is then applied to the Darlington driving arrangement. The incremental DC output is developed across a 50-ohm load resistor and then coupled into channel one of the oscilloscope. In add mode, the oscilloscope scales and combines this input with the mass signal present on channel two producing the small displacement between sequential mass traces in the 26 traces per frame photographic data.

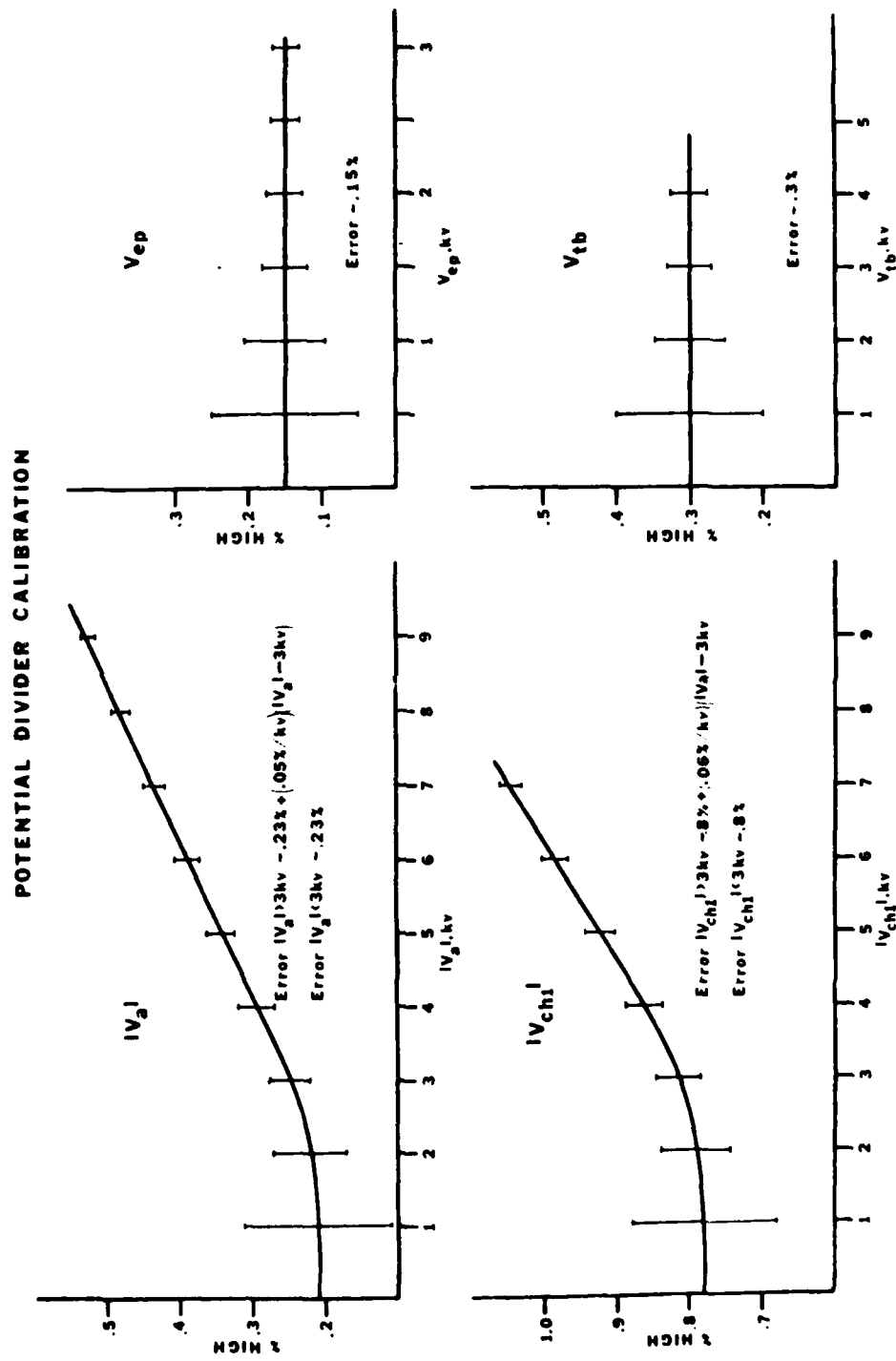


Figure 35. Calibration curves for the potential dividers.

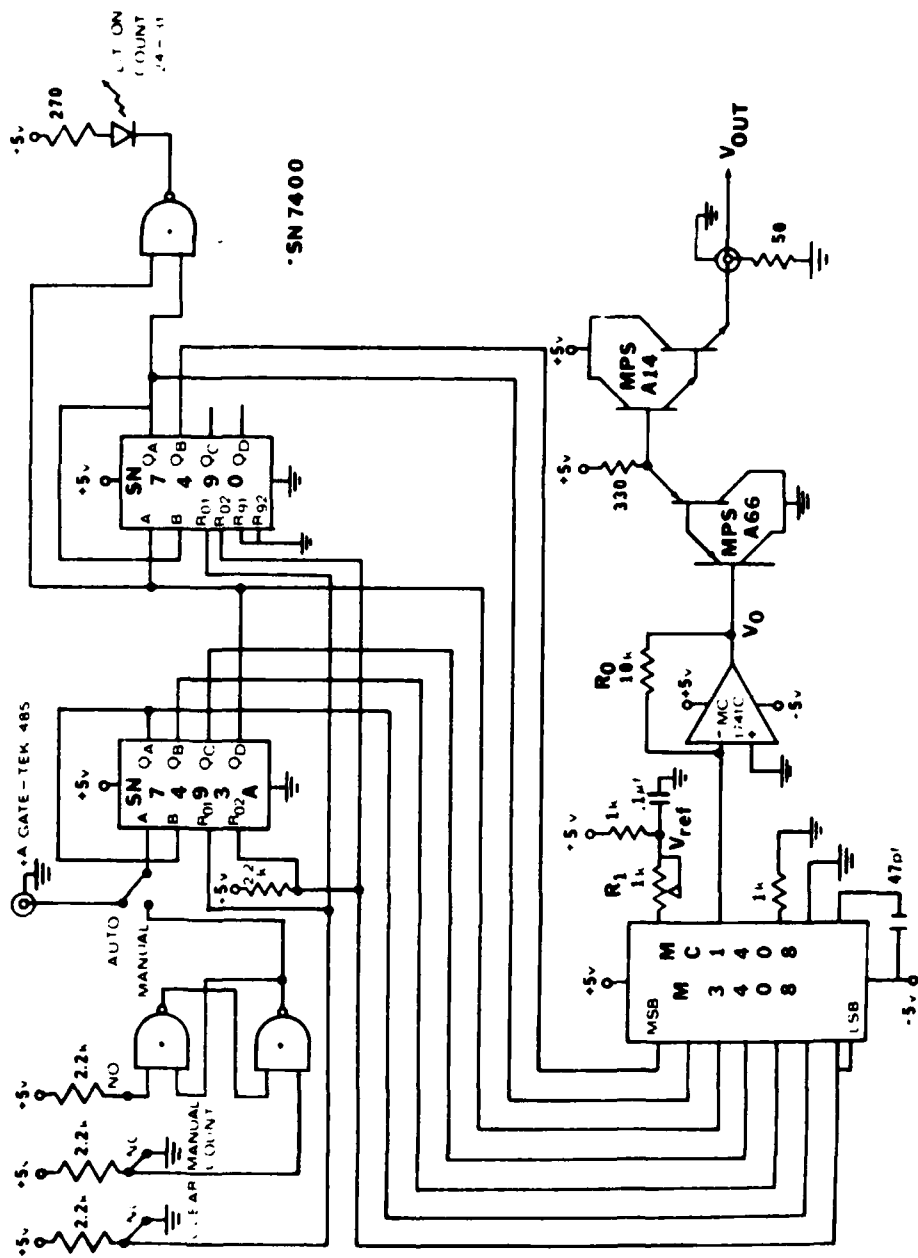


Figure 36. Schematic diagram of the stepped DC power supply.

## BIBLIOGRAPHY

1. J. A. Panitz, *Progress in Surface Science* 8, 219 (1978). The "Imaging Atom-Probe" as a descriptive instrument title was suggested by A. J. Waugh of the University of Cambridge, Cambridge, England.
2. E. W. Müller and R. J. Walko, 19th Int'l. Field Emission Symposium, Urbana, Illinois (1972).
3. E. W. Müller, S. V. Krishnaswamy, S. B. McLane, T. Sakurai, and R. J. Walko, 19th Int'l. Field Emission Symposium, Urbana, Illinois (1972).
4. E. W. Müller, *Lab. Prac.* 22, 408 (1973).
5. R. J. Walko and E. W. Müller, *Phys. Stat. Sol. (a)* 9, K9 (1972).
6. J. A. Panitz, *Rev. Sci. Instrum.* 44, 1034 (1973).
7. J. A. Panitz, *J. Vac. Sci. & Technol.* 11, 206 (1974).
8. J. A. Panitz, *J. Vac. Sci. & Technol.* 12, 210 (1975).
9. J. A. Panitz, *CRC Critical Reviews in Solid State Sciences* 5, 153 (1975).
10. E. W. Müller and S. V. Krishnaswamy, "Characterization of Metal and Polymer Surfaces, Metal Surfaces", Vol. 1, p. 27, Academic Press, New York (1977).
11. E. W. Müller, *CRC Critical Reviews in Solid State Sciences*, p. 99, (April, 1976).
12. S. Kapur and E. W. Müller, *Sur. Sci.* 62, 617 (1977).
13. S. V. Krishnaswamy, S. B. McLane, and E. W. Müller, *J. Vac. Sci. & Technol.* 13, 665 (1976).
14. A. R. Waugh, E. D. Boyes, and M. J. Southon, *Surf. Sci.* 61, 109 (1976).
15. J. A. Panitz, "Hydrogen Energy", Ed. T. N. Veziroghu, Part B, p. 1079, Plenum Publishing, New York (1975).
16. D. L. Cocke and J. A. Panitz, 26th Int'l. Field Emission Symposium, West Berlin, Germany (1979).

17. J. A. Panitz, J. Vac. Sci. & Technol. 14, 502 (1977).
18. A. R. Waugh, 24th Int'l. Field Emission Symposium, Oxford, England (1977).
19. R. Wagner, J. Pilliar, and S. S. Brenner, 24th Int'l. Field Emission Symposium, Oxford, England (1977).
20. A. R. Waugh and S. Paetke, 26th Int'l. Field Emission Symposium, West Berlin, Germany (1979).
21. J. A. Panitz and I. Giaever, 25th Int'l. Field Emission Symposium Abstracts, Ultramicroscopy, (September, 1979).
22. J. A. Panitz and I. Giaever, 26th Int'l. Field Emission Symposium, West Berlin, Germany (1979).
23. G. L. Kellogg and J. A. Panitz, 25th Int'l. Field Emission Symposium Abstracts, Ultramicroscopy, (September, 1979).
24. G. L. Kellogg and J. A. Panitz, 26th Int'l. Field Emission Symposium, West Berlin, Germany (1979).
25. G. L. Kellogg and T. T. Tsong, 26th Int'l. Field Emission Symposium, West Berlin, Germany (1979). G. L. Kellogg has assured this author that references alluding to high mass resolution, e.g., "separation of W isotopes", etc., would be removed from this abstract prior to its publication in Ultramicroscopy.
26. W. Drachsel, S. Nishigaki, and J. H. Block, 26th Int'l. Field Emission Symposium, West Berlin, Germany (1979).
27. S. V. Krishnaswamy, Ph.D. Dissertation, pp. 89-97, The Pennsylvania State University, University Park, Pa. (1974).
28. M. Martinka, 26th Int'l. Field Emission Symposium, West Berlin, Germany (1979).
29. E. W. Müller and T. T. Tsong, Progress in Surface Science 4, 1 (1974).
30. E. W. Müller, CRC Critical Reviews in Solid State Sciences, p. 85 (April, 1976).
31. S. V. Krishnaswamy, M. Martinka, and E. W. Müller, Surf. Sci. 64, 23 (1977).  
Also reference 29.

32. A. J. Moore and J. A. Spink, 21st Int'l. Field Emission Symposium, Marseille, France (1974).
33. A. R. Waugh, E. D. Boyes, D. A. Coppell, A. J. Watts, and M. J. Southon, 21st Int'l. Field Emission Symposium, Marseille, France (1974).  
A. R. Waugh, E. D. Boyes, and M. J. Southon, *Nature* 253, 342 (1975).  
Also reference 14.
34. S. V. Krishnaswamy, S. B. McLane, and E. W. Müller, *Rev. Sci. Instrum.* 46, 1237 (1975).
35. E. W. Müller, *Z. Physik.* 131, 136 (1951).
36. A Chevron CEMA is Galileo Electro-Optics Corp. designation for two Channeltron Electron Multiplier Arrays operated in tandem. The channels of one array are biased at a small angle with respect to those in the second array in a "Chevron"-like configuration. The arrangement permits signal pulses to be about 1000 times greater than ion-generated afterpulses.
37. M. Martinka and S. B. McLane, 25th Int'l. Field Emission Symposium, Albuquerque, New Mexico (1978). Abstracts published in Ultramicroscopy (September 1979).
38. Reference 10, page 38, mass spectra of field evaporated tantalum from E. W. Müller, *Naturwiss.* 57, 222 (1970).
39. Reference 9, Figure 6, mass spectra of field evaporated molybdenum.
40. E. W. Müller and S. V. Krishnaswamy, *Rev. Sci. Instrum.* 45, 1053 (1974).  
Also reference 27.
41. J. A. Panitz, S. B. McLane, and E. W. Müller, *Rev. Sci. Instrum.* 40, 1321 (1969).  
J. A. Panitz, Ph.D. Dissertation, pp. 62-78, The Pennsylvania State University, University Park, Pennsylvania (1969).
42. S. V. Krishnaswamy and E. W. Müller, *Rev. Sci. Instrum.* 45, 1049 (1974).  
Also reference 27.

43. "Properties of Electrodeposits Their Measurement and Significance" edited by R. Sard, H. Leidheiser, and F. Ogburn, The Electrochemical Society, Inc., Princeton (1975). This is an extensive review of the techniques used to investigate the nature of electro- and electroless deposits. Applicable references and information for nickel deposits are:  
Chapter 1, R. Sard and R. Weil (structure and strain by TEM, SEM, and X-ray diffraction)  
Chapter 4, P. C. Sander, J. B. C. Wu, and R. Weil (microstrain by Pseudo-Kossel X-ray patterns)  
Chapter 15, R. S. Oswald and R. Weil (microstrain and hardness by X-ray diffraction)  
Chapter 23, L. T. Romankiv and D. A. Thompson (magnetic properties).
44. G. Gutzeit, Metal Progr. 65, (1) 113 (1954); Trans. Inst. Metal Finishing 33, 1-29 (1956); "Electroplating Engineering Handbook", Ed. A. K. Graham, Reinhold Pub. Corp., New York (1968).
45. A. W. Goldenstein, W. Rostoker, F. Schossberger, and G. Gutzeit, J. Electrochem. Soc. 104, 104 (1957).
46. H. Heinrich and T. Haag, 26th Int'l. Field Emission Symposium, West Berlin, Germany (1979).
47. O. T. Inal and L. Keller, 26th Int'l. Field Emission Symposium, West Berlin, Germany (1979).
48. J. Piller, 26th Int'l. Field Emission Symposium, West Berlin, Germany (1979).
49. E. W. Müller and T. T. Tsong, "Field Ion Microscopy: Principles and Applications", American Elsevier Publishing Company, Inc., New York (1969), pp. 44 and 181.
50. Reference 29, page 97.
51. W. R. Blood, "MECL Systems Design Handbook", Motorola Semiconductor Products, Inc. (1972), pp. 142, 118, and 154-166.
52. I.A.D. Lewis and F. H. Wells, "Millimicrosecond Pulse Techniques", Pergamon Press, New York (1959), pp. 25-26, 39, 72, and 115-123.
53. Huggins Laboratories, Inc., 999 East Argus Avenue, Sunnyvale, California. This firm is no longer in existence, and no other source could be located.
54. D. L. Waidelich, "Steady State Waves on Transmission Lines", Trans. Amer. Inst. Elect. Engrs. 1950, 69, 1521-4.
55. EG & G Electro-Optics Division, Salem, Mass.

56. P. J. Turner, P. Cartwright, M. J. Southon, A. Van Oostrom, and B. W. Manley, *J. Sci. Instr.* 2, 731 (1969).
57. R. T. Lewis and R. Gomer, *Surface Sci.* 26, 197 (1970).
58. "Applications for Microchannel Plates", Varian/LSE Div., Palo Alto, California.
59. J. A. Panitz and J. A. Foesch, *Rev. Sci. Instrum.* 47, 44 (1976).
60. E. W. Müller, S. V. Krishnaswamy, and S. B. McLane, *Rev. Sci. Instrum.* 44, 84 (1973).
61. B. Nahrath, M. Shakhatre, and G. Decker, *Rev. Sci. Instrum.* 47, 88 (1976).
62. B. Nahrath, W. E. Blanz, and G. Decker, *Rev. Sci. Instrum.* 48, 95 (1977).
63. R. R. Alfano and N. Yurlina, *Rev. Sci. Instrum.* 40, 166 (1969).
64. R. Gomer, "Field Emission and Field Ionization", Harvard University Press, Cambridge, Massachusetts (1961).
65. J. C. Maxwell, "A Treatise on Electricity and Magnetism", 3rd ed., republished by Dover Pub. Inc., New York (1954), p. 188 and pp. 240-243.
66. J. A. Pantiz, Ph.D. Dissertation, The Pennsylvania State University, University Park, Pennsylvania (1969).
67. A. C. Melissinos, "Experiments in Modern Physics", Academic Press, New York (1969), pp. 461-464.
68. J. Roboz, "Introduction to Mass Spectrometry", John Wiley and Sons, New York (1968).
69. E. W. Müller and S. V. Krishnaswamy, *Phys. Rev. Letters* 37, 1011 (1976).
70. S. V. Krishnaswamy and S. B. McLane, *Sur. Sci.* 70, 265 (1978).
71. T. Sakurai and E. W. Müller, *Sur. Sci.* 51, 38 (1975).
72. S. Kapur and E. W. Müller, *Sur. Sci.* 66, 45 (1977).
73. S. V. Krishnaswamy and E. W. Müller, *Z. physik, chem. Neve Folge*, Bd. 104, 121 (1977).
74. S. S. Brenner and J. T. McKinney, *Rev. Sci. Instrum.* 43, 1264 (1972).

75. "Rhodium", The International Nickel Company, Inc., New York (1966).
76. E. W. Müller, *Sur. Sci.* 8, 462 (1967).
77. A. J. Melmed, *Sur. Sci.* 8, 191 (1967).
78. D. R. Gabe, "Principles of Metal Surface Treatment and Protection", Pergamon Press, New York (1972).
79. W. Blum and G. B. Hogaboom, "Principles of Electroplating and Electroforming", McGraw-Hill, Inc., New York (1949).
80. K. D. Rendulic and E. W. Müller, *J. Appl. Phys.* 38, 550 (1967).
81. O. T. Inal and A. E. Torma, *Thin Solid Films* 54, 161 (1978).
82. R. T. Allsop, Thesis, Birmingham University, Birmingham, Alabama (1953).
83. J. Gündiler and L. E. Murr, *J. Vac. Sci. Technol.* 12, 762 (1975).
84. J. W. Dini, H. R. Johnson, and H. J. Saxton, *J. Vac. Sci. Technol.* 12, 766 (1975).
85. A. Brenner and G. E. Riddell, *J. Research Nat'l. Bur. Standards* 37, 1 (1946); 33, 385 (1947); *Proc. Am. Electroplaters' Soc.* 33, 16 (1946); 34 156 (1947).
86. A. Brenner and G. E. Riddell, U. S. Patents 2,532,283 and 2,532,284 (Dec. 5., 1950).
87. M. V. Sullivan and J. H. Eigler, *J. Electrochem. Soc.* 104 226 (1957).
88. H. Nowotny and E. Henglein, *Z. phys. Chem.*, B40, 281 (1938).
89. J. C. Turn and E. L. Owen, *Plating* 61, 1015 (1974).
90. P. Z. Borukhovich, A. E. Kiv, V. I. Kimarskii, A. I. Koifman, and O. R. Niyazova, *phys. stat. sol.*, (a) 25, K133 (1974).

VITA

Michael Martinka was born in Philadelphia, Pennsylvania, on September 20, 1948, and graduated from Northeast Philadelphia High School in June, 1966. He received the B.S. degree in Physics from The Pennsylvania State University in June, 1970, and began his graduate study there as a teaching assistant in the Department of Physics the following September. Since 1973, Mr. Martinka has held a Graduate Research Assistantship, supported by the Applied Research Laboratory of The Pennsylvania State University under contract with the Naval Sea Systems Command, while working toward his doctorate with Professor Erwin W. Müller until his death, and subsequently with Professor T. T. Tsong. Mr. Martinka is the author or co-author of five scientific papers and has been awarded a National Research Council Postdoctoral Research Associateship to continue and expand his thesis research at the National Bureau of Standards in Washington, D.C.

DISTRIBUTION

Commander (NSEA 0342)  
Naval Sea Systems Command  
Department of the Navy  
Washington, DC 20362

Copies 1 and 2

Commander (NSEA 9961)  
Naval Sea Systems Command  
Department of the Navy  
Washington, DC 20362

Copies 3 and 4

Defense Technical Information Center  
5010 Duke Street  
Cameron Station  
Alexandria, VA 22314

Copies 5 through 16

